

# UC Santa Barbara

## UC Santa Barbara Electronic Theses and Dissertations

**Title**

How Do Galaxies Get Their Gas?

**Permalink**

<https://escholarship.org/uc/item/79h3v0cj>

**Author**

Ho, Stephanie H.

**Publication Date**

2019

Peer reviewed|Thesis/dissertation

UNIVERSITY of CALIFORNIA  
Santa Barbara

**How Do Galaxies Get Their Gas?**

A dissertation submitted in partial satisfaction of the  
requirements for the degree

Doctor of Philosophy

in

Physics

by

Stephanie Hoi-kiu Ho

Committee in charge:

Professor Crystal L. Martin, Chair

Professor Lars Bildsten

Professor S. Peng Oh

September 2019

The dissertation of Stephanie Hoi-kiu Ho is approved.

---

Professor Lars Bildsten

---

Professor S. Peng Oh

---

Professor Crystal L. Martin, Chair

July 2019

Copyright © 2019  
by Stephanie Hoi-kiu Ho



## Acknowledgements

I owe thanks to many people who have made this dissertation work possible and enabled me to continue the journey of exploring our universe.

First of all, I owe many thanks to my advisor Crystal Martin. From introducing me to undergraduate textbook astrophysics to showing me the ropes of observing at the Keck Observatory, and more importantly, to helping me transition into a researcher, her guidance and scientific insight have not only taught me how to understand the data, but have also helped me do science and think like a scientist. Her encouragement and support have also helped me overcome the challenges in my research pathway and push past my limits. I feel extremely fortunate to work with and learn from her, and I look forward to many more collaborations in the future.

I sincerely thank my collaborators, Chris Churchill and Glenn Kacprzak, for sharing their expertise in quasar absorption-line studies and their insight into understanding of the circumgalactic gas kinematics. In addition to their continuous support, I appreciate them for providing me the additional opportunity to observe with the 3.5-m telescope at the Apache Point Observatory; the data played a crucial role in the analysis presented in this dissertation. I also thank Joop Schaye for providing me the opportunity to work with the **EAGLE** simulation suite and keeping up an interest in my observational work. Being able to work with observations and cosmological simulations simultaneously allow me to approach the same science questions from different perspectives, and I treasure this unique learning experience. I thank Monica Turner for showing me the “basics” of handling the **EAGLE** simulations and providing useful comments and suggestions regarding my analysis with **EAGLE**. I extend my thank to the **EAGLE** team at Leiden, who shares with me their knowledge on **EAGLE**. I also thank the members of my supervising committee, Lars Bildsten and Peng Oh, who have followed my research work throughout the years and provided insightful suggestions.

I would also like to extend my thank to everyone who taught me physics, and generally, science and technology, in middle school and high school. They have expanded my childhood interest from history and archaeology to mathematics, physics, and computer programming. They have sparked my interest in learning science, which have eventually led me to pursue my current pathway of becoming a scientist.

Lastly, I would like to express my enormous thank to my parents for their continuous support and understanding.

# Curriculum Vitae

Stephanie Hoi-kiu Ho

## Education

2019	Ph.D., Physics, University of California, Santa Barbara
2016	M.A., Physics, University of California, Santa Barbara
2013	B.Sc., Physics, The Chinese University of Hong Kong, Hong Kong

## Publications

Kacprzak, G. G., Martin, C. L., Bouché, N., Churchill, C. W., Cooke, J., LeReun, A., Schroetter, I., **Ho, S. H.** & Klimek, E., *New Perspective on Galaxy Outflows from the First Detection of Both Intrinsic and Traverse Metal-line Absorption*. 2014, ApJL, 792, L12

**Ho, S. H.**, Martin, C. L., Kacprzak, G. G. & Churchill, C. W., *Quasar Probing Galaxies: I. Signatures of Gas Accretion at Redshift  $z \approx 0.2$* . 2017, ApJ, 835, 267

**Ho, S. H.** & Martin, C. L., *Resolving 3D Disk Orientation using High-Resolution Images: New Constraints on Circumgalactic Gas Inflows*. 2019, ApJ, submitted, arxiv:1901.11182

Martin, C. L., **Ho, S. H.**, Kacprzak, G. G. & Churchill, C. W., *Kinematics of Circumgalactic Gas: Feeding Galaxies and Feedback*. 2019, ApJ, 878, 84

**Ho, S. H.**, Martin, C. L. & Turner, M. L., *How Gas Accretion Feeds Galactic Disks*. 2019, ApJ, 875, 54

## Honors and Awards

2019	Rodger Doxsey Travel Prize (Honorable Mention), AAS
2018 / 2019	UC LEADS Scholar Program (Mentoring), UCSB
2017 – 2018	Graduate Opportunity Fellowship, UCSB
2017 – 2018	Doctoral Student Travel Grant, UCSB
2015 – 2016	Graduate Research Mentorship Program Fellowship, UCSB
2015	Travel Award for Excellence in Graduate Research, APS
2014 / 2016	Worster Summer Research Fellowship (Mentoring), UCSB
2014 – 2015	Outstanding Teaching Assistant Award, UCSB

2013 – 2014	Yzurdiaga Graduate Fellowship, UCSB
2013 – 2014	Herbert P. Broida Fellowship, UCSB
2011	Yasumoto International Exchange Scholarship, CUHK

### **Observing Experience**

Keck Observatory, Keck I, LRIS, 5 nights

Keck Observatory, Keck II, NIRC2, 3 nights

Apache Point Observatory, 3.5m, DIS, 6 half nights

Gemini Observatory, Gemini North, GMOS-N, 7.2 hours (queue observing)

# Abstract

## How Do Galaxies Get Their Gas?

by

Stephanie Hoi-kiu Ho

The growth of galactic disks requires a continuous gas supply, but direct observations of gas accretion onto galaxies remain rare. In this dissertation, we analyze the kinematics of the low-ionization-state gas in the circumgalactic medium (CGM) and study how the gas feeds the galactic disks. We have observed quasars behind  $z \approx 0.2$ , star-forming galaxies, and the quasar sightlines intersect the CGM within 100 kpc of the foreground galaxies. We find that the Doppler shift of the circumgalactic gas absorption shares the same sign as the quasar side of the galactic disk, but the Doppler shifts are smaller than disk rotation predicts. Our results suggest that the low-ionization-state gas in the inner CGM corotates with the galactic disks, and centrifugal forces partially support the low-ionization-state gas. However, the circumgalactic absorption spans a broader velocity range than a thin rotating disk can explain, and we model the velocity range using a simple inflow model with gas spiraling inwards near the disk plane. We also use new, high-resolution imaging to reveal the wrapping direction of galaxy spiral arms, and we combine it with the galaxy rotation curve to deduce the orientation of the galactic disk in 3D-space. Using the 3D disk orientation as an additional parameter for the inflow

model, we constrain the radial inflow speed or rule out a velocity component from radial inflow in the quasar sightline. We find inflow speeds comparable to that of the cold inflowing gas we have identified around galaxies in the **EAGLE** cosmological simulations, where most of the **EAGLE** galaxies have mass inflow rates high enough to sustain the star-forming activities of the galaxies. We also find cold rotating disks with inflowing gas in **EAGLE**, and these disks extend to radii comparable to the impact parameters of our quasar sightlines around galaxies. Hence, using both observations and simulations, we conclude that the inner CGM has significant angular momentum, and our analysis with **EAGLE** further supports our inflow interpretation for the circumgalactic kinematic observations.

# Contents

<b>1</b>	<b>Introduction</b>	<b>1</b>
<b>2</b>	<b>Quasars Probing Galaxies: Signatures of Gas Accretion at Redshift <math>z \approx 0.2</math></b>	<b>7</b>
2.1	Introduction . . . . .	8
2.2	Observations and Data Reduction . . . . .	12
2.2.1	Sample . . . . .	13
2.2.2	Keck LRIS Observations . . . . .	20
2.2.3	APO DIS Observations . . . . .	27
2.2.4	NIRC2 and GMOS Imaging Observations . . . . .	29
2.3	General Kinematic Properties of the CGM . . . . .	39
2.3.1	Evidence for Rotation . . . . .	41
2.3.2	Comparison to Galaxy Masses . . . . .	42
2.3.3	The Covering Fraction of Low-ionization-state Gas . . . . .	47
2.4	Discussion: Circumgalactic Gas Dynamics . . . . .	48
2.4.1	Angular Momentum of Circumgalactic Gas . . . . .	50
2.4.2	The Tension between the Velocity Widths of Mg II Absorbers and Rotating Disks . . . . .	54
2.4.3	Implications for How Galactic Disks Get Their Gas . . . . .	60
2.5	Conclusion . . . . .	64
<b>3</b>	<b>Resolving 3D Disk Orientation using High-Resolution Images: New Constraints on Circumgalactic Gas Inflows</b>	<b>67</b>
3.1	Introduction . . . . .	68
3.2	Data and Observations . . . . .	76
3.2.1	HST WFC3 Observations . . . . .	78
3.2.2	Keck NIRC2 Observations . . . . .	78
3.2.3	Galaxy Environment . . . . .	79
3.3	Individual Galaxies: Disk tilt and Gas Kinematic Modeling . . . . .	80
3.3.1	Deducing the Disk Tilt From High-Resolution Images . . . . .	81
3.3.2	Brief Description of the Disk Model and Radial Inflow . . . . .	82
3.3.3	Disk Tilt of Individual Galaxies and their Gas Kinematic Modeling . . . . .	84
3.4	Discussion and Implications . . . . .	95

3.4.1	The Projection of Radial Inflow is Not Symmetric About a Disk Flip	95
3.4.2	Constraining Radial Inflow Speed or Predicting the Disk Tilt . . .	96
3.4.3	Radial Inflow Detection and Inside-out Disk Growth . . . . .	99
3.5	Conclusion . . . . .	101
<b>4</b>	<b>How Gas Accretion Feeds Galactic Disks</b>	<b>105</b>
4.1	Introduction . . . . .	106
4.2	Galaxy Selection from the EAGLE Simulation . . . . .	111
4.2.1	Simulation Overview . . . . .	111
4.2.2	Defining Cold Gas . . . . .	113
4.2.3	Galaxy Selection . . . . .	113
4.2.4	Global Gas Consumption Timescale . . . . .	115
4.3	Identification of Inflowing Cold Gas . . . . .	118
4.3.1	Ballistic Approximation . . . . .	119
4.3.2	Geometry of the Inflowing Cold Gas . . . . .	122
4.3.3	Angular Momentum of Inflowing Gas . . . . .	128
4.3.4	Average Mass Inflow Rate and SFR . . . . .	128
4.3.5	Mass-weighted Average Inflow Speed . . . . .	130
4.4	Ballistic Approximation versus Hydrodynamic Calculations . . . . .	132
4.4.1	Tracking Gas Particles to Identify Inflowing Gas . . . . .	132
4.4.2	Average Mass Inflow Rate from Particle Tracking . . . . .	135
4.4.3	Mass-weighted Average Inflow Speed from Particle Tracking . . .	137
4.4.4	Star Formation from Gas Accreted onto the Inner Galaxy . . . . .	139
4.4.5	Limitations of the Ballistic Approximation . . . . .	141
4.5	Interpreting Cold Gas Kinematics from Observations . . . . .	143
4.5.1	Creating Mock Quasar Sightlines . . . . .	147
4.5.2	CGM Corotation with Galactic Disk . . . . .	149
4.5.3	Velocity Range along the LOS . . . . .	153
4.6	Summary and Conclusions . . . . .	158
<b>5</b>	<b>Summary and Future Prospects</b>	<b>162</b>
<b>A</b>	<b>The Inflow Model</b>	<b>169</b>
A.1	Kinematic Signatures of Circular Orbits in Disks . . . . .	170
A.2	Kinematics Signatures of Radial Infall in the Disk Plane . . . . .	174
<b>B</b>	<b>Rotation Curves of Galaxies in the Quasars Probing Galaxies Program</b>	<b>177</b>
<b>C</b>	<b>Projected LOS Velocities of Cold Gas Particles in the EAGLE Simulations</b>	<b>188</b>
	<b>Bibliography</b>	<b>190</b>

# Chapter 1

## Introduction

Gas accretion onto galaxies shapes the growth of the galactic disks. Decades of observations have demonstrated that galaxies require a continuous gas supply to explain the star formation history and the stellar metallicity of the disks. Without a continuous gas supply, galaxies would exhaust their gas within a few gigayears (e.g., Bigiel et al. 2008, 2011; Leroy et al. 2008, 2013). The infalling gas thereby lengthens the gas consumption timescale and regulates the galaxy star formation (Kennicutt 1983; Bouché et al. 2010; Davé et al. 2012). Accretion of metal-poor gas accounts for the relative paucity of low metallicity stars in the disk, known as the G-dwarf problem in the solar neighborhood (van den Bergh 1962; Sommer-Larsen 1991; Woolf & West 2012) but not unique to the Milky Way (MW; Worthey et al. 1996). Gas infall also explains the colors of the galactic disks along the Hubble Sequence (Kennicutt 1998; Papovich et al. 2015) and supports the inside-out disk growth scenario observed in nearby galaxies (Gogarten et al. 2010;



Barker et al. 2011; Muñoz-Mateos et al. 2011). Hence, studying how the circumgalactic gas feeds the galactic disk holds the key of understanding the assembly and the growth of galactic disks.

While hydrodynamical simulations also show that gas accretes onto galaxies (Oppenheimer et al. 2010; Stewart et al. 2011; Danovich et al. 2015) and grows the disks inside-out (Kimm et al. 2011; Pichon et al. 2011; Lagos et al. 2017), direct observations of gas accretion onto galaxies remain sparse (Putman et al. 2012). Even for our MW, much of the inflowing gas remains undetected, because only gas with the highest velocities (i.e., high-velocity clouds) can be easily distinguished kinematically from the disk gas (Zheng et al. 2015). Beyond the local universe, the detection rate of net inflow identified from galaxy spectra stays low at a few percent (Martin et al. 2012; Rubin et al. 2012), a result consistent with cold accretion streams covering small solid angles (Faucher-Giguère & Kereš 2011; van de Voort & Schaye 2012). Nevertheless, recent progress on studying the physical conditions of the circumgalactic medium (CGM) has shed light on exploring how the circumgalactic gas grows the galactic disks.

Recent transverse absorption-line observations have identified the CGM as a gas reservoir surrounding the galaxies. Extending to the virial radii (Tumlinson et al. 2017), the CGM contains a significant amount of metals (Peeples et al. 2014) and also accounts for at least half of the missing baryons associated with galaxy halos (Werk et al. 2014; Prochaska et al. 2017; Bregman et al. 2018). The ubiquitous detection of the highly ionized  $\text{O}^{+5}$  gas around blue,  $\sim L^*$  galaxies but not red galaxies not only highlights the

complex ionization structure of the CGM (Tumlinson et al. 2011), but also potentially explains the quenching of star formation in massive halos (Schawinski et al. 2014) and the bimodal distribution of galaxy colors (Strateva et al. 2001). It remains unclear whether the transformation from a blue to a red galaxy, perhaps through AGN feedback (Nelson et al. 2018), alters the CGM properties, or whether the changes in the CGM, plausibly driven by the development of the accretion shock, quench the star formation (Oppenheimer 2018; Stern et al. 2018). In any case, the CGM interacts closely with the galaxies and plays a crucial role in the evolution of galaxies.

Probing the CGM with transverse quasar sightlines also reveals the inhomogeneous spatial distribution of low-ionization-state gas (e.g.,  $\text{Mg}^+$ ) in the CGM. At the same impact parameters, sightlines near the galaxy minor axes often detect Mg II absorption with larger rest-frame equivalent width than sightlines near the major axes (e.g., Bordoloi et al. 2011; Bouché et al. 2012; Lan et al. 2014). Absorption near the galaxy minor and major axis is often attributed to outflows and inflows (Bouché et al. 2012; Kacprzak et al. 2012; Nielsen et al. 2015); minor- and major-axis sightlines intersect winds blown out perpendicular to the disk plane and gas accreted near the galactic disk plane, respectively (Shen et al. 2012; Ford et al. 2014). Even though recent quasar absorption-line studies have provided indirect evidence of gas accretion onto galaxies, most of these studies only have a small sample size, e.g., NGC 1097, a nearby spiral galaxy, in Bowen et al. (2016) and two  $z \sim 1$  galaxies in Bouché et al. (2013, 2016). Hence, despite the recent progress on understanding the CGM through absorption-line studies, how exactly the CGM feeds

the galactic disks, what is the fate of the circumgalactic gas, or simply how the gas moves around galaxies, have not been systematically explored for a uniform sample of galaxies.

Our *Quasars Probing Galaxies* (QPG) program measures the circumgalactic gas kinematics using the intervening Mg II absorption in quasar sightlines, and we describe the gas kinematics in the reference frame of the galactic disk. We select a sample of 50  $z \approx 0.2$ , star-forming galaxies, all of which have quasar sightlines intersecting the inner CGM (within half the virial radius) of the foreground galaxies. Compared to previous work that studied the circumgalactic gas kinematics (e.g., Steidel et al. 2002; Kacprzak et al. 2010, 2011; Bouché et al. 2012), our selection has a larger sample size and consists of a more homogeneous galaxy sample. Our 50 sightlines through single galaxies allow us to “stack” the galaxies and thereby produce a multi-sightline description of the average CGM kinematics.

To date, we have four publications from the QPG program. In Kacprzak et al. (2014, ApJL, 792, L12, hereafter Paper I), we studied a galaxy with its quasar sightline lying near the galaxy minor axis. We detected Mg II absorption in both the quasar sightline and the galaxy spectrum, making this one of the first outflow detection at both large impact parameter and “down-the-barrel”. Then, we modeled the outflow properties using a biconical outflow model. Ho et al. (2017, ApJ, 835, 267, hereafter Paper II) focused on a subset of 15 galaxies, all of which have quasar sightlines within  $30^\circ$  from the galaxy major axes. The Mg II Doppler shift shares the same sign as the rotation of the galactic disk at the quasar side of the galaxy, implying the gas corotates with the disk.

At the time of publication, this was the largest major-axis sightline sample discovering the corotating circumgalactic gas. To explain the broad velocity ranges spanned by the Mg II absorption, we introduced a radial inflow model with gas spiraling inward near the disk plane. Then in Ho & Martin (2019, ApJ, submitted, hereafter Paper III), we presented new high-resolution images for a subset of the 15 galaxies in Paper II. These new images revealed the wrapping direction of the spiral arms, and together with the galaxy rotation curves, we determined the galactic disk orientation in three-dimensional space. This new geometrical information provides an extra constraint for the inflow model in Paper II. Lastly, Martin et al. (2019, ApJ, 878, 84, hereafter Paper IV) presented the full QPG sample of 50 galaxy–quasar pairs and found no counter-rotating Mg II absorbers in sightlines within  $45^\circ$  from the galaxy major axis. We explored the hypothesis that individual Mg II velocity components can be explained by either gas rotating in the disk plane or gas being blown out of a galaxy in a biconical outflow. We concluded that both winds and angular momentum should be included while modeling the circumgalactic gas flow.

Most of the work presented in this thesis belongs to the QPG program. Chapter 2 and 3 present the work in Paper II and Paper III, respectively. Both chapters focus on the low-ionization-state gas kinematics detected in major-axis sightlines and the interpretation of the corotating gas spiraling inward near the disk plane. Hence, the analysis sheds light on identifying the circumgalactic gas that feeds the galactic disk and fuels star formation. In addition to studying the circumgalactic gas kinematics through observations, Chap-

ter 4 presents an inflow analysis using the cosmological simulation suite, Evolution and Assembly of GaLaxies and their Environments (**EAGLE**) project; this work is published in Ho et al. (2019, ApJ, 875, 54, hereafter Paper V). This pilot study with **EAGLE** has focused on galaxies similar to those in the QPG program. Not only does the cold inflowing gas around **EAGLE** galaxies have similar inflow speeds as those modeled in Papers II and III, but we have also found extended rotating disks with inflows. Hence, our analysis with **EAGLE** further supports our inflow interpretation for the circumgalactic kinematic observations. Chapter 5 summarizes our results and discusses the future prospects building upon the current work. The three Appendices contain auxiliary information associated with the main chapters. Appendix A provides a detailed mathematical description of the radial inflow model used in Papers II and III; this appendix is also published in Paper II. Appendix B presents the rotation curves for individual galaxies in the QPG program. We describe how we model the rotation curve to estimate the asymptotic rotation speed; we have used the latter while analyzing the circumgalactic gas kinematics and modeling the radial inflow in Papers II, III, and IV. Appendix C presents the projection plots of cold gas particles (colored by their line-of-sight velocities) for individual **EAGLE** galaxies; the plots are published in Paper V. This figure set illustrates that rotating gas structures are not rare among **EAGLE** galaxies, even though not of them have “disky” geometries.

## Chapter 2

### Quasars Probing Galaxies:

### Signatures of Gas Accretion at

### Redshift $z \approx 0.2$

We describe the kinematics of circumgalactic gas near the galactic plane, combining new measurements of galaxy rotation curves and spectroscopy of background quasars. The sightlines pass within 19–93 kpc of the target galaxy and generally detect Mg II absorption. The Mg II Doppler shifts have the same sign as the galactic rotation, so the cold gas co-rotates with the galaxy. Because the absorption spans a broader velocity range than disk rotation can explain, we explore simple models for the circumgalactic kinematics. Gas spiraling inwards (near the disk plane) offers a successful description of the observations. An Appendix describes the addition of tangential and radial gas flows

and illustrates how the sign of the disk inclination produces testable differences in the projected line-of-sight velocity range. This inflow interpretation implies that cold flow disks remain common down to redshift  $z \approx 0.2$  and prolong star formation by supplying gas to the disk.

## 2.1 Introduction

Stars and interstellar gas account for only 30% of the baryons associated with galaxies similar in mass to the Milky Way (MW; McGaugh et al. 2010). The missing baryons almost certainly reside in galaxy halos but are challenging to detect in emission due to their low density. This region between a galaxy and the intergalactic medium is known as the circumgalactic medium (CGM; Shull 2014).

Gas accretion from the CGM plays an important role in galaxy evolution. A significant rate of infall is required to extend the gas consumption time of galactic disks and explain the colors of galactic disks along the Hubble sequence (Kennicutt 1998). Accretion of gas with lower metallicity than the disk easily explains the relative paucity of low metallicity stars in the disk (van den Bergh 1962; Sommer-Larsen 1991; Woolf & West 2012), a problem not limited to the MW galaxy (Worthey et al. 1996). Remarkably, the cosmological baryonic accretion rate appears to largely determine the mass and redshift dependence of the star formation rate from  $z \approx 2$  to the present (Bouché et al. 2010; Davé et al. 2012).

Simple models based on this equilibrium require nearly half the baryons accreted by

dark matter halos to cycle through galactic disks. The prevalence and speed of galactic outflows (Heckman et al. 2000), especially among galaxies at intermediate redshift (Weiner et al. 2009; Erb et al. 2012; Martin et al. 2012; Rubin et al. 2014), provide direct evidence for gas recycling. The measured metallicity and  $\alpha$ -element enhancement of the hot wind (relative to the interstellar medium–ISM) provides direct evidence for enrichment of outflows by core-collapse supernovae (Martin et al. 2002).

Direct observations of the inflowing gas, however, remain sparse (Putman et al. 2012). The MW is clearly accreting gas. Complex C (Wakker et al. 1999) and the Magellanic stream (Fox et al. 2014) are examples of accretion, but our location inside the Galaxy limits identification of inflow to high-velocity clouds (Zheng et al. 2015). Spectral observations identify net inflow in roughly 5% of intermediate redshift galaxies (Martin et al. 2012; Rubin et al. 2012), a result consistent with inflow covering a small solid angle. The critical limitation of these down-the-barrel observations is that, much like the MW sightlines, they too require the Doppler shift of inflowing gas to be distinguished from the velocity dispersion of the interstellar medium (ISM); hence, significant mass flux may be missed.

Observing bright quasars (or galaxies) behind foreground galaxies appears to be one way to advance our empirical understanding of gas accretion (Steidel et al. 2002; Kacprzak et al. 2010, 2011; Bouché et al. 2013, 2016; Keeney et al. 2013; Nielsen et al. 2015; Diamond-Stanic et al. 2016). The challenge here is in determining whether the intervening absorption produced by the CGM can be uniquely associated with the inflowing



portion of the flows created by gas recycling. A promising strategy for working around this ambiguity is to leverage geometrical knowledge about the orientation of a galactic disk and the quasar sightline (e.g., Gauthier & Chen 2012; Keeney et al. 2013). Support for this approach can be found in both recent observations and hydrodynamical simulations.

In hydrodynamical simulations, galactic disks grow by accreting cooling gas from the CGM (Oppenheimer et al. 2010; Brook et al. 2012; Shen et al. 2012; Ford et al. 2014; Muratov et al. 2015; Christensen et al. 2016). As cold streams fall toward a galaxy, torques generated by the disk align the infalling gas with the pre-existing disk (Danovich et al. 2012, 2015). The newly accreted gas then forms an extended cold flow disk out to large radius, which co-rotates with the galaxy (Stewart et al. 2011, 2013). This gas supply prolongs star formation in disks and fuels starbursts during galaxy interactions. Feedback from star formation in the form of supernova explosions, radiation pressure, and cosmic rays drives powerful winds. Much of this wind ejecta is later re-accreted by the disk, thereby setting up the circulation pattern (Ford et al. 2014, 2016).

In a schematic representation of this circulation, much of the gas accretion takes place near the disk plane. Galactic winds, in contrast, break out of the ISM perpendicular to the disk plane (Veilleux et al. 2005). In principle, this variation in the physical origin of the absorbing gas will produce observable signatures as a function of sightline orientation relative to the galactic disk. When a galactic disk is viewed at high inclination, minor axis sightlines will intersect extraplanar gas and be sensitive to bipolar outflows. Major axis

sightlines, in contrast, will maximize sensitivity to orbits in the disk plane and will not intersect biconical outflows. Testing this schematic picture proves difficult. The published literature includes measurements of thousands of low-ionization-state absorbers, but the orientation and kinematics of the host galaxy have not typically been measured (Prochter et al. 2006).

Observations have recently begun, however, to distinguish absorbers based on the azimuthal angle of the quasar sightline.<sup>1</sup> The results largely support the above schematic representation. First, the large equivalent widths detected along minor axis sightlines,  $\alpha = 60^\circ\text{--}90^\circ$ , require a broad range of gas velocity and are thus consistent with a galactic outflow origin (Bordoloi et al. 2011, 2014; Bouché et al. 2012; Kacprzak et al. 2012; Keeney et al. 2013; Lan et al. 2014; Nielsen et al. 2015). Second, the paucity of strong absorbers at intermediate azimuthal angles (Bouché et al. 2012; Kacprzak et al. 2012) may reflect the same bimodality measured for the metallicity distribution of the circumgalactic gas (Lehner et al. 2013; Quiret et al. 2016). In other words, outflows would create not only the strong minor axis absorption but also the most metal-enriched systems. Third, the warm gas, which appears to be unique to the halos of star-forming galaxies (Tumlinson et al. 2011) seems to be concentrated near the galactic minor axis (Kacprzak et al. 2015).

As part of a larger effort to describe the gas kinematics of the inner CGM of star-forming galaxies (Paper IV), we present new spectroscopy of both redshift  $z \approx 0.2$  galaxies and background quasars. In this paper, we discuss the 15 galaxy–quasar pairs most

---

<sup>1</sup>With the vertex fixed at the galactic nucleus, azimuthal angle,  $\alpha$ , is measured from the galaxy major axis to the quasar.

likely to probe extended gas disks. Our approach has several unique aspects. Whereas traditional studies detect an intervening absorption system and then search for the host galaxy *ex post facto*, our program probes the CGM of a well-defined galaxy population. We measure rotation curves for each individual galaxy. The spectroscopy is sensitive to ionic columns  $N(\text{Mg}^+) \approx 2 \times 10^{12} \text{ cm}^{-2}$ , corresponding to gas columns  $N(\text{H}) \gtrsim 5 \times 10^{16} (Z/Z_\odot)^{-1} \text{ cm}^{-2}$ .

We describe the sample selection, observation, data reduction, and measurements in Section 2.2. We present results for the gas kinematics in Section 2.3. We test simple models for the gas kinematics in Section 2.4 to better understand the dynamics of the halo gas. We summarize the conclusions in Section 2.5. Throughout the paper, we adopt the cosmology from Planck Collaboration et al. (2015), with  $h = 0.6774$ ,  $\Omega_m = 0.3089$ ,  $\Omega_\Lambda = 0.6911$ ,  $\Omega_b = 0.0486$ ,  $\sigma_8 = 0.8159$ , and  $n_s = 0.9667$ . We use the atomic data in Morton (2003). We quote vacuum wavelengths in the near-UV, but air wavelengths for rest-frame optical transitions.

## 2.2 Observations and Data Reduction

We present the spectroscopy of 15 galaxy–quasar pairs selected from the Sloan Digital Sky Survey (SDSS) Data Release 9 (DR9) catalog (Ahn et al. 2012), using the Low Resolution Imaging Spectrometer (LRIS; Oke et al. 1995; Rockosi et al. 2010) with the Cassegrain Atmospheric Dispersion Compensatoron (ADC; Phillips et al. 2006) on the Keck I telescope. The blue sensitivity of LRIS allows us to study the near-UV Mg II

$\lambda\lambda 2796, 2803$  absorption doublet at redshift  $z \approx 0.2$ . We acquired additional longslit spectra for a subset of galaxies using the Double Imaging Spectrograph (DIS) at the Apache Point Observatory (APO) 3.5m telescope.<sup>2</sup> We describe the sample selection criteria in Section 2.2.1, the LRIS observations in Section 2.2.2, and the DIS rotation curves in Section 2.2.3. For a subset of the sample, we supplemented the SDSS imaging with higher resolution imaging as described in Section 2.2.4.

### 2.2.1 Sample

Our study focuses on galaxies with photometric redshifts in the  $0.15 < z < 0.3$  range. This redshift selection is a compromise between sensitivity to halo gas and accurate characterization of galaxy morphology. At lower redshift, the strong, near-UV resonance lines are not accessible from the largest aperture telescopes. At higher redshift, the disk position angle and inclination fit to SDSS images (York et al. 2000; Eisenstein et al. 2011) become increasingly less accurate.

We select highly inclined star-forming galaxies from the SDSS photometry. Our color cut at  $M_u - M_r < 2.0$  selects primarily late-type galaxies. We required an axis ratio of  $b/a < 0.71$  in the  $r$  band. The resulting disk inclinations are greater than  $i > 43^\circ$ .<sup>3</sup> Hence, minor axis sightlines will intersect the disk at very large radii, thereby selecting extraplanar gas. Star-forming galaxies at these redshifts tend to be fainter than the knee

---

<sup>2</sup> Instrument specifications can be found in the manual written by Robert Lupton, which is available at [http://www.apo.nmsu.edu/35m\\_operations/35m\\_manual/Instruments/DIS/DIS\\_usage.html#Lupton\\_Manual](http://www.apo.nmsu.edu/35m_operations/35m_manual/Instruments/DIS/DIS_usage.html#Lupton_Manual)

<sup>3</sup> We have applied the Hubble formula (Hubble 1926) here with  $q_0 = 0.2$ .

in the galaxy luminosity function at  $M_r^* = -20.44 + 5 \log_{10} h = -21.29 \pm 0.01$  (Blanton et al. 2003).

We observed 15 background quasars brighter than  $u_{qso} \leq 18.5$ . All these sightlines pass within 93 kpc of a target galaxy. The smallest impact parameter is 19 kpc, and the median is 57 kpc. The quasar sightlines are near the disk plane at azimuthal angles  $\leq 30^\circ$ . This selection focuses attention on the subset of Mg II absorbers most likely associated with gas accretion onto the galactic disk. Table 2.1 identifies the galaxy–quasar pairs by their coordinates. Table 2.2 lists the new observations, which are described further below.

Table 2.1. Target information from the SDSS DR9 catalog

QSO Name (1)	QSO ID (2)	QSO RA (3)	QSO DEC (4)	Galaxy Name (5)	GAL RA (6)	GAL DEC (7)	$i$ ( $^{\circ}$ ) (8)	$\theta$ ( $''$ ) (9)	$\alpha$ ( $^{\circ}$ ) (10)
J084234+565350	1237663529724674207	08 42 35.00	+56 53 50.2	J084235+565358	08 42 35.98	+56 53 58.8	60	11.8	4
J084723+254105	1237664837539332241	08 47 23.56	+25 41 05.4	J084725+254104	08 47 25.06	+25 41 04.7	52	20.2	14
J085215+171143	1237667429553537034	08 52 15.34	+17 11 43.9	J085215+171137	08 52 15.36	+17 11 37.1	63	6.8	24
J091954+291408	1237664879949054021	09 19 54.28	+29 14 08.4	J091954+291345	09 19 54.11	+29 13 45.3	66 <sup>a</sup>	23.1	11 <sup>a</sup>
J102907+421752	1237661851997503514	10 29 07.73	+42 17 52.9	J102907+421737	10 29 07.56	+42 17 37.6	50	15.4	19
J103640+565125	1237658302741741626	10 36 40.74	+56 51 26.0	J103643+565119	10 36 43.44	+56 51 19.0	62	23.2	18
J123049+071036	1237661971186712663	12 30 49.67	+07 10 37.0	J123049+071050	12 30 49.01	+07 10 50.6	45 <sup>b</sup>	16.8	4 <sup>b</sup>
J123317+103538	1237658493356671023	12 33 17.75	+10 35 38.2	J123318+103542	12 33 18.80	+10 35 42.1	50	16.0	3
J124601+173156	1237668590262616102	12 46 01.81	+17 31 56.5	J124601+173152	12 46 01.75	+17 31 52.2	63	4.5	11
J135522+303324	1237665180055765029	13 55 22.89	+30 33 24.8	J135521+303320	13 55 21.20	+30 33 20.4	80 <sup>c</sup>	22.4	2 <sup>c</sup>
J135734+254204	1237665532246884371	13 57 34.41	+25 42 04.6	J135733+254205	13 57 33.86	+25 42 05.1	45	7.5	12

Table 2.1 (cont'd)

QSO Name	QSO ID	QSO RA	QSO DEC	Galaxy Name	GAL RA	GAL DEC	$i$	$\theta$	$\alpha$
(1)	(2)	(3)	(4)	(5)	(6)	(7)	(8)	(9)	(10)
J142501+382100	1237662195073876015	14 25 01.46	+38 21 00.5	J142459+382113	14 24 59.82	+38 21 13.4	60	23.2	15
J154741+343357	1237662337327300689	15 47 41.88	+34 33 57.3	J154741+343350	15 47 41.46	+34 33 50.9	58	8.2	2
J160907+441734	1237659326563614832	16 09 07.45	+44 17 34.4	J160906+441721	16 09 06.72	+44 17 21.5	72	15.2	13
J160951+353843	1237662500544184468	16 09 51.81	+35 38 43.8	J160951+353838	16 09 51.62	+35 38 38.6	72 <sup>d</sup>	5.7	27 <sup>d</sup>

<sup>a</sup>Inclination and azimuthal angles measured from the  $r$ -band isophotes in the SDSS image. The catalog measurements have potentially included the tidal arm structure. The original SDSS DR9 catalog gives  $i = 76^\circ$  and  $\alpha = 23^\circ$ .

<sup>b</sup>Inclination and azimuthal angles measured from the NIRC2 image. The original SDSS DR9 catalog gives  $i = 68^\circ$  and  $\alpha = 19^\circ$ .

<sup>c</sup>Inclination and azimuthal angles measured from the NIRC2 image. The original SDSS DR9 catalog gives  $i = 58^\circ$  and  $\alpha = 6^\circ$ .

<sup>d</sup>Inclination and azimuthal angles measured from the NIRC2 and GMOS images. The original SDSS DR9 catalog gives  $i = 59^\circ$  and  $\alpha = 15^\circ$ .

Note. — (1) Name of the quasar. (2) SDSS object ID of the quasar. (3) Quasar R.A. (J2000). (4) Quasar Decl. (J2000). (5) Name of the galaxy. (6) Galaxy R.A. (J2000). (7) Galaxy Decl. (J2000). (8) Inclination of the galactic disk, from SDSS DR9 PhotoObjAll unless otherwise noted. The statistical error from the  $b/a$ -ratio in SDSS PhotoObjAll catalog. The typical uncertainty is  $5^\circ$  and does not include the systematic error generated by the point spread function. (9) Angular separation between the galaxy and the quasar. Angular separation has a typical uncertainty of  $\lesssim 0''.1$ , dominated by the error in determining the center of the galaxy. (10) Azimuthal angle, the angle between the galaxy major axis and the quasar sightline. Azimuthal angle has a typical uncertainty of  $3^\circ$ , which is dominated by the error in the position angle of the major axis. The position angle has been measured in the SDSS  $r$ -band image unless otherwise noted.

Table 2.2. Observations

Instrument	Target	Exposure Time (s)	Configuration	Observing Dates (Semester/Quarter)
Keck/LRIS	J084235+565358/J084234+565350	2700/3520	B1200/R900	2015 Mar 21 (2015A)
Gemini/GMOS	J084235+565358/J084234+565350	3600	$r'$	2015 Apr 23 (2015A) <sup>a</sup>
Keck/LRIS	J084725+254104/J084723+254105	3600/3520	B1200/R900	2015 Mar 22 (2015A)
Keck/LRIS	J085215+171137/J085215+171143	2700/2640	B1200/R900	2014 May 2 (2014A) <sup>a</sup>
Gemini/GMOS	J085215+171137/J085215+171143	3600	$r'$	2015 Mar 16, 2015 Apr 20 (2015A)
Keck/LRIS	J091954+291345/J091954+291408	1800/1760	B1200/R900	2015 Mar 22 (2015A)
Keck/LRIS	J102907+421737/J102907+421752	2700/2640	B1200/R900	2015 Mar 22 (2015A)
APO/DIS	J102907+421737	7200	B1200/R1200	2016 Apr 10 (2016Q2) <sup>a</sup>
Keck/LRIS	J103643+565119/J103640+565125	1800/1760	B1200/R900	2015 Mar 22 (2015A)
Keck/LRIS	J123049+071050/J123049+071036	3600/3520	B1200/R900	2015 Mar 21 (2015A)
Keck/NIRC2	J123049+071050/J123049+071036	600	$K_s$	2015 May 6 (2015A)
Keck/LRIS	J123318+103542/J123317+103538	1800/1760	B1200/R900	2014 May 3 (2014A) <sup>a</sup>



Table 2.2 (cont'd)

Instrument	Target	Exposure Time (s)	Configuration	Observing Dates (Semester/Quarter)
Keck/NIRC2	J123318+103542/J123317+103538	600	$K_s$	2015 May 6 (2015A)
Keck/LRIS	J124601+173152/J124601+173156	2700/2640	B1200/R900	2014 May 3 (2014A) <sup>a</sup>
Keck/LRIS	J135521+303320/J135522+303324	3600/3520	B1200/R900	2014 May 3 (2014A) <sup>a</sup>
Keck/NIRC2	J135521+303320/J135522+303324	600	$K_s$	2015 May 6 (2015A)
Keck/LRIS	J135733+254205/J135734+254204	2400/2340	B1200/R900	2014 May 2 (2014A) <sup>a</sup>
APO/DIS	J135733+254205	3600	B1200/R1200	2015 Mar 25 (2015Q1) <sup>a</sup>
Gemini/GMOS	J135733+254205/J135734+254204	3600	$r'$	2015 Apr 23 (2015A) <sup>a</sup>
Keck/LRIS	J142459+382113/J142501+382100	1800/1760	B1200/R900	2014 May 2-3 (2015A) <sup>a</sup>
APO/DIS	J142459+382113	5100	B1200/R1200	2016 Apr 2 (2016Q2) <sup>a</sup>
Keck/NIRC2	J142459+382113/J142501+382100	600	$K_s$	2015 May 6 (2015A)
Keck/LRIS	J154741+343350/J154741+343357	1800/1760	B1200/R900	2014 May 3 (2014A) <sup>a</sup>
Keck/NIRC2	J154741+343350/J154741+343357	600	$K_s$	2015 May 6 (2015A)

Table 2.2 (cont'd)

Instrument	Target	Exposure Time (s)	Configuration	Observing Dates (Semester/Quarter)
Gemini/GMOS	J154741+343350/J154741+343357	3600	$r'$	2015 Mar 23 (2015A) <sup>a</sup>
Keck/LRIS	J160906+441721/J160907+441734	5400/5280	B1200/R900	2015 Mar 21–22 (2015A)
Gemini/GMOS	J160906+441721/J160907+441734	3600	$r'$	2015 Apr 25 (2015A)
Keck/LRIS	J160951+353838/J160951+353843	1800/1760	B1200/R900	2014 May 2 (2014A) <sup>a</sup>
Keck/NIRC2	J160951+353838/J160951+353843	600	$K_s$	2015 May 6 (2015A)
Gemini/GMOS	J160951+353838/J160951+353843	3600	$r'$	2015 Mar 23 (2015A) <sup>a</sup>

<sup>a</sup>Not photometric.

### 2.2.2 Keck LRIS Observations

We configured the double spectrograph using the D500 dichroic, the 1200 lines  $\text{mm}^{-1}$  grism blazed at 3400 Å, and the 900 lines  $\text{mm}^{-1}$  grating blazed at 5500 Å. We binned both detectors  $2 \times 2$  producing a spatial scale of  $0''.27 \text{ pixel}^{-1}$  for both LRISb and LRISr, a dispersion of  $0.48 \text{ Å pixel}^{-1}$  for LRISb, and a dispersion of  $1.06 \text{ Å pixel}^{-1}$  for LRISr. We cut slit masks with slitlet widths of  $1''.0$  and lengths adequate to measure the sky spectrum. We designed the masks to either include nearby galaxies or to align the slitlet position angle with the major axis of the target galaxy. If neither of these multiplexing advantages could be realized, then we observed the galaxy–quasar pair with a  $1''.0$  wide longslit.

Using IRAF<sup>4</sup>, we removed fixed pattern noise as follows. We fit the overscan region of the images and subtracted a bias zeropoint. For blue spectra, pixel-to-pixel sensitivity variations were calibrated using twilight sky and internal deuterium flatfield exposures. Exposures of an internal, halogen lamp were used to flatfield the red spectra.

Cosmic rays were easily removed from the blue frames using L.A.Cosmic (van Dokkum 2001). Because of the higher cosmic ray rate on the red detector, we limited the exposure time of individual red frames to 900 s, but the high density of sky lines in the red spectra still made cosmic ray removal challenging. We created cosmic ray masks for the 2015A red frames using L.A.Cosmic. For the 2014A red frames, we made masks by comparing

---

<sup>4</sup>IRAF, <http://iraf.noao.edu>, is distributed by the National Optical Astronomy Observatory, which is operated by the Association of Universities for Research in Astronomy (AURA) under a cooperative agreement with the National Science Foundation.

individual frames to a median frame. The frames for each object were registered and then combined using the cosmic ray masks and a sigma-clipping algorithm. A two-dimensional error frame was created using the standard deviation of the image stack at each pixel.

We fit a dispersion solution to arclamp lines taken immediately before or after the science frames. We adopted vacuum and air wavelengths, respectively, for the blue and red frames. The root-mean-square (RMS) residuals were 0.15 and 0.05 Å for LRISb and LRISr spectra, where the difference reflects the number of arc lines available. The object frames were rectified using a two-dimensional fit to the dispersion solution.

We checked our dispersion solutions for each target by comparing the wavelengths of night sky emission lines to a calibrated sky spectrum from the Ultraviolet and Visual Echelle Spectrograph (UVES; Hanuschik 2003). The largest offsets found were less than 25 km s<sup>-1</sup>, and we applied a zeropoint shift to correct for them. We attribute these shifts to difference in rotator angle between the calibration and science exposures. We then applied a heliocentric correction to the spectrum of each target to correct for the earth’s seasonal motion.

We fit the median sky level at each wavelength to the portion of the slitlet not covering the galaxy or quasar. A one-dimensional object spectrum and a variance spectrum were extracted by summing over columns. We measured the spectral resolution from arc lines. For the blue spectra, the resolution was 165 km s<sup>-1</sup> and 105 km s<sup>-1</sup>, respectively, in 2014A and 2015A. For the red spectra, the average resolution was 105 km s<sup>-1</sup> and 75 km s<sup>-1</sup> in 2014A and 2015A, respectively. Higher resolution spectra would resolve

structure in the line profiles. Several velocity components spread over a 20 to 200 km s<sup>-1</sup> wide trough are normally required to fit metal-line systems (Prochaska & Wolfe 1997; Charlton & Churchill 1998; Boksenberg & Sargent 2015). Our deconvolution is described in Section 2.4.2.

### **2.2.2.1 Red Spectra: Measuring Emission-line Redshifts**

We determined the galaxy systemic redshift using optical emission lines detected in the LRISr spectra. We measured the redshifted wavelengths of the H $\alpha$  emission line for objects observed in 2014A, together with [O I]  $\lambda$ 6300, [N II]  $\lambda$ 6548, 6583, and [S II]  $\lambda$ 6716, 6731 for objects observed in 2015A on the integrated one-dimensional galaxy spectra. For the highest redshift galaxy, J123049+071050, we measured the redshifted wavelengths of H $\beta$  and [O III]  $\lambda$ 5007 emission lines. The redshifts listed in Table 2.3 define the systemic velocities.

### **2.2.2.2 Blue Spectra: Measuring the Mg II Absorption**

To quantitatively describe the Mg II strength and kinematics without introducing a particular parametric description, we perturbed each 1D spectrum 1000 times adding a random value in the range of  $[-\sigma, +\sigma]$  at each pixel, where  $\sigma^2$  is the variance in the flux density. For each fake spectrum, we identified lines by searching for several consecutive pixels with flux density at least  $1\sigma$  below the continuum level in each pixel. This velocity range defines a bandpass for each line. Integration over these pixels determined the total equivalent width and the mean velocity, which we weighted by equivalent width. When

this criterion did not identify a line, we defined a bandpass at the systemic velocity with a width of three times a resolution element and calculated the equivalent width weighted mean velocity and an upper limit on the equivalent width. We took the median of the probability distributions for the equivalent width, equivalent width weighted mean velocity, and the total velocity range as our best estimate of each parameter. The error bars represent the 68% confidence interval.

We considered both transitions in the doublet to objectively determine whether Mg II was detected. Our doublet detections have a total equivalent width with a significance of at least  $3\sigma$ ; the wavelength separation of the two lines and their equivalent width ratio must also be consistent with the Mg II transitions. For the detected systems, Table 2.3 lists the rest-frame equivalent width  $W_r$ , mean velocity  $\langle v \rangle_W$  (weighted by equivalent width), and velocity width  $\Delta v$ .

As a point of comparison, we also fit the Mg II absorption doublet. We used the custom software described in Martin et al. (2012), which applies the Levenberg–Marquardt algorithm (Press et al. 1992) to minimize the chi-squared fit statistic. Convolution of the intrinsic line profile with a Gaussian model of the line-spread function leaves the fitted profiles nearly Gaussian in form. The errors on the fitted Doppler shift are obtained from the covariance matrix. As shown in Table 2.3, the fitted Doppler shifts and the equivalent widths of the line profiles generally agree with the direct integration method described above. We therefore conclude that the results are not sensitive to how we measured the Doppler shift.

We constrain the  $\text{Mg}^+$  column density assuming optically thin absorption, which provides a robust lower limit. Our curve-of-growth analysis provides higher column densities. We do not list these doublet-ratio results in Table 2.3 because the errors are poorly constrained. The LRIS spectral resolution does not distinguish individual absorption components. Unresolved, saturated absorption components would produce misleading results. Along some sightlines, the actual ionic column densities may be orders of magnitude higher than our lower limits.

Table 2.3. Measurements from LRIS Spectroscopy

Quasar Name (1)	$z_{gal}$ (2)	$b$ (kpc) (3)	$W_r^{2796}$ (Å) (4)	$W_r^{Mg II}$ (Å) (5)	$v_D^{Mg II}$ (km s <sup>-1</sup> ) (6)	$\langle v \rangle_W^{2796}$ (km s <sup>-1</sup> ) (7)	$\Delta v_{2796}$ (km s <sup>-1</sup> ) (8)	$\Delta v_{2796}^{intr}$ (km s <sup>-1</sup> ) (9)	$N(Mg^+)$ ( $\times 10^{12}$ cm <sup>-2</sup> ) (10)
J084234+565350	0.21824 <sup>a</sup>	43	$\leq 0.24$	$\leq 0.35$	...	...	...	...	...
J084723+254105	0.19591 <sup>a</sup>	68	$0.09^{+0.01}_{-0.01}$	$0.20^{+0.03}_{-0.02}$	$-103 \pm 1$	$-105^{+9}_{-9}$	$[-176, -44]$	$[-119, -101]$	$> 5.2$
J085215+171143	0.16921 <sup>b</sup>	20	$1.31^{+0.05}_{-0.04}$	$2.51^{+0.06}_{-0.07}$	$-39 \pm 4$	$-49^{+5}_{-5}$	$[-225, 86]$	$[-135, -5]$	$> 56$
J091954+291408 <sup>c</sup>	0.23288 <sup>a</sup>	88	$0.22^{+0.01}_{-0.01}$	$0.38^{+0.02}_{-0.03}$	$-154 \pm 9$	$-147^{+5}_{-7}$	$[-266, -8]$	$[-208, -66]$	$> 7.5$
			$0.52^{+0.02}_{-0.02}$	$0.87^{+0.03}_{-0.03}$	$137 \pm 4$	$131^{+5}_{-4}$	$[-51, 292]$	$[7, 235]$	$> 16$
J102907+421752	0.26238 <sup>a</sup>	65	$0.12^{+0.03}_{-0.03}$	$0.25^{+0.03}_{-0.03}$	$-53 \pm 15$	$-53^{+17}_{-20}$	$[-134, 34]$	$[-76, -24]$	$> 5.8$
J103640+565125	0.13629 <sup>a,d</sup>	58	$0.28^{+0.06}_{-0.08}$	$0.37^{+0.07}_{-0.10}$	$412 \pm 22$	$392^{+16}_{-22}$	$[284, 516]$	$[341, 459]$	$6.6^e$
J123049+071036	0.39946 <sup>f</sup>	93	$0.08^{+0.02}_{-0.01}$	$0.12^{+0.02}_{-0.02}$	$-91 \pm 34^g$	$-93^{+36g}_{-38}$	$[-172, -21]$	$[-115, -79]$	$> 2.2$
J123317+103538	0.21040 <sup>b</sup>	57	$0.33^{+0.06}_{-0.02}$	$0.64^{+0.06}_{-0.05}$	$22 \pm 9$	$20^{+8}_{-29}$	$[-86, 129]$	$[5, 39]$	$> 14$
J124601+173156 <sup>c</sup>	0.26897 <sup>b</sup>	19	$0.31^{+0.03}_{-0.03}$	$0.58^{+0.04}_{-0.04}$	$-299 \pm 11$	$-293^{+9}_{-8}$	$[-404, -200]$	$[-314, -290]$	$> 13$
J135522+303324	0.20690 <sup>b</sup>	78	$\leq 0.18$	$\leq 0.19$	...	...	...	...	...



Table 2.3 (cont'd)

Quasar Name (1)	$z_{gal}$ (2)	$b$ (kpc) (3)	$W_r^{2796}$ (Å) (4)	$W_r^{Mg II}$ (Å) (5)	$v_D^{Mg II}$ (km s <sup>-1</sup> ) (6)	$\langle v \rangle_W^{2796}$ (km s <sup>-1</sup> ) (7)	$\Delta v_{2796}$ (km s <sup>-1</sup> ) (8)	$\Delta v_{2796}^{intr}$ (km s <sup>-1</sup> ) (9)	$N(Mg^+)$ ( $\times 10^{12}$ cm <sup>-2</sup> ) (10)
J135734+254204	0.25995 <sup>b</sup>	31	1.49 <sup>+0.02</sup> <sub>-0.02</sub>	2.65 <sup>+0.02</sup> <sub>-0.02</sub>	-6 ± 1	-33 <sup>+3</sup> <sub>-3</sub>	[-423, 197]	[-332, 107]	> 55
J142501+382100	0.21295 <sup>b</sup>	83	0.24 <sup>+0.03</sup> <sub>-0.03</sub>	0.36 <sup>+0.03</sup> <sub>-0.03</sub>	9 ± 7	21 <sup>+12</sup> <sub>-14</sub>	[-128, 221]	[-37, 130]	5.7 <sup>e</sup>
J154741+343357	0.18392 <sup>b</sup>	26	1.01 <sup>+0.02</sup> <sub>-0.02</sub>	1.91 <sup>+0.04</sup> <sub>-0.04</sub>	-15 ± 2	-12 <sup>+3</sup> <sub>-3</sub>	[-152, 156]	[-62, 65]	> 42
J160907+441734	0.14732 <sup>a</sup>	40	0.29 <sup>+0.02</sup> <sub>-0.02</sub>	0.59 <sup>+0.04</sup> <sub>-0.04</sub>	-60 ± 4	-59 <sup>+3</sup> <sub>-3</sub>	[-151, 30]	[-94, 27]	> 14
J160951+353843	0.28940 <sup>b</sup>	26	2.17 <sup>+0.04</sup> <sub>-0.03</sub>	4.24 <sup>+0.06</sup> <sub>-0.06</sub>	6 ± 2	6 <sup>+2</sup> <sub>-3</sub>	[-213, 231]	[-122, 141]	> 97

<sup>a</sup>H $\alpha$ , [O I]  $\lambda$ 6300, [N II]  $\lambda\lambda$ 6548, 6583, and [S II]  $\lambda\lambda$ 6716, 6731 emission lines are used to determine the systemic redshift.

<sup>b</sup>Only the H $\alpha$  emission line is used to determine the systemic redshift.

<sup>c</sup>Potential misidentification of host galaxy of the Mg II absorption.

<sup>d</sup>The blue spectrum shows hints of a second, weaker component just below the detection limit.

<sup>e</sup>The doublet ratio is consistent with 2:1 within uncertainties, i.e., an optically thin absorption.  $N(Mg^+)$  is calculated from the equivalent width of Mg II  $\lambda$ 2796 (i.e.,  $W_r^{2796}$ ).

<sup>f</sup>H $\beta$  and [O III]  $\lambda$ 5007 emission lines are used to determine the systemic redshift.

<sup>g</sup>The absorption system falls in a part of the spectrum without arcclamp lines. Extrapolation of the dispersion solution adds an additional error term of 34 km s<sup>-1</sup> on top of the measurement error.

Note. — (1) Name of the quasar. (2) Galaxy systemic redshift measured from emission lines. Number of significant figures listed for galaxy systemic redshift reflects its uncertainty. (3) Sightline impact parameter. (4) Rest-frame equivalent width of Mg II  $\lambda$ 2796;  $2\sigma$  upper limit is listed for non-detections. (5) Rest-frame equivalent width of both Mg II  $\lambda\lambda$ 2796, 2803;  $2\sigma$  upper limit is listed for non-detections. (6) Mg II Doppler shift measured from line profile fitting. (7) Equivalent width weighted mean Mg II velocity shift. (8) Measured velocity range. (9) Intrinsic velocity range. (10) Column density of Mg<sup>+</sup>. Lower limit on column density  $N(Mg^+)$ , which we derive for optically thin absorption (and unity covering fraction). The doublet ratio indicates that many systems are actually optically thick, so the actual columns may be orders of magnitude larger in some cases.

### 2.2.3 APO DIS Observations

Longslit spectra were obtained using the APO/DIS in 2015 March and 2016 April for three galaxies, for which the details are listed in Table 2.2. We used the grating with 1200 lines  $\text{mm}^{-1}$  for both the blue and red channels, which are blazed at 4400 Å and 7300 Å respectively. We observed with the default 1 by 1 binning, resulting in a spatial scale of  $0''.42 \text{ pixel}^{-1}$  and  $0''.40 \text{ pixel}^{-1}$  and a wavelength dispersion of  $0.62 \text{ Å pixel}^{-1}$  and  $0.58 \text{ Å pixel}^{-1}$  for the blue and red spectra respectively. We observed each of the three galaxies with a  $1''.5$  longslit, and we aligned the slitlet with the galaxy major axis. In this paper, we describe the red spectra, which captured the  $\text{H}\alpha$  emission.

The APO data reduction followed standard steps. The red frames were corrected for the zeropoint bias level, trimmed, and flat fielded using exposures of an internal quartz lamp. Cosmic rays were removed when combining frames. We masked cosmic rays using L.A. Cosmic (van Dokkum 2001), sometimes editing the masks around strong sky lines. To clean up a few remaining cosmic rays, we applied a sigma-clipping algorithm when combining frames. A two-dimensional error frame was also created along with each combined science spectrum, which was the standard deviation of each pixel among different exposures.

We used a list of vacuum wavelengths for the arclamp calibration. The RMS error in the dispersion solutions is  $0.04 \text{ Å}$ . Comparison to a UVES sky spectrum (Hanuschik 2003), converted into vacuum wavelength using the Edlén formula (Edlén 1966) and smoothed to the DIS spectral resolution, showed shifts in the emission lines up to 0.9

Å. We applied this correction and then corrected to a heliocentric reference frame. The spectral resolution of the red spectra was determined from the arclamps' lines, and was measured to be  $50 \text{ km s}^{-1}$ .

### 2.2.3.1 Rotation Curves

To obtain the position–velocity (PV) maps, we fit a Gaussian function to the emission-line profile at different spatial positions on the two-dimensional LRISr and DIS spectra.<sup>5</sup> We did not typically obtain a DIS spectrum when the LRIS slit was within  $30^\circ$  of the major axis. We calculated the projected rotation velocity relative to the redshift derived from the integrated spectrum. We plot the PV diagram of each galaxy in the middle column in Figure 2.1.

We produce galaxy rotation curves by deprojecting the position and velocity from the direct measurements onto circular orbits in the disk plane. Let  $\rho$  be the observed projected distance along the slit with respect to the galaxy center, and  $v_{los}$  be the line-of-sight velocity detected along the slit. Following Chen et al. (2005), if the slitlet is at an angle  $\zeta$  from the galaxy major axis, we translate the projected distance  $\rho$  into galactocentric radius  $R$  by

$$R = \rho \sqrt{1 + \sin^2 \zeta \tan^2 i} \quad (2.1)$$

---

<sup>5</sup> We generally used the extended  $H\alpha$  emission line to construct the PV maps. For J123049+071050, we used  $H\beta$  since  $H\alpha$  is not covered; and since the  $H\alpha$  emission line is badly contaminated by a strong skyline in the J160951+353838 spectrum, we measured  $[\text{N II}] \lambda 6583$ .

and find the rotational velocity  $v_{rot}(R)$  along the disk by

$$v_{rot}(R) = \frac{\sqrt{1 + \sin^2 \zeta \tan^2 i}}{\sin i \cos \zeta} v_{los}(\rho), \quad (2.2)$$

where  $i$  is the galaxy inclination. To calculate the error in rotation velocity  $v_{rot}(R)$ , we first estimate the uncertainty of velocity measured along the slit. We perturb each 2D spectrum by adding a random value within  $[-\sigma, \sigma]$  at each pixel, where  $\sigma^2$  represents the variance of flux density. With 1000 fake spectra, we obtain the line centroid and its uncertainty from the median and 68% confidence interval of the probability distribution. We then combine this uncertainty with the errors in inclination angle and position angle of the galaxy major axis from Table 2.1 to obtain the errors in deprojected velocities.

## 2.2.4 NIRC2 and GMOS Imaging Observations

In this paper, we use new, higher resolution imaging to check for measurement errors in the disk position angle and inclination. Table 2.1 denotes corrections to the values tabulated in the SDSS DR9 photoObj catalog. We introduce the key properties of the imaging observations here and defer details to a future paper describing the morphological structure of these galaxies. The imaging observations are summarized in Table 2.2.

We obtained images of half the target galaxies with the NIRC2 camera on the Keck II telescope on 2015 May 6. The quasar was used as the tip-tilt reference for the Laser Guide Star Adaptive Optics (van Dam et al. 2006; Wizinowich et al. 2006) system. The  $K_s$  broadband filter with a central wavelength at  $2.146 \mu\text{m}$  and a bandpass width of  $0.311 \mu\text{m}$ . We used the wide field camera with a field of view of  $40'' \times 40''$  and a plate scale

of  $0''.04 \text{ pixel}^{-1}$ . The median width of the quasar profile was  $0''.13$  FWHM. We reduced these images using the data reduction pipeline provided by the UCLA/Galactic center group (Ghez et al. 2008).

Images of a few galaxies were obtained in queue mode with the the Gemini Multi-Object Spectrograph (GMOS, Program GN-2015A-Q-60). The GMOS science images and calibration data, including the bias and twilight flats, were retrieved from the Gemini Observatory Archive<sup>6</sup>. All data were reduced using the Gemini IRAF Package. We used the  $r'$ -band filter with an effective wavelength of  $6300 \text{ \AA}$ , and wavelength interval between  $5620$  and  $6980 \text{ \AA}$ . The pixel scale was  $0''.0728 \text{ pixel}^{-1}$ , and the spatial resolution ranged from  $0''.5$  to  $0''.8$  FWHM.

#### 2.2.4.1 Galaxy Morphology

If the morphology of the target galaxy was clearly different from that in the SDSS catalog, we fit a galaxy surface brightness profile model. We wrote custom software to fit the point-spread function (PSF) of the quasar using a Moffat profile. To create a model, we convolved an exponential surface brightness profile (SB) with this PSF. We perturbed the galaxy image by adding a random value within  $[-\sigma, \sigma]$  at each pixel, where  $\sigma^2$  is the variance in flux density. We then find the underlying galaxy profile by minimizing the  $\chi^2$  between the convolved model and the fake galaxy image. Iterating this process by 1000 times, we obtain the ‘true’ galaxy profile and the uncertainty of each parameter using the median and 68% confidence interval. The uncertainties in the fitted inclination and

---

<sup>6</sup><https://archive.gemini.edu/>

the galaxy major-axis position angle are usually within  $5^\circ$  and  $3^\circ$  respectively.

#### 2.2.4.2 Galaxy Interactions and Environment

Galaxy group environment affects properties of Mg II absorption. Around group members, Mg II absorption is detected to larger impact parameters than around isolated galaxies (Bordoloi et al. 2011). Our target galaxies are generally isolated. We searched each field for galaxies with photometric redshifts within three standard deviations of our primary target. In only four of the 15 fields do we find a galaxy as bright as the target within the virial radius. We describe these four environments here; see the images in Figure 2.1.

J084723+254105 field. The photometric redshift of the red galaxy labeled *FIL* agrees with the redshift of our primary target. The LRIS spectrum of *FIL* shows no emission lines and does not cover the best spectral region for fitting an absorption-line redshift. The only other potential group member is at twice the impact parameter of our primary pair. These three galaxies may form a group.

J091954+291408 field. The bright, red galaxy  $4''.4$  northeast of our target galaxy has a photometric redshift consistent with our target. A fainter, red galaxy is located  $8''.7$  south of our target with a similar photometric redshift. These three galaxies likely form a group.

J102907+421752 field. The galaxy labeled *FIL* has spectroscopic redshift,  $z = 0.18496$ , that precludes group membership with our target. This field includes another bright galaxy, however, which is not shown in the postage stamp because it lies three times

farther from the quasar than our target galaxy. Our target and this more distant galaxy could be members of the same group.

J124601+173156 field. Within the virial radius of our primary galaxy, we find several galaxies with photometric redshifts consistent with group memberships. Slightly further away, we identified another set of galaxies with photometric redshifts also consistent with group membership. It seems likely that our target galaxy belongs to one of these groups.

We also looked for signs of galaxy interactions. One galaxy, J160951+353838, shows a tail-like structure toward the northeast side. The irregularity of rotation curve in this region confirms the identification of a merger. The quasar sightline shows the strongest Mg II absorption in the sample, and we suggest that this is related directly to the merger. SDSS images of J124601+173152 show two surface brightness peaks, which higher resolution imaging may resolve into a merger.

#### **2.2.4.3 Stellar Mass**

The stellar mass is obtained from spectral energy distribution (SED) fitting with FAST (Kriek et al. 2009), using the stellar population synthesis model from Bruzual & Charlot (2003), Chabrier IMF (Chabrier 2003), and the Calzetti dust extinction law (Calzetti et al. 2000). SDSS *ugriz* photometry is used for every galaxy. Supplementary photometry from *Galaxy Evolution Explorer* (GALEX; Martin et al. 2005) imaging is listed in Table 2.4 when available. *GALEX* data products (Morrissey et al. 2007) are downloaded from MAST<sup>7</sup>, and the deepest available image for each field is used for flux measurement.

---

<sup>7</sup><http://archive.stsci.edu>

The same aperture is used in both near-UV and far-UV images. A  $3\sigma$  upper limit is used when there is no obvious UV emission detected from the target galaxy, or when it is badly contaminated by emission from the quasar or other nearby objects. All fluxes, i.e., both SDSS and *GALEX*, are then corrected for Galactic dust extinction before input into FAST. This is done by using the reddening law from Fitzpatrick (1999), together with the  $E(B - V)$  retrieved from the NASA/IPAC Infrared Science Archive<sup>8</sup> using the calibration from Schlafly & Finkbeiner (2011). The stellar mass estimates range from  $\log(M_*/M_\odot) = 9.4$  to 10.6 with a median of  $M_* = 6.61 \times 10^9 M_\odot$ , and Table 2.4 lists the individual values for reference.

---

<sup>8</sup><http://irsa.ipac.caltech.edu>



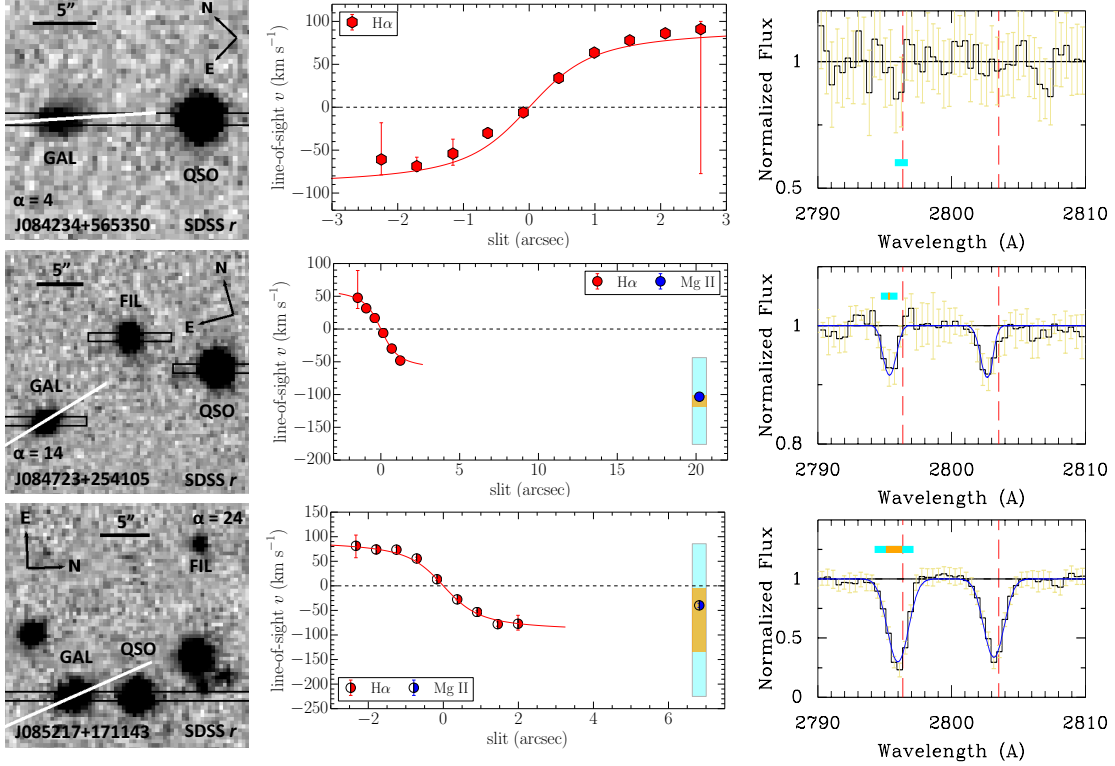


Figure 2.1: Imaging and spectroscopy of galaxy-quasar pairs. *Left Column:* SDSS  $r$ -band, GMOS  $r$ -band image, or NIRC2  $K_s$  band image. Labels indicate the quasar, target galaxy, and filler galaxies (if applicable). The black rectangle illustrates the  $1''.0$  wide LRIS slitlet, and the white line indicates the position angle of the galaxy major axis. The  $1''.5$  wide APO/DIS slitlet was aligned with the galaxy major axis. *Middle Column:* position-velocity diagram for the optical emission-line flux from LRISr and/or DIS. We show the line-of-sight velocity by direct measurements (red symbols). *Right Column:* LRISb spectrum of the Mg II system relative to the systemic velocity of the target galaxy. We superimpose the fitted line profile onto the spectrum (blue line) and show the Doppler shift of the Mg II absorption in the quasar sightline on the position-velocity diagram (blue symbol). The cyan bar shows the full line-of-sight velocity range detected while the orange bar shows the intrinsic width corrected for resolution. In cases when no Mg II absorption is detected, the cyan bar shows the FWHM of a resolution element. For the J135734+254204 sightline, we show the position-velocity map of the galaxy obtained from both the LRIS and DIS spectra. The LRIS slitlet is  $12^\circ$  from the galaxy major axis and we have no preference between the two sets of measurements.

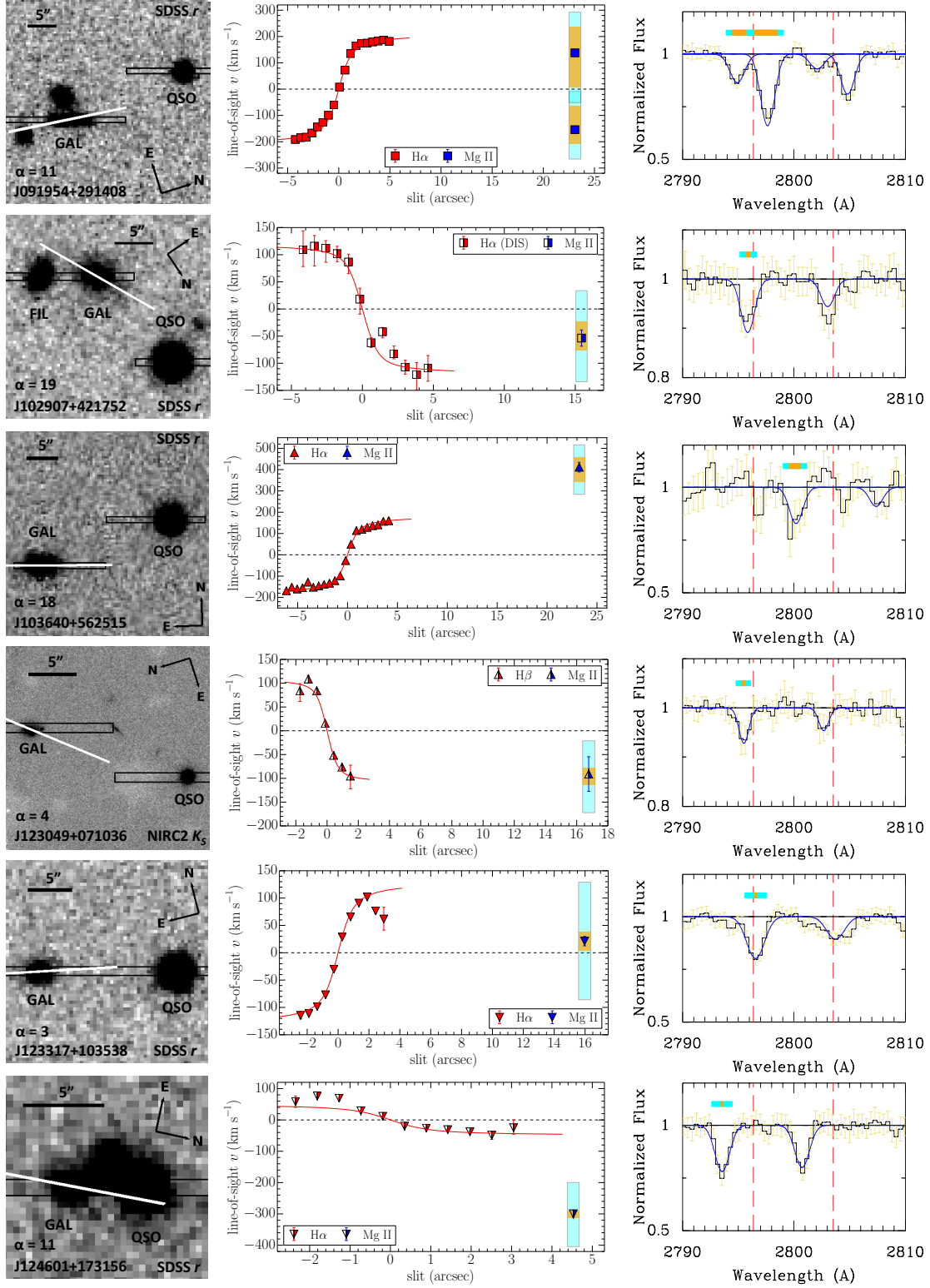


Figure 1 (*Continued*)

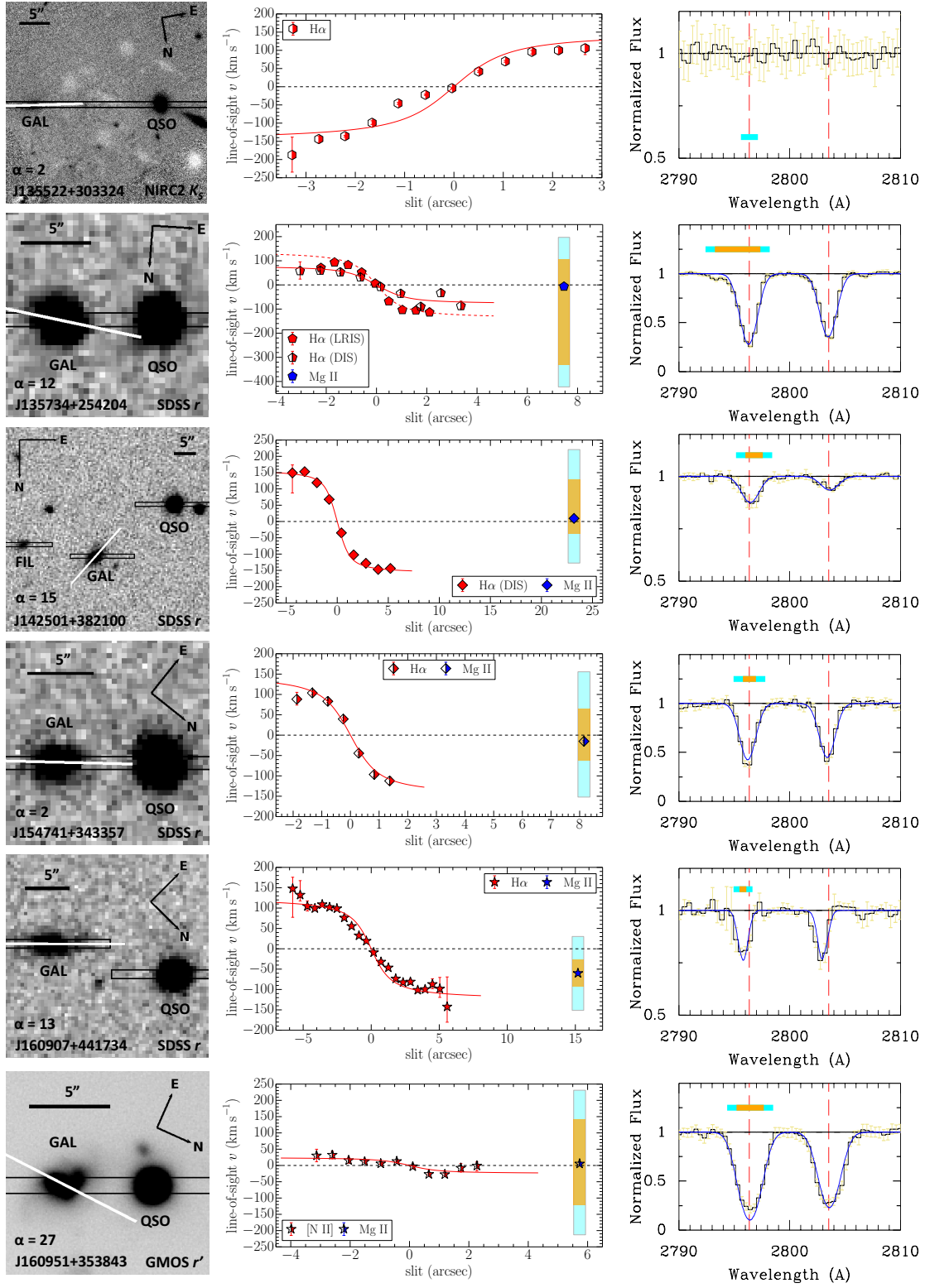


Figure 1 (*Continued*)

Table 2.4: Galaxy Properties

Galaxy Name	NUV/FUV Survey <sup>a</sup>	$m_{\text{NUV}}^a$ (AB mag)	$m_{\text{FUV}}^a$ (AB mag)	$\log(M_*/M_\odot)^b$	$\log(M_{\text{vir}}/M_\odot)^c$	$r_{\text{vir}}^d$ (kpc)	$R/r_{\text{vir}}^e$	$v_{\text{rot}}^f$ (km s <sup>-1</sup> )
J084235+565358	AIS/AIS	$\geq 22.62$	$\geq 23.30$	$9.74^{+0.21}_{-0.18}$	$11.47^{+0.12}_{-0.09}$	$155^{+15}_{-19}$	0.279	110
J084725+254104	MIS/MIS	$\geq 24.23$	$\geq 25.27$	$9.80^{+0.20}_{-0.13}$	$11.50^{+0.12}_{-0.07}$	$160^{+15}_{-8}$	0.444	115
J085215+171137	AIS/AIS	$\geq 22.11$	$\geq 23.66$	$9.71^{+0.07}_{-0.13}$	$11.45^{+0.03}_{-0.07}$	$156^{+4}_{-7}$	$0.166^g$	$150^g$
J091954+291345	DIS/AIS	$21.20 \pm 0.03$	$\geq 22.94$	$10.54^{+0.18}_{-0.17}$	$12.18^{+0.30}_{-0.22}$	$264^{+69}_{-41}$	0.366	260
J102907+421737	AIS/AIS	$\geq 22.50$	$\geq 23.15$	$10.03^{+0.11}_{-0.09}$	$11.66^{+0.08}_{-0.06}$	$174^{+12}_{-8}$	0.399	$155^h$
J103643+565119	DIS/DIS	$20.97 \pm 0.02$	$21.40 \pm 0.05$	$9.94^{+0.19}_{-0.06}$	$11.56^{+0.13}_{-0.03}$	$174^{+18}_{-5}$	0.385	205
J123049+071050	GH/GH	$22.79 \pm 0.16$	$\geq 25.01$	$10.41^{+0.03}_{-0.05}$	$12.07^{+0.03}_{-0.06}$	$220^{+6}_{-10}$	0.423	180
J123318+103542	GH/AIS	$21.96 \pm 0.11$	$\geq 22.77$	$9.62^{+0.13}_{-0.11}$	$11.41^{+0.07}_{-0.05}$	$148^{+8}_{-6}$	0.383	170
J124601+173152	GH/AIS	$\geq 23.11$	$\geq 22.60$	$9.54^{+0.02}_{-0.16}$	$11.38^{+0.01}_{-0.07}$	$140^{+1}_{-8}$	0.146	60
J135521+303320	AIS/AIS	$\geq 21.43$	$\geq 22.66$	$9.82^{+0.11}_{-0.09}$	$11.51^{+0.08}_{-0.06}$	$161^{+7}_{-10}$	0.494	155
J135733+254205	AIS/AIS	$\geq 22.15$	$\geq 23.51$	$10.24^{+0.09}_{-0.08}$	$11.83^{+0.09}_{-0.07}$	$199^{+14}_{-11}$	0.159	$160^j$
J142459+382113	MIS/AIS	$21.17 \pm 0.10$	$\geq 22.84$	$10.27^{+0.18}_{-0.14}$	$11.84^{+0.20}_{-0.12}$	$206^{+35}_{-19}$	0.441	$185^h$
J154741+343350	AIS/AIS	$\geq 22.18$	$\geq 24.38$	$9.81^{+0.17}_{-0.09}$	$11.50^{+0.10}_{-0.05}$	$161^{+6}_{-13}$	0.161	175
J160906+441721	NIL/NIL	...	...	$9.44^{+0.20}_{-0.04}$	$11.32^{+0.09}_{-0.02}$	$143^{+10}_{-2}$	0.347	130
J160951+353838	AIS/AIS	$19.34 \pm 0.08$	$20.88 \pm 0.29$	$10.02^{+0.12}_{-0.12}$	$11.66^{+0.09}_{-0.08}$	$172^{+13}_{-10}$	0.255	$50^k$

Table 2.4 (cont'd)

- 
- <sup>a</sup> AIS: All-sky Imaging Survey. MIS: Medium Imaging Survey. DIS: Deep Imaging Survey. GII: Guest Investigator Program. NIL: No available images. Fluxes are listed as measured, prior to correction for Galactic reddening. In the absence of a detection, we list the  $3\sigma$  limit.
- <sup>b</sup> Stellar mass and the 68% confidence levels are obtained from SED fitting using FAST (Kriek et al. 2009).
- <sup>c</sup> Halo mass is obtained from the stellar mass using the stellar mass-halo mass (SM-HM) relation from Behroozi et al. (2010). The confidence levels of halo mass are calculated from those of stellar mass. Uncertainties due to the scatters in SM-HM relation are not included.
- <sup>d</sup> Virial radius is calculated using Eqn. 2.3 and the redshift of each galaxy in Table 2.3, expressed in kiloparsecs. The confidence levels of virial radius are calculated from those of the halo mass.
- <sup>e</sup>  $R$  is the radial distance between the sightline and the galaxy center *on the disk plane*.
- <sup>f</sup> The asymptotic rotation speed  $v_{rot}$  has a systematic error of  $\sim 20 \text{ km s}^{-1}$  due to the uncertainty in the galaxy systemic velocity. Less extended rotation curves also impose larger uncertainties onto  $v_{rot}$ .
- <sup>g</sup> The GMOS images of the galaxy may suggest a  $5^\circ$  and sub-degree change in the inclination and major-axis position angle, respectively, from the SDSS measurements. These potential adjustments lead to extra uncertainties on  $R/r_{vir}$  and  $v_{rot}$  of no more than 15%. Furthermore, due to the scatter of individual galaxies around the mean SM-HM relation, the uncertainty in  $R/r_{vir}$  is dominated by that of  $r_{vir}$ .
- <sup>h</sup> The asymptotic rotation speed  $v_{rot}$  is derived using the rotation curve from the APO/DIS spectra. The offset of the Keck/LRIS slitlet from the galaxy major axis exceeds  $30^\circ$ .
- <sup>i</sup> The ‘galaxy’ in the SDSS is resolved into two objects. The SDSS photometry is therefore overestimated which leads to a poor SED fit using FAST. The fitted stellar mass and thereby the halo mass are subjected to systematic errors.
- <sup>j</sup> The listed  $v_{rot}$  is the average  $v_{rot}$  from the rotation curves derived from the Keck/LRIS and APO/DIS spectra. We have no preference between the two rotation curves since the Keck/LRIS slitlet is only  $12^\circ$  from the galaxy major axis.
- <sup>k</sup> The rotation curve deviates from disk-like rotation, which leads to a large uncertainty in the asymptotic rotation speed  $v_{rot}$ . The tail-like structure toward the northeast side of the galaxy suggests the possibility of galaxy interaction.

## 2.3 General Kinematic Properties of the CGM

Figure 2.1 shows the fields of the target galaxies, the measurements of galactic rotation, and the foreground Mg II absorption in the quasar spectrum. To facilitate a comparison of the galactic and circumgalactic gas kinematics, we have rotated the images to align the LRIS slitlet with the spatial axis of the PV diagram. We chose the orientation that places the quasar sightline to the right of the target galaxy. Since we will argue that modeling the velocity width presents a key challenge to understanding the physical origin of the absorption, we illustrate the instrumental broadening in all the figures. In Figure 2.1, the instrumental resolution of LRIS broadens the intrinsic Mg II line profiles as illustrated by the cyan bars in Figure 2.1; the orange bars represent the intrinsic line widths, for which we discuss the resolution correction in Section 2.4.2. Several results follow directly from the measurements shown in this figure.

We detected Mg II absorption in 13 of the 15 quasar sightlines. Most of these sightlines probe the CGM of isolated galaxies. Figure 2.2 illustrates the location and strength of the absorption relative to the major axis. The strongest absorber is the merger, J160951+353838.

Throughout the manuscript, the yellow diamonds identify two systems with uncertain host galaxy assignments. The J091954+291408 sightline intersects a group, see Section 2.4.2, and our spectrum detects two absorption systems. The statistical relationships between absorber and galaxy properties (Lan et al. 2014) suggest that our target

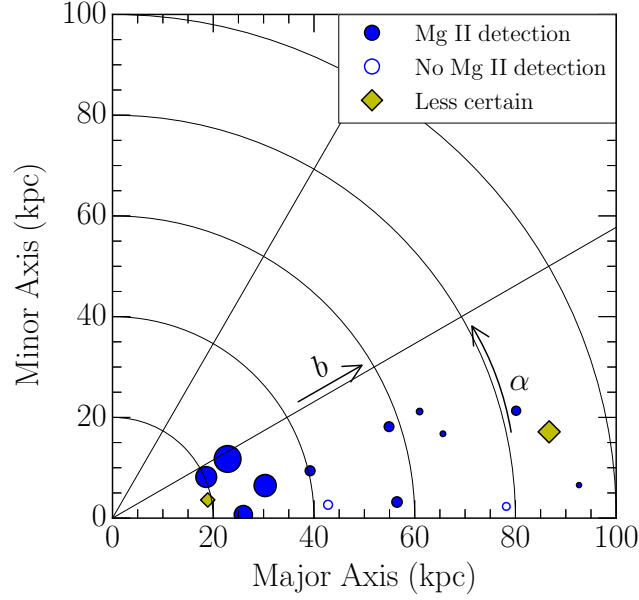


Figure 2.2: Ensemble of sightlines. The LRISb spectra detect Mg II absorption at impact parameters from 19 to 93 kpc near the galaxy major axis. All measured equivalent widths and upper limits lie within one standard deviation from the mean equivalent width – impact parameter relations. The apparent decrease in the covering fraction with impact parameter is therefore largely a sensitivity issue related to the decrease in mean absorption strength with the impact parameter. The filled and unfilled markers represent detections and non-detections respectively. The yellow diamonds flag the uncertain systems as described in the text. Each marker size scales with the rest-frame equivalent width  $W_r^{2796}$  (detection) or its  $2\sigma$  upper limit (non-detection).

has a 50% chance of being the source of either system. The bright, red galaxy and our target have essentially the same impact parameter ( $b = 88$  kpc), and red and blue galaxies are equally likely to produce the measured absorption strengths ( $W_r(2796) = 0.52$  and  $0.22 \text{ \AA}$ ). We assign the stronger system to the blue galaxy (our target) and flag the weaker system as potentially mis-assigned, i.e., not produced by our target. We also flag the J124601+173156 sightline through the richer group that includes galaxy J124601+173152. Bordoloi et al. (2011) found that overlap of the circumgalactic media of group galaxies flattens the radial decline in absorption strength. This sightline inter-

sects our target galaxy at  $0.14r_{vir}$ , and the contribution from the CGM of the other likely members (at  $r > 0.70r_{vir}$ ) is likely small. Our primary concern is the object between the quasar and the target galaxy. SDSS DR9 classifies this object as a star. We have yet to spectroscopically verify its stellar nature, and an identification as a compact galaxy would change our interpretation.

### 2.3.1 Evidence for Rotation

We explore the connection between the CGM kinematics and the angular momentum vector of the galactic disk. We detect 14 Mg II systems in 13 sightlines. We exclude the two flagged systems. Since only one of the two systems along the J091954+291408 sightline is excluded, 12 systems in 12 sightlines remain in our analysis. Among these 12 sightlines, the Doppler shift of the Mg II absorption is offset more than  $20 \text{ km s}^{-1}$  from the galaxy velocity in eight sightlines. Inspection of Figure 2.1 shows that the sign of the Mg II Doppler shift always matches the sign of the galactic rotation on the quasar side of the major axis.

Contrast this result with expectations for clouds on random orbits in a spherical halo. The shot noise from individual clouds would align the Doppler shifts half the time and produce anti-alignments in all other sightlines. Taking the probability of alignment in any one sightline as  $p = 0.50$ , the chance of finding eight alignments among 12 sightlines is just 12%.

Consideration of the systems without a net Doppler shift further lowers the odds



of obtaining our data from a random, spherical cloud distribution. Our measurement errors on the systemic velocities for four systems – J135734+254204, J142501+382100, J15471+343357, and J160951+352843 – are comparable to the uncertainties in the net Doppler shift of the Mg II absorption. It seems unlikely that higher S/N ratio data would reveal anti-correlations in all four of these systems. The true number of (projected) angular momentum alignments among our 12 sightlines very likely exceeds eight.

Our work was motivated in part by the pioneering study of Steidel et al. (2002) who published rotation curves for the hosts of five Mg II absorbers at  $z \approx 0.5$ . Three of their systems had azimuthal angles and disk inclinations consistent with our selection criteria, and the Doppler shifts of all three of these Mg II systems share the sign of the galactic rotation. With alignments now detected in 11 of our combined 15 sightlines, we can conclude that the circumgalactic gas clouds do not follow random orbits. The data require a component of angular momentum that appears to be aligned with the gas disk of the galaxy. A qualitatively similar trend, though quantitatively less significant, has also been seen at larger azimuthal angles (Kacprzak et al. 2010, 2011); and we will quantify the dependence on azimuthal angle in future work.

### **2.3.2 Comparison to Galaxy Masses**

In our study, the absorption systems span a very broad velocity range compared to the thermal line width. We interpret the broad line widths as evidence that many clouds contribute to each absorption system. The resulting picture requires a population of

clouds to produce each Mg II system. If the circumgalactic clouds follow random orbits in a roughly spherical halo, for example, then the line widths would reflect the depth of the gravitational potential while the Doppler shifts would be near the systemic velocity. The shot noise resulting from the finite number of clouds could produce net Doppler shifts along single sightlines, but no average shift would be measured.

To compare the velocity range of the Mg II absorption to the motion of clouds in virial equilibrium, we estimated the halo mass and virial radius of each galaxy. We adopted a stellar mass–halo mass relation derived from abundance matching Behroozi et al. (2010, hereafter B10). We obtained a median halo mass of  $\log(M_{vir}/M_\odot) = 11.51$ , which is significantly lower than the canonical quenching mass of  $10^{12} M_\odot$  (Conroy & Wechsler 2009; Yang et al. 2012; Kravtsov et al. 2014). We note that the scatter of individual galaxies around the mean stellar mass–halo mass relation introduces an uncertainty of  $\pm 0.30$  dex on any single halo mass estimate. This error is in addition to the statistical errors listed in Table 2.4.

We define the virial radius for each halo by

$$r_{vir} = M_{vir}(z)^{1/3} \left( \frac{4\pi}{3} \Delta_{vir}(z) \rho_c(z) \right)^{-1/3}. \quad (2.3)$$

The B10 definition of the virial mass follows Bryan & Norman (1998) who define the overdensity  $\Delta_{vir}(z)$  with respect to the critical density at redshift  $z$  by the expression

$$\Delta_{vir} = 18\pi^2 + 82x - 39x^2, \quad (2.4)$$

$$x = \Omega(z) - 1 \quad \text{and} \quad \Omega(z) = \rho_m(z)/\rho_c(z), \quad (2.5)$$

where  $\rho_m(z)$  and  $\rho_c(z)$  are the mean matter density and critical density at redshift  $z$ . For example,  $\Delta_{vir} \approx 119$  at  $z = 0.2$  ( $\Delta_{vir} \approx 273$  with respect to mean matter density). We list estimates of  $r_{vir}$  for individual galaxies in Table 2.4. The median halo virial radius for the 15 galaxies is 160 kpc, and the quasar sightlines intersect the CGM at impact parameters of 0.1–0.5  $r_{vir}$ .

The line-of-sight velocity dispersion through a halo of specified  $M_{vir}$  and  $r_{vir}$  depends on the mass distribution. In this section, for simplicity, we describe the halo profile as a singular isothermal sphere truncated at the virial radius  $r_{vir}$ . The resulting halo circular velocity,

$$V_{c,vir} = \sqrt{GM_{vir}(r_{vir})/r_{vir}}, \quad (2.6)$$

stays constant with radius. In virial equilibrium, the 3D velocity dispersion of the gas clouds would be  $\langle v^2 \rangle = 3kT/(\mu m_H)$ . We adopt the isotropic velocity dispersion in one dimension,

$$\sigma_v^2 = \frac{\langle v^2 \rangle}{3} = \frac{V_{c,vir}^2}{2} \quad (2.7)$$

as our estimate of the line-of-sight velocity dispersion along the quasar sightline.

Figure 2.3 illustrates the velocity dispersion of the Mg II systems over the mass range of our sample. Except for the J103640+565125 sightline and the two systems already flagged as potentially associated with galaxies other than our primary target, the velocity spread of the Mg II absorption along each of the other 11 sightlines is similar to the range predicted for clouds in virial equilibrium. In virial equilibrium, we would also expect the velocity range to broaden with increasing halo mass, and the data do not contradict this

expectation.

Our results probe a relatively small range in halo and galaxy properties, but we find no contradictions to virial equilibrium in this regime. In contrast, absorber–galaxy cross-correlation studies have reported an inverse correlation between absorber strength (i.e., velocity width) and the mean halo mass (Bouché et al. 2006; Gauthier et al. 2009), prompting much discussion regarding the virialization of the clouds making up Mg II systems (Bouché et al. 2006; Chen et al. 2010; Tinker & Chen 2010). We note only that a more recent analysis of absorber–galaxy catalogs shows there is no anti-correlation between Mg II equivalent width and virial mass (Churchill et al. 2013).

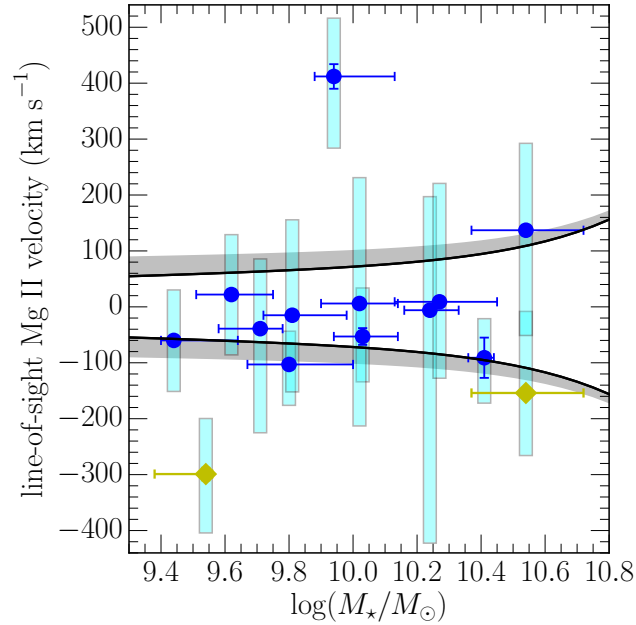


Figure 2.3: Velocity range of Mg II systems compared to halo velocity dispersion. The black lines illustrate the velocity dispersion of the halo (Equation (2.7)) with an assumed redshift of  $z = 0.2$ ; the shading represents convolution with the spectral resolution. The observed velocity range of the Mg II absorption is consistent with the velocity dispersion of virialized clouds. Note that  $\sigma_v$  is a mass-weighted mean velocity, so we expect some absorption at larger velocities. All except one of the Doppler velocities (blue points) lie within the expected range.

Figure 2.4 compares the velocity width of the absorption troughs to the halo escape velocity,  $v_{esc}(r) = \sqrt{2|\Phi(r)|}$ . The gravitational potential of the halo,  $\Phi(r)$ , has been calculated for the isothermal halo profiles at three radii chosen to span our range of the sightline impact parameter. Clearly, the Doppler shifts of the low-ionization-state absorption indicate that the clouds are expected to be bound to the halos. We add that directly matching the projected distance of each sightline with the escape velocity curves is a conservative comparison because the larger galactocentric radius of the cloud in 3D places it in a region of the halo with lower escape velocity,  $v_{esc}(r_{3D}) < v_{esc}(b)$ .

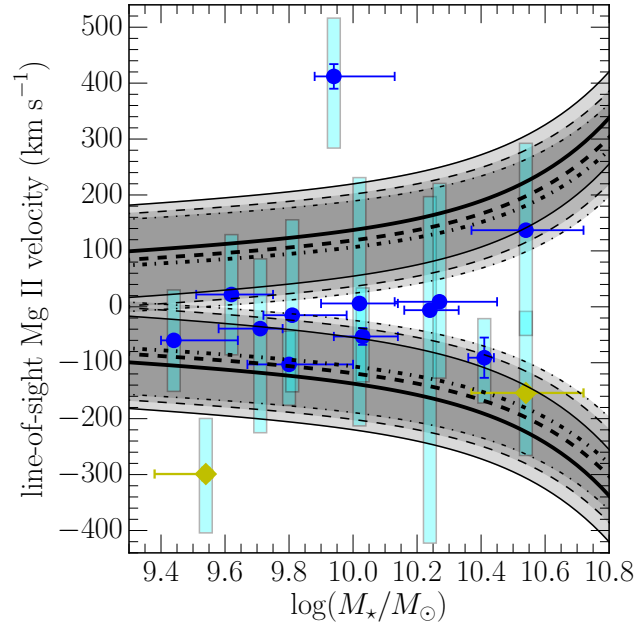


Figure 2.4: Comparison of low-ionization-state gas kinematics to the halo escape velocity. For purposes of illustration, we assume that the clouds move isotropically and plot the line-of-sight component of the escape velocity,  $v_{esc}/\sqrt{3}$ . A redshift of  $z = 0.2$  is assumed for the models. Symbols are as in Figure 2.3. The solid, dashed, and dotted-dashed lines are the escape velocities at galactocentric radii of 30, 60, and 90 kpc. The gray bands illustrate convolution with the line response function of the spectrograph. For the pairs without large systemic velocity uncertainties, most of the measured velocity ranges of the low-ionization-state gas are less than the escape velocity.

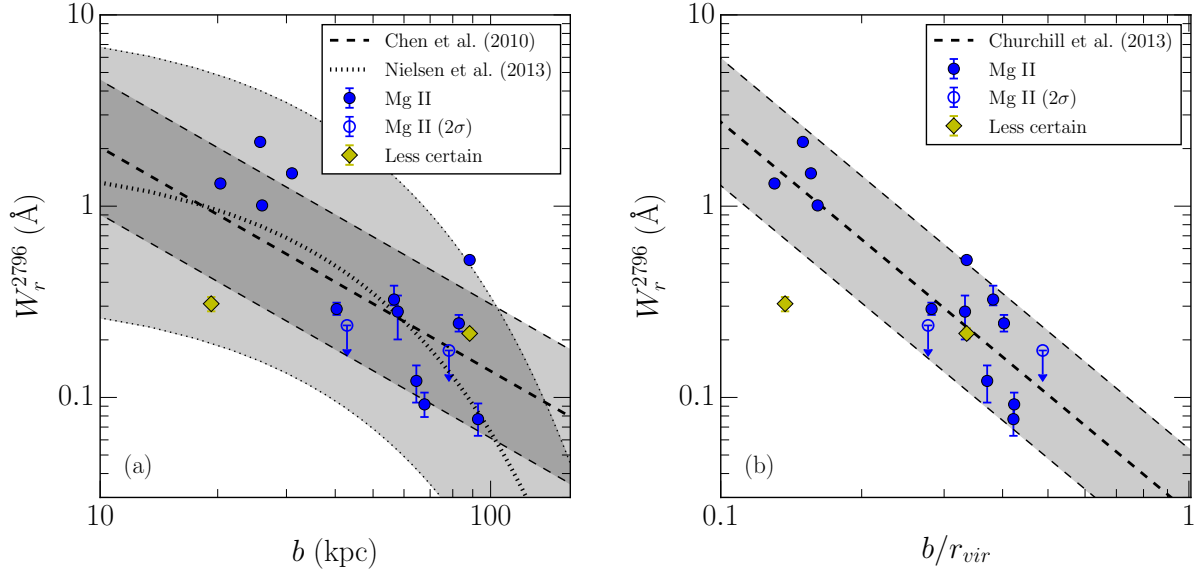


Figure 2.5: Decline in rest-frame equivalent width of Mg II absorption with (normalized) impact parameter. The filled markers represent detections, and the unfilled markers show the  $2\sigma$  upper limits for non-detections. The yellow diamonds flag the uncertain systems as described in the text. In panel (a), the thick dashed and dotted curves show the fitted correlations from Chen et al. (2010) and Nielsen et al. (2013), respectively. The shaded regions show the corresponding root-mean-square residual between the data and the fit in Chen et al. (2010), and the square root of the variance of the data relative to the fit in Nielsen et al. (2013). In panel (b), the thick dashed line and the shaded region represent the fitted relation and square root of the variance of data relative to the fit in Churchill et al. (2013).

### 2.3.3 The Covering Fraction of Low-ionization-state Gas

Of the 15 sightlines, seven show strong absorption,  $W_r(\lambda 2796) \geq 0.3 \text{ Å}$  (Nestor et al. 2005). Since all of our sightlines would easily detect strong absorption, one could claim a covering fraction close to 50%. However, the absorption strengths decrease with impact parameter, following a well-known trend illustrated in Figure 2.5(a). Our covering fraction measurement accounts for both this radial trend and size differences among the host galaxies. In Figure 2.5(b), we normalize the impact parameter by the halo virial radius. The strength of the detected absorption is typical for the impact parameters.

Figure 2.5 shows upper limits for the two non-detections. Since these upper limits fall within a standard deviation of the mean relation, we cannot exclude typical Mg II absorption along these sightlines. Our results are therefore consistent with a unity covering fraction. This high major-axis covering fraction applies to the inner CGM. Our largest impact parameters are 83 kpc (0.24 Å, J142501+382100) and 93 kpc (0.08 Å, J123049+071036).

## 2.4 Discussion: Circumgalactic Gas Dynamics

We established in Section 2.3 that our Mg II detections probe circumgalactic gas largely in virial equilibrium with the target galaxies. However, the orbits of these gas clouds are not random, rather their Doppler shifts show a positive correlation with the sign of each galactic rotation curve.

These kinematic properties of the CGM appear to be consistent with several decades of published literature on intervening absorption systems. For example, surveys of quasar fields traced intervening Mg II absorption to the halos of bright ( $0.7L_B^*$ ) galaxies at intermediate redshifts, e.g., Steidel et al. (1994). However, a deeper understanding of profile widths and their notable asymmetries (Lanzetta & Bowen 1992) generated debate between proponents of extended disk models (Prochaska & Wolfe 1997) and those favoring more spherical halos (McDonald & Miralda-Escudé 1999). As it turned out, adding a rotational component to the population of clouds proved to be the key to describing the statistical properties of the Mg II line profiles. This solution, however, did not distinguish

between rotating disks, halos, or hybrid descriptions (Charlton & Churchill 1998).

Our selection criteria – specifically (1) inclined disks, (2) low azimuthal angles for the sightlines, and (3) low impact parameters – clearly favor the detection of extended disks. Thus, rather than re-visiting the disk vs. spheroid quandary with a small number of sightlines, we simply explore the conjecture that major-axis sightlines primarily select gas clouds in the extended plane of galactic disks. In this section, we further explore the relationship between the angular momentum of circumgalactic gas and galactic disks.

Our discussion focuses on the measured velocity range and centroid of Mg II absorption in 11 CGM sightlines. We assume that J091954+291345 produces the stronger of the two components in the J091954+291408 sightline and predict that one of the neighboring galaxies in the field will turn out to have a redshift closer to that of the weaker absorption component. We exclude the flagged J124601+173156 sightline from the discussion in this section because the Mg II absorption appears to be associated with a galaxy at smaller angular separation from the quasar than our target galaxy. We defer discussion of the J103640+565125 sightline until we obtain high-resolution imaging because the other targets with such high velocity components have turned out to be groups or mergers. We also note evidence for a galaxy interaction with J160951+353838, which may be related to the unusually broad and strong absorption.



### 2.4.1 Angular Momentum of Circumgalactic Gas

Our observations do not directly determine the location of the clouds along each sightline. To gain insight about their relationship to the galaxy, we consider the conjecture that the clouds populate the extended plane of the galactic disk, calculate their implied galactocentric radius and circular velocity, and then examine the implications for the dynamical state of the gas.

Figure 2.6 compares the implied rotation speed of the Mg II systems to the rotation speed of the galactic disk. As described in Section 2.4.1, the Doppler shifts of the Mg II systems share the sign of the galactic rotation along seven sightlines. The measurement errors for four systems are consistent with no net Doppler shift, and these systems have substantial equivalent width on both sides of the systemic velocity. The range of deprojected Mg II velocities often reaches the asymptotic rotation speed of the disk. The Doppler shift of most of the absorption equivalent width is, however, too low to be consistent with purely circular orbits in a disk.

In Figure 2.7, we have normalized the galaxy rotation curves by the asymptotic rotation speed,  $v_{rot}$ , of each galaxy. The red squares show the halo circular velocity assuming a Navarro, Frenk, and White (Navarro et al. 1996) halo profile with the concentration parameter  $c(z, M_{vir})$  calculated using the python package **Colossus** introduced by Diemer & Kravtsov (2015).<sup>9</sup> The halo circular velocity resembles the form of Equation (2.6) but

---

<sup>9</sup> (Diemer & Kravtsov 2015, hereafter DK15) adopt  $M_{200c}$  to describe a halo with a mean density 200 times the critical density and model the corresponding concentration parameter  $c_{200c}$ , but Behroozi et al. (2010) define halo mass differently. **Colossus** provides the conversion of halo concentration between different mass definitions, for which the discussion in Appendix C of DK15 suggests that the inaccuracies

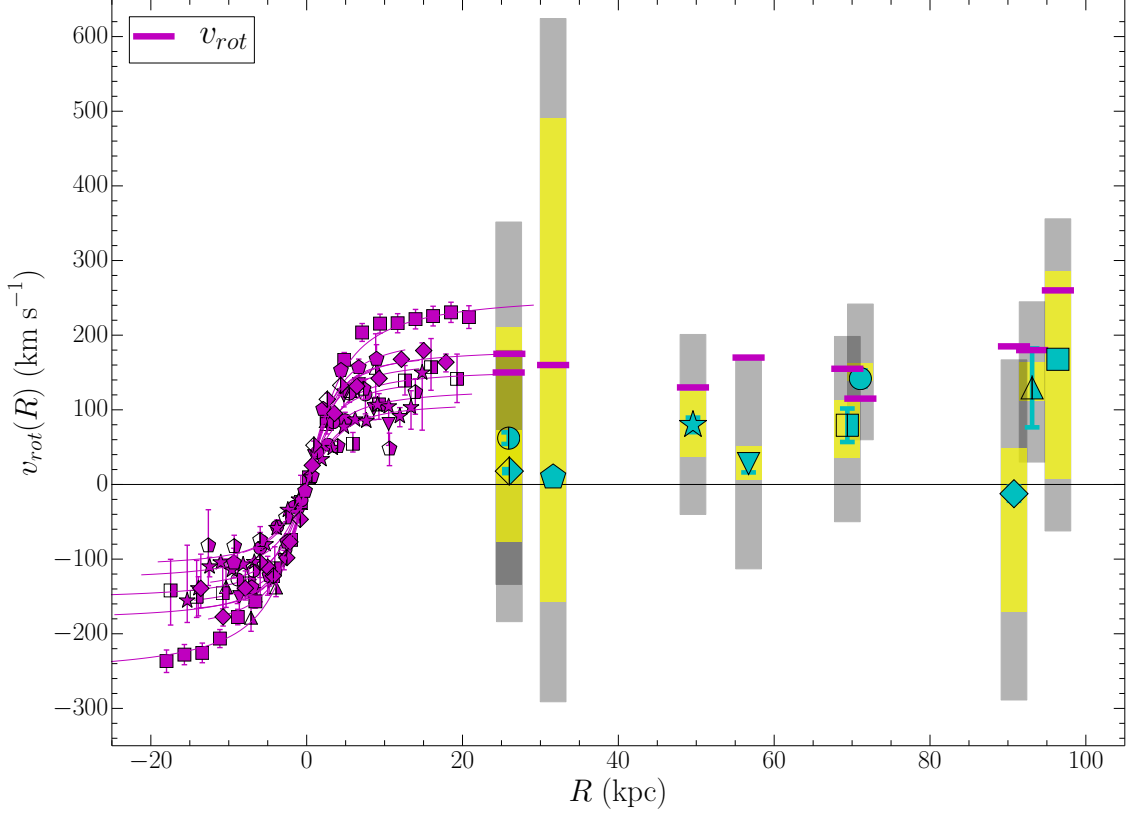


Figure 2.6: Comparison of circumgalactic gas kinematics to galaxy rotation. For purposes of illustration, we have deprojected the Doppler shift and impact parameter of each Mg II system to a circular velocity and galactocentric radius. In other words, the Mg II velocity here represents the tangential motion in the disk plane that would give the observed Doppler shift when projected onto the quasar sightline. For purposes of uniformity in this figure, galactic rotation curves are defined with a positive velocity on the quasar side of the major axis. The symbol for each sightline is the same as in the PV-diagrams in Figure 2.1, but all measurements are now deprojected onto the disk plane. The yellow (gray) bars indicate the deconvolved (measured) width of each absorption complex; these can be compared to the extended rotation curves indicated by the magenta bars. Note that we omit J160951+353843 in this figure and Figure 2.7 because the large absorption strength and width stand out from all the other sightlines; the measured velocity range requires expanding the  $y$ -axis making it less possible to distinguish the individual rotation curves.

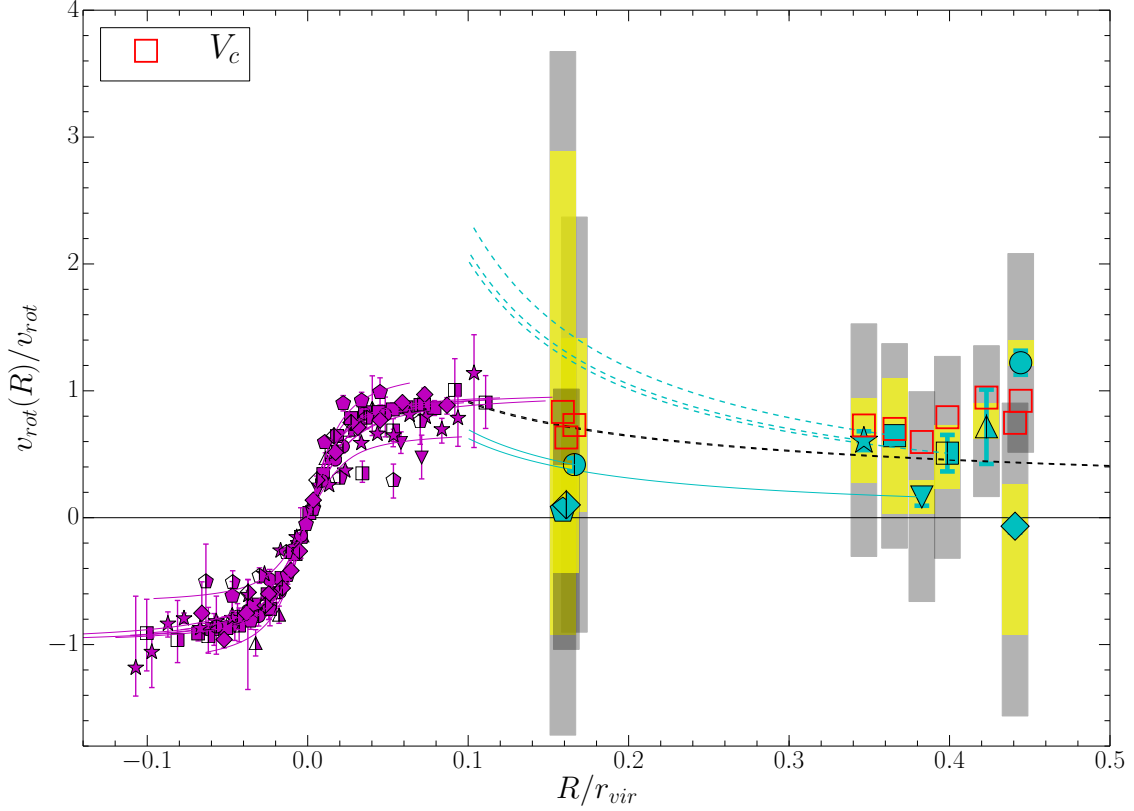


Figure 2.7: Comparison of disk and halo angular momentum. Similar to Figure 2.6, but this diagram shows the normalized rotation speed as a fraction of the halo virial radius. The points show our models of the actual rotation speed in the halo accounting for the dark matter halo (red squares); the Keplerian fall off from the measured rotation curve sets a lower limits on the rotation speed in the CGM (dashed, black line). The cyan curves illustrate constant  $Rv_{rot}(R)$  and show that the infalling gas would have specific angular momentum at least as large as that in the galactic disk.

with a radial dependence,

$$V_c(r) = \sqrt{GM_{vir}(r)/r}. \quad (2.8)$$

Most of the Mg II equivalent width is detected at Doppler shifts less than that generated by clouds on circular orbits. The velocity widths of the systems are broad enough to include gas on a circular orbit, but the estimated speed of a circular orbit exceeds the centroid velocity (cyan symbols in Figure 2.7). Adding the stellar mass from Table 2.4 to the halo mass raises the circular velocity slightly (2 – 6%) and increases the magnitude of the discrepancy. Only the sightline probing the CGM at the largest radius provides an exception. At  $R/r_{vir} \approx 0.45$ , the J084723+254105 sightline has a Doppler shift larger than expected from circular orbits.

If clouds near the disk plane with  $R/r_{vir} \lesssim 0.45$  are not fully described by circular orbits, then what can we say about their dynamical state? Since we have shown that the velocity spread of the systems is consistent with virial motion, we can conclude that the clouds have a significant velocity component that is perpendicular to any tangential motion in the disk plane. We suggest radial inflow as a physically likely origin for this extra velocity component. While the spectral line profiles do not uniquely distinguish radial inflow from other velocity vectors, we argue that our selection of major-axis sightlines favors this solution.

If our interpretation is correct, then it has implications for how galaxies get their gas.

We illustrate where the infalling gas might obtain a circular orbit by drawing curves of

---

of these conversions are no more than  $\sim 20\%$ .

constant angular momentum in Figure 2.7. By following these curves, we see that some of the gas detected in Mg II absorption has specific angular momentum comparable to the galactic disk. The broad line widths, however, indicate that other clouds might obtain circular orbits at radii several times that of the visible galactic disk. Large gas disks have been detected in H I 21 cm observations of nearby spiral galaxies. If we have detected extended gas disks at  $z \approx 0.2$ , then the composition of the gas is clearly not pristine implying significant metal recycling.

### 2.4.2 The Tension between the Velocity Widths of Mg II Absorbers and Rotating Disks

Figure 2.8 illustrates the velocity spread of our Mg II absorption troughs relative to the systemic velocities of the associated galaxies. We have added published observations of sightlines with  $\alpha \leq 30^\circ$  near inclined, star-forming galaxies. We do not include sightlines from the COS Halos survey (Tumlinson et al. 2011, 2013; Werk et al. 2013, 2014) because no measurements of galaxy rotation have been published. As introduced in Section 2.4.1, three sightlines from Steidel et al. (2002, hereafter S02) satisfy our selection criteria. At intermediate redshifts, we add two sightlines from Kacprzak et al. (2010, hereafter K10); and, at lower redshift, we found one sightline from Kacprzak et al. (2011, hereafter K11). Little data of this type exists at higher redshifts, but two ground-breaking papers suggest that similar trends may be present in the low-ionization-state absorption. Just  $20^\circ$  off the major axis of a  $z = 2.3283$  galaxy, Bouché et al. (2013) detected absorption from low

ions (but did not cover Mg II) at an impact parameter of 26 kpc. The Doppler shift of the main absorption component is  $180 \text{ km s}^{-1}$  and in the same direction as the galactic rotation, whereas the total absorption spans from  $-35 \text{ km s}^{-1}$  to  $+300 \text{ km s}^{-1}$ . Just 12 kpc from a  $z = 0.9096$  galaxy, Bouché et al. (2016) resolved the Mg II line profile in a sightline  $15^\circ$  off the major axis. The Doppler shift is again in the same sense as the galaxy rotation, and the velocities range from  $-230 \text{ km s}^{-1}$  to  $+265 \text{ km s}^{-1}$ .

Differences in instrumental resolution among these observations affect the measured velocity widths of the absorption troughs. We have attempted to correct all observations to the same effective resolution in Figure 2.8. In the left panel of Figure 2.8, we have simply degraded the spectra of bright quasars taken using Keck/HIRES or VLT/UVES ( $v_{\text{res}} \simeq 6 \text{ km s}^{-1}$ ) to our resolution by convolving with the LRIS line-spread function. The inverse process – recovering the intrinsic velocity width of a system from our lower resolution spectra – is inherently more noisy. We show the results of this exercise in the right panel of Figure 2.8. The observations reported by K11 were also obtained with Keck/LRIS at a spectral resolution ( $v_{\text{res}} \simeq 155 \text{ km s}^{-1}$ ) similar to our median resolution. Section 4.1 of the K11 paper convincingly argues that these LRIS line widths should be decreased by  $85 \text{ km s}^{-1}$  on both sides before they are compared to well resolved line profiles. We have confirmed that simply fitting the Mg II absorption with a Gaussian profile convolved with the LRIS line spread gives a consistent velocity width. After taking instrumental broadening into account, we find that four of our 11 systems show absorptions at velocities on both sides of the galaxy systemic velocity.

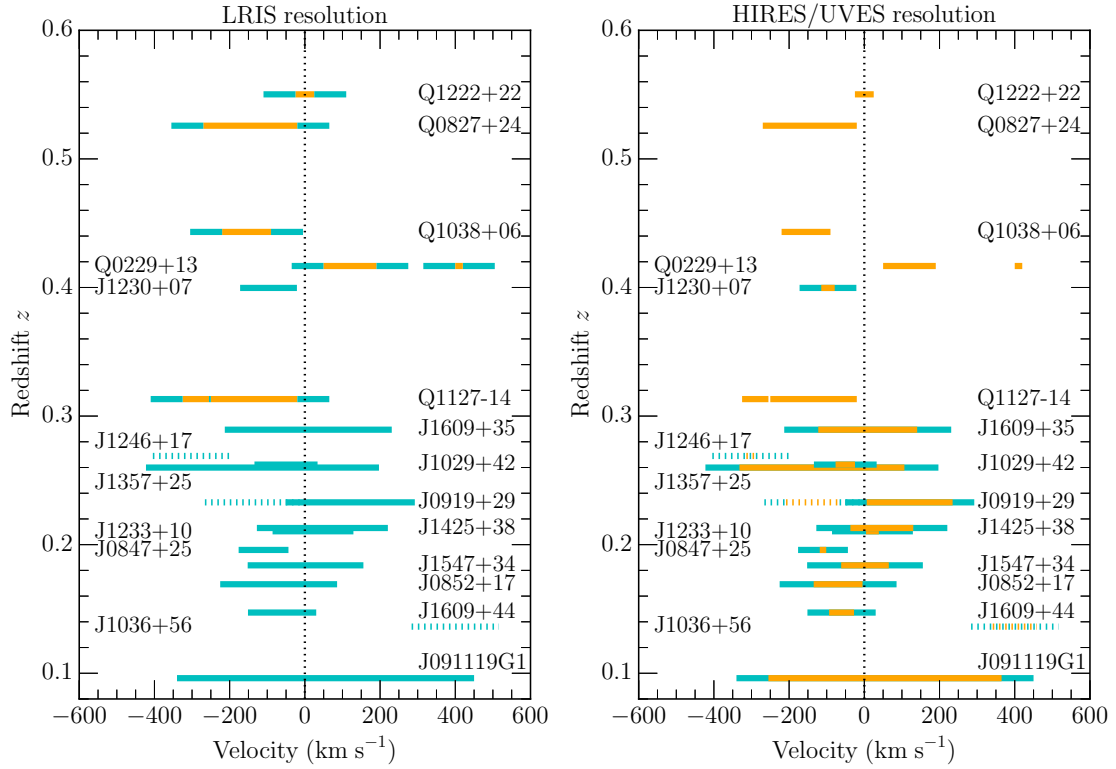


Figure 2.8: Velocity range of major axis Mg II absorption. Our results for 11 sightlines (solid bars) are compared to previously published measurements over a range of redshift. Significant absorption is detected to both sides of the systemic velocity for all low redshift galaxies observed; in contrast, the velocity ranges are one-sided in S02 and K10. *Left Panel:* Comparison at moderate spectral resolution. Broadening of the echelle spectra by the LRIS instrumental resolution is illustrated by the cyan bars. *Right Panel:* Comparison at high spectral resolution. To illustrate the LRIS instrumental broadening (cyan), we scale the correction factor derived in K11 to the LRIS spectral resolution of each run. The orange bars are our best estimate of the intrinsic system velocity spread. Dashed lines represent the excluded absorption components or sightlines in our analysis in Section 2.4.

A dynamical description of the low-ionization-state gas kinematics must explain the following: (1) the correlation of the sign of the net Doppler shift with the galactic disk, (2) the broad line width, and (3) the generation of absorption on both sides of the systemic velocity. The simple disk model naturally satisfies the first criterion, but the other kinematic properties prove challenging to explain with the simple disk picture. For individual systems, we have explored two types of solutions: (1) adding a vertical velocity gradient to the disk rotation speed and (2) adding radial infall in the disk plane. We provide a mathematical description of these models in Appendix A. The solution space is highly degenerate. Rather than presenting every possible solution, we focus on answering a few well posed questions.

#### **2.4.2.1 Are There Sightlines that cannot be Fitted by Disk Rotation?**

Disk rotation can never produce a sign change in the line-of-sight velocity along a sightline. Equation (A.4) and diagrams in Appendix A demonstrate this fact quantitatively.<sup>10</sup>

We find four sightlines with absorption on both sides of the systemic velocity – J135734+254204, J142501+382100, J154741+343357, and J160951+353843, so the simple disk model cannot describe the velocity range of the Mg II absorption. The spherical halo model adequately describes these systems, and these sightlines need not intersect a disk at all. Nonetheless, we asked whether an extended disk with radial inflow provided a viable alternative explanation of the line widths. We found that inflow

---

<sup>10</sup> Poor spectral resolution could certainly smear the line profile so that it crossed the systemic velocity. In principle, turbulence could provide a physical mechanism to accomplish this line broadening, but requiring turbulent velocities comparable to the circular velocity implies a structure that cannot really be labeled a disk.



( $v_R = -250 \text{ km s}^{-1}$ ) in a thick disk ( $2H_{\text{eff}} = 40 \text{ kpc}$ ) produces the velocity range of the J142501+382100 system. The other three systems required thicker disks and higher inflow speeds. The extreme values of these parameters lead us to conclude that extended disks are not a viable model for these systems.

For the systems with single-sided absorption, a rotating disk can describe the velocity range measured in five of the seven sightlines, albeit with a troubling implication. Recall that in Figure 2.8, the intrinsic line widths typically span around a hundred  $\text{km s}^{-1}$  or more. The problem is that the pathlength of a sightline through a thin disk is just the vertical thickness of the disk,  $2H_{\text{eff}}$  (as illustrated in the schematic diagrams in Appendix A), lengthened by the secant of the viewing angle. Unless we view the disk exactly edge-on, the intercepted velocity range will be small. We found that the simple disk model required disk thicknesses of the order of the virial radius – i.e., tall rotating cylinders rather than disks.

As demonstrated in S02 and in Appendix A, adding a scale-height  $h_v$  for the vertical velocity gradient such that the disk rotation speed decreases with increasing perpendicular distance from the disk midplane will bring the line-of-sight velocity  $v_{los}$  toward zero over a shorter pathlength along the sightline. As a fiducial reference point, we adopted  $h_v = 10 \text{ kpc}$ . For our measured range of rotation speeds, this choice of velocity scale height produces a vertical gradient between 11 and 26  $\text{km s}^{-1}$  per kpc. Above the plane of nearby spiral galaxies, the rotation lags the disk; our adopted  $h_v$  creates a vertical velocity gradient consistent with measurements of  $dv_\phi/dz = -8$  to  $-60 \text{ km s}^{-1}$  per kpc

(Oosterloo et al. 2007; Heald et al. 2011; Marasco & Fraternali 2011; Zschaechner et al. 2011, 2012; Gentile et al. 2013; Kamphuis et al. 2013; Zschaechner & Rand 2015). With this velocity gradient in the extraplanar gas, we found solutions with very thick disks and reduced the median  $H_{\text{eff}}$  to 20 kpc (for the models fitted to the five disks).<sup>11</sup> We also found an alternative picture, however, which appears at least as plausible in our opinion. When a radial inflow component was allowed, the median  $H_{\text{eff}}$  dropped to 10 kpc, and the range of inflow speed ranged from 40 to 180 km s<sup>-1</sup>.

Figure 2.9 illustrates the failure of the thick disk model for the other two Mg II detections. The thick disk model cannot describe the J084723+254105 system because the large blueshift of the absorption exceeds the projected rotation speed ( $v_{\text{rot}} \sin i = 115 \text{ km s}^{-1} \sin(52^\circ) = 91 \text{ km s}^{-1}$ ). The bottom row of Figure 2.9 illustrates a slightly different mode of failure for the thick disk model. Toward the sightline associated with J123318+103542, the absorption velocities do not reach the projected circular velocity of the galactic disk. In the center panels of Figure 2.9, we successfully fit these two systems by introducing radial infall in the disk plane. The observed line-of-sight velocities are the projection of the total velocity vector produced by the addition of rotation and inflow in the disk plane. Whether the infall boosts or cancels the projected circular velocity depends on geometry. The Appendix clearly illustrates the origin of this asymmetry; we could not find it described previously in the literature. This solution has a reasonable disk of thickness  $H_{\text{eff}} = 5 \text{ kpc}$  and  $H_{\text{eff}} = 2 \text{ kpc}$ , with the velocity scale height  $h_v = 10 \text{ kpc}$

---

<sup>11</sup> The total vertical thickness of the disk is  $2H_{\text{eff}}$ ;  $H_{\text{eff}}$  measures the disk thickness from the disk midplane.

in the models for J084725+254104 and J123318+103542 respectively. The corresponding inflow speeds are  $v_R = -140 \text{ km s}^{-1}$  and  $v_R = -1120 \text{ km s}^{-1}$  in the two models.

#### **2.4.2.2 Is Radial Inflow Excluded When it is not Required?**

A rotating disk with radial infall provides a plausible description of the Mg II kinematics in our two systems that cannot be fit with simpler models. While the other systems do allow simpler descriptions, we emphasize that the implied parameters generate tension with our expectations for real disks. Without inflow, the five systems described by rotating disks require very thick disks, and we suggest solutions with thinner disks and inflow as a viable alternative. The same picture, inflow in a rotating gas disk, can reproduce broad absorption centered near the systemic velocity. We do not favor this interpretation for those four sightlines because simpler models remain consistent with our observations; we simply emphasize that, *no*, we do not exclude this interpretation for a single sightline.

#### **2.4.3 Implications for How Galactic Disks Get Their Gas**

The gas flows in simulations of galaxy formation motivated us to consider the observational signature of gas flows near the plane of the galactic disk. We observed the CGM along sightlines near the galactic major axis in an effort to select such disks if they exist. We demonstrated that this circumgalactic gas has a component of angular momentum in the same direction as the disk angular momentum. If the gas clouds follow circular orbits in the extended plane of the galactic disk, however, their Doppler shifts would be larger

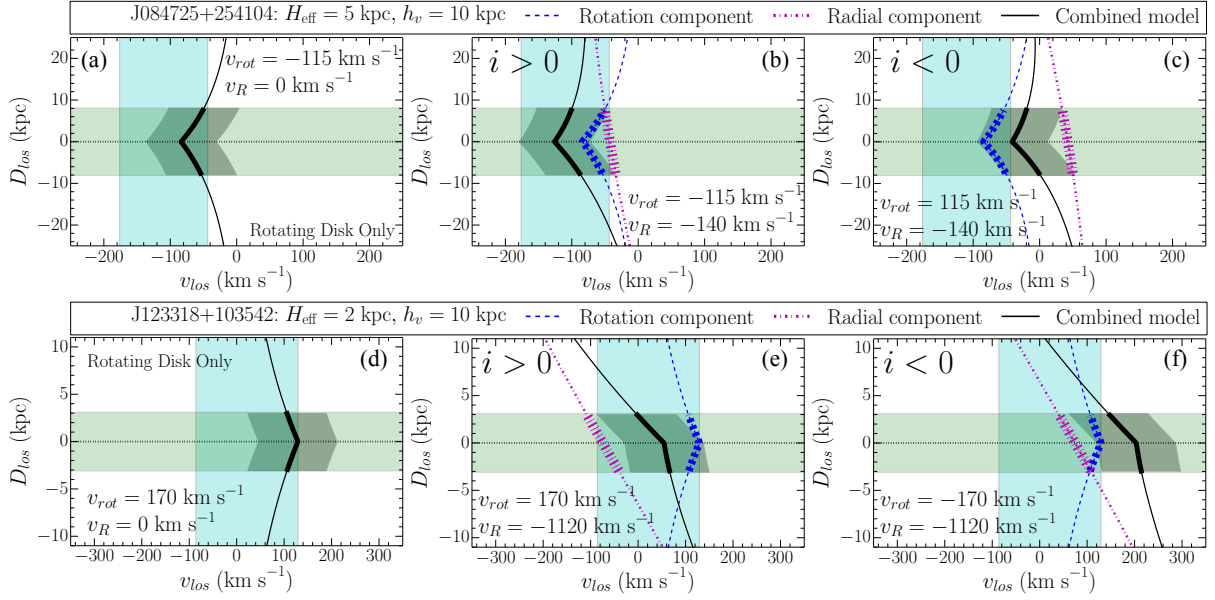


Figure 2.9: Examples of the infall solution for the kinematics of absorption-line systems. The cyan shading shows the observed line-of-sight velocity range for galaxy J084725+254104 (top row) and J123318+103542 (bottom row) along their corresponding quasar sightlines. Left columns illustrate the failure of the simple disk model. The disk of J084725+254104 rotates too slowly to produce the large Doppler shifts observed. The rotation speed of the J123318+103542 disk creates a large Doppler shift than we observe. Middle and right columns contrast the two signs of the disk inclination. To reproduce the velocity range of the Mg II absorption (cyan), the inflow model (bold black line) requires a positive sign of the disk inclination. The opposite tilt of the disk produces absorption that is too redshifted along both sightlines. We adopt the right-handed coordinate system for which  $v_{rot} > 0$  produces an angular momentum vector along the positive  $z$ -axis of the disk, where the positive  $z$ -axis always points toward the quasar side of the disk and is perpendicular to the disk plane. The sign flip of the disk inclination therefore changes the sign of  $v_{rot}$  in the model (see the Appendix for more detail). In each position-velocity diagram ( $D_{los}$  vs.  $v_{los}$ ), the green shaded region indicates the portion of the sightline intersecting the disk. The gray band illustrates the convolution of the modeled line-of-sight velocity with the line response function of the spectrograph.

than observed. One interpretation of this result is simply that the angular momentum vector of the inner circumgalactic gas is only partially aligned with that of the disk. We suggest, however, that radial inflow in the disk plane provides another viable description of the observations.

The inferred mass flux depends directly on the column density. Since we generally obtained a very conservative lower limit on the column density, we estimate a lower limit of the mass flux. For purposes of illustration, we use solar metallicity (Morton 2003) and a unity ionization fraction of singly ionized magnesium, i.e.,  $N(\text{Mg}^+)/N(\text{Mg}) = 1$ .<sup>12</sup> Substituting the lower limits from Table 2.3, we infer hydrogen columns from  $6 \times 10^{16} \text{ cm}^{-2}$  to  $3 \times 10^{18} \text{ cm}^{-2}$ . We apply Equation (1) from Bouché et al. (2013). For the two systems that require inflow, the mass flux exceeds  $0.07\text{--}1 \text{ M}_\odot \text{ yr}^{-1}$ . If we interpret the five systems with single-sided absorption as inflow detections, then the mass fluxes are at least  $0.02\text{--}0.08 \text{ M}_\odot \text{ yr}^{-1}$ . In general, the true mass flux could be much, much larger; but we will need higher resolution spectra to produce accurate measurements.

In the context of this inflow picture, the new observations place some constraints on how galaxies get their gas. First, the inflow speeds we found were generally within a factor of two of the rotation speed. One sightline, quasar J123317+103538 associated with galaxy J123318+103542, required a much larger inflow velocity to cancel the tangential velocity. We remain skeptical of inflow velocities as large as  $1000 \text{ km s}^{-1}$ ; however, some high velocity clouds have velocities this large relative to the Local Stan-

---

<sup>12</sup> The ionization fraction  $N(\text{Mg}^+)/N(\text{Mg})$  varies between 0.1 and 1 (Murray et al. 2007; Martin et al. 2012).

dard of Rest (Wakker & van Woerden 1997). Second, in Figure 2.7, we sketched curves of constant  $RV(R)$  and then argued that some of the infalling gas would have to reach the galactic disk. Possible strategies for testing this picture include the following: (1) confirming/refuting the predictions for the disk inclination and spiral arm morphology, (2) examining the implications of the model for a broader range of azimuthal angles, and (3) significantly increasing the sample of major-axis sightlines.

Given the absence of previous evidence for gas inflow in galactic disks, this result if verified would have significant implications for how galactic disks get their gas. In this context, it is interesting to compare the galaxies in our sample to a younger version of the MW galaxy in the past. We use the stellar mass evolution function presented in van Dokkum et al. (2013). They study galaxies at different redshifts with the same rank order in stellar mass as the MW at  $z = 0$ , and adopt the stellar mass of the present-day MW as around  $5 \times 10^{10} M_{\odot}$ , i.e.,  $\log(M_{\star}/M_{\odot}) = 10.70$  (Flynn et al. 2006; McMillan 2011). They then associate galaxies at different redshifts by requiring them to have the same cumulative comoving number density. We use their approximate stellar mass evolution function

$$\log(M_{\star, \text{MW}}/M_{\odot}) = 10.7 - 0.045z - 0.13z^2 \quad (2.9)$$

to find the predicted stellar mass of the MW progenitors at  $z = 0.2$  as  $\log(M_{\star, \text{MW}}/M_{\odot})_{z=0.2} = 10.69$ , which is marginally lower than that at  $z = 0$ . This predicted stellar mass has an uncertainty of  $\sim 0.2$  dex. The comparison between our galaxy sample at  $z = 0.2$  and the MW progenitors at  $z = 0.2$  show that our median galaxy is 0.87 dex less massive

than the typical MW progenitor 2.5 Gyr ago; but the upper mass range of our sample is consistent with the expected masses of MW progenitors.

## 2.5 Conclusion

We presented new observations of 15 galaxy–quasar pairs. This study more than doubles the number of quasar sightlines studied within  $30^\circ$  of the major axis of star-forming galaxies. The focus on typical, star-forming galaxies allows us to consider the ensemble of sightlines as multiple sightlines through the same average CGM.

Gas clouds in the plane of these galactic disks are a plausible source of Mg II absorption detected in the quasar spectrum near the redshift of the foreground galaxy. Models predict that such gas has been accreted recently. We therefore asked the question of whether the gas kinematics might yield signs of accretion.

We detected Mg II absorption in 13 sightlines with  $W_r(\lambda 2796) \gtrsim 0.1 \text{ \AA}$ . The sign of the Doppler shifts of these systems always matched the sign of the galactic rotation on the quasar side of the major axis. This result demonstrated that the motion of the absorbing gas is not random. The observations do not require the absorbing clouds to be located in the plane of the galactic disk, but we focused our modeling effort on gas in an extended plane for two reasons: (1) these models offer the simplest geometry allowed by the data, and (2) numerical simulations of individual galaxies predict that gas accreted at late times feeds an extended gas disk. The Doppler shifts of the Mg II systems are less than expected for gas on circular orbits. If these clouds reside in the disk plane,

then they will spiral inwards through the disk. This inflow mechanism would broaden the absorption troughs.

The velocity widths of the Mg II systems typically agree with expectations for gas in virial equilibrium. Host galaxy mis-assignments plausibly explain the outliers. However, the velocity range poses a challenge for simple models. The velocity widths of two Mg II systems cannot be fit by a thick rotating disk model. Furthermore, modeling the widths of many systems requires the disk to be ridiculously thick, essentially morphing into a rotating cylinder that is much thicker than the disk radius.

We found that radial infall in the disk plane solves the above dilemmas. Other solutions may exist, but we argue that radial infall is the simplest geometry consistent with the data. These measurements provide a benchmark against which the accuracy of the gas accretion process in numerical simulations should be evaluated. Our future work will address how the circumgalactic gas kinematics depend on azimuthal angle.

This research was partially supported by the National Science Foundation under AST-1109288. G.G.K. acknowledges the support of the Australian Research Council through the award of a Future Fellowship (FT140100933). We thank the referee for the useful suggestions. We thank Mark Seibert for the discussion on GALEX photometry. We gratefully acknowledge conversations with Peng Oh and Andrey Kravtsov, which contributed to shaping our interpretation of these data. Most of the data presented herein were obtained at the W.M. Keck Observatory, which is operated as a scientific partner-



ship among the California Institute of Technology, the University of California and the National Aeronautics and Space Administration. The Observatory was made possible by the generous financial support of the W.M. Keck Foundation. The authors wish to recognize and acknowledge the very significant cultural role and reverence that the summit of Mauna Kea has always had within the indigenous Hawaiian community. We are most fortunate to have the opportunity to conduct observations from this mountain. Some presented data are based on observations obtained with the Apache Point Observatory 3.5 m telescope, which is owned and operated by the Astrophysical Research Consortium.

## Chapter 3

# Resolving 3D Disk Orientation using High-Resolution Images: New Constraints on Circumgalactic Gas Inflows

We constrain gas inflow speeds in star-forming galaxies with color gradients consistent with inside-out disk growth. Our method combines new measurements of disk orientation with previously described circumgalactic absorption in background quasar spectra. Two quantities, a position angle and an axis ratio, describe the projected shape of each galactic disk on the sky, leaving an ambiguity about which side of the minor axis is tipped toward the observer. This degeneracy regarding the 3D orientation of disks has compromised

previous efforts to measure gas inflow speeds. We present HST and Keck/LGSAO imaging that resolves the spiral structure in five galaxies at redshift  $z \approx 0.2$ . We determine the sign of the disk inclination for four galaxies, under the assumption that spiral arms trail the rotation. We project models for both radial infall in the disk plane and circular orbits onto each quasar sightline. We compare the resulting line-of-sight velocities to the observed velocity range of Mg II absorption in spectra of background quasars, which intersect the disk plane at radii between 69 and 115 kpc. For two sightlines, we constrain the maximum radial inflow speeds as 30-40 km s<sup>-1</sup>. We also rule out a velocity component from radial inflow in one sightline, suggesting that the structures feeding gas to these growing disks do not have unity covering factor. We recommend appropriate selection criteria for building larger samples of galaxy–quasar pairs that produce orientations sensitive to constraining inflow properties.

### 3.1 Introduction

Gas accretion onto galaxies shapes the growth of their disks. Decades of observations have demonstrated that galaxies need a continuous gas supply to explain the star formation history and the stellar metallicity distribution of the disks. Without a continuous gas supply, the gas reservoir around galaxies will exhaust within a few gigayears, and the galaxies cannot sustain their star formation rates (Bigiel et al. 2008, 2011; Leroy et al. 2008, 2013; Rahman et al. 2012). The accreting gas will thereby prolong the gas consumption time (Kennicutt 1983) and explain the color of galaxy disks along the Hub-

ble sequence (Kennicutt 1998). The infall of metal-poor gas also explains the relative paucity of low metallicity stars in the disk, known as the G-dwarf problem in the solar neighborhood (van den Bergh 1962; Schmidt 1963; Sommer-Larsen 1991) but not unique to the Milky Way (Worthey et al. 1996).

In hydrodynamical simulations, galaxies accrete cooling gas to grow the galactic disks (Oppenheimer et al. 2010; Brook et al. 2012; Shen et al. 2012; Ford et al. 2014; Christensen et al. 2016). The torques generated by the disk align the cooling, infalling gas with the pre-existing disk (Danovich et al. 2012, 2015). The newly accreted gas then forms an extended cold flow disk that corotates with the central disk (Stewart et al. 2011, 2013, 2017). As gas accreted at later times has higher angular momentum, the late time infall builds the disk inside-out (Kimm et al. 2011; Pichon et al. 2011; Lagos et al. 2017; El-Badry et al. 2018).

Direct observations of gas accretion onto galaxies remain sparse (Putman et al. 2012). Nevertheless, recent studies of the circumgalactic medium (CGM) through quasar sightlines have shed light on detecting the inflowing gas. The CGM extends to the galaxy virial radii (Tumlinson et al. 2017) and contains a significant fraction of the baryonic mass associated with the galaxy halos (Werk et al. 2014). For the low-ionization-state gas (e.g.,  $\text{Mg}^+$ ) detected as intervening absorption in quasar sightlines, absorption near the galaxy major and minor axes is often explained by inflows and outflows (e.g., Bouché et al. 2012; Kacprzak et al. 2012, 2015; Nielsen et al. 2015); minor- and major-axis sightlines intersect winds blown out perpendicular to the disk plane and gas accreted near

the disk plane, respectively (Shen et al. 2012). In addition, Paper IV studied the circumgalactic gas kinematics of a sample of 50  $z \approx 0.2$  blue galaxies, and the galaxies have quasar sightlines intersecting the inner CGM at all azimuthal angles.<sup>1</sup> They found that the Mg II absorption strength increases with the velocity range, both of which increase toward the minor axis. They concluded that minor-axis sightlines intersect the CGM kinematically disturbed by galactic outflows, a property that has been shown for galaxies undergoing or have recently undergone a strong starburst (Heckman et al. 2017).

Paper II studied a subset of 15 galaxy–quasar pairs from Paper IV, and all 15 quasar sightlines lie within  $30^\circ$  from the galaxy major axes. In 13 out of the 15 major-axis sightlines, Paper II detected Mg II absorption, and the Mg II Doppler shift shares the same sign as the galactic disk rotation at the quasar side of the galaxy. This implies that the Mg II gas in the inner CGM corotates with the galaxy disk. Moreover, Paper IV has found no net counter-rotating Mg II systems within  $45^\circ$  of the major axis. Therefore, our results have strengthened previous results from smaller, diverse galaxy samples that also found corotating low-ionization-state gas in major-axis sightlines (Steidel et al. 2002; Kacprzak et al. 2010; Bouché et al. 2013, 2016; Zabl et al. 2019), a property that also describes Ly $\alpha$  absorbers (Barcons et al. 1995; Prochaska & Wolfe 1997; Chen et al. 2005).

To explain the kinematics of the Mg II absorbing gas, Paper II explored simple models to describe the velocity range spanned by the absorption. We have adopted disk models, instead of rotating halo models, as the simplest configuration. This is motivated in part

---

<sup>1</sup> We define the azimuthal angle as the angle between the galaxy major axis and the line joining the quasar and the galaxy center.

by hydrodynamic simulations that show the corotation between the central disks and the extended cold gas disks (e.g., Stewart et al. 2011; El-Badry et al. 2018). Previous observational work has also attempted to model the Doppler shifts and/or velocity ranges of  $\text{Ly}\alpha$  and  $\text{Mg II}$  absorption systems with disk rotation (e.g.,  $\text{Mg II}$  in Steidel et al. (2002) and Kacprzak et al. (2010, 2011), and  $\text{Ly}\alpha$  in Barcons et al. (1995), Prochaska & Wolfe (1997), and Chen et al. (2005)). Despite the known problem where rotating gas on thin disks fails to reproduce the broad velocity ranges spanned by the absorption, previous works overcame this challenge by using variations of disk models, e.g., using thick disks (cylinders) instead of thin disks, introducing a lag in the rotation (i.e., a vertical velocity gradient), adding radial inflow on the disk plane, or a combination of these options (Steidel et al. 2002; Kacprzak et al. 2010, 2011; Paper II). We have selected major-axis sightlines that intersect the inner CGM of galaxies with inclined disks. If the gas disks extend beyond the visible disks of galaxies, then our sightlines will intersect gas near the extended disk planes at within half the virial radii. Therefore, motivated by previous work and our selection of major-axis sightlines, we adopt a disk geometry and explore the consequences for the gas dynamics.

With a disk geometry, the modeled line-of-sight (LOS) velocity depends on the galaxy disk orientation in 3D-space. In addition to the disk axis-ratio and position angle, establishing the 3D disk orientation requires the sign of disk inclination. The sign of disk inclination indicates how the galaxy disk tilts with respect to the plane of the sky. From the perspective of the observer, switching the sign flips the near side and the far side

of the galaxy disk; Figure 3.1 illustrates this concept. We have implemented this geometrical difference into our inflow model in Paper II. The model combines a tangential (rotation) and a radial (inflow) velocity component, producing gas spiraling inward on the disk plane. When the disk flips, the tangential and radial velocity components add together differently. This alters whether the radial inflow boosts or cancels the projected rotation velocity, resulting in different modeled LOS velocity ranges. We have explained the model in detail and demonstrated this asymmetry in the Appendix of Paper II.

In general, the asymmetry originates from velocity vectors added together differently when the disk flips. Through our simple radial inflow model, we will demonstrate the use of the disk tilt to constrain disk inflows. In Paper IV, we have also discussed how the disk tilt constrains outflow models and explains minor-axis absorption. Hence, the disk tilt is an important parameter when modeling circumgalactic gas kinematics.

In this paper, we will demonstrate a method to independently deduce the disk tilt, i.e., the sign of disk inclination, *a priori*; Figure 3.2 illustrates this concept. Because disks rotate differentially, and only trailing spirals are long-lived (Carlberg & Freedman 1985), spiral arms generally trail the direction of rotation. Hence, using the observed wrapping direction of spiral arms and the direction of disk rotation measured from the rotation curve, we can determine which way the disk tilts on the sky.

This work examines five galaxy–quasar pairs from Paper II and Paper IV. We present new, high-resolution images for the five galaxies, including optical images from the Hubble Space Telescope (HST) and adaptive-optics-corrected (AO-corrected), near infrared

images from the Keck Observatory. Section 4.5 briefly describes the imaging observations. Section 3.3 shows that these new images reveal the wrapping direction of the spiral arms for four galaxies. Together with the rotation curves (presented in Paper II), we determine how the disks tilt and examine whether/how the tilts constrain the radial inflow model in Paper II. Section 3.4 discusses the implications of our results, which we summarize in Section 3.5. Throughout the paper, we adopt the cosmology from Planck Collaboration et al. (2015), with  $h = 0.6774$ ,  $\Omega_m = 0.3089$ ,  $\Omega_\Lambda = 0.6911$ , and  $\Omega_b = 0.0486$ .



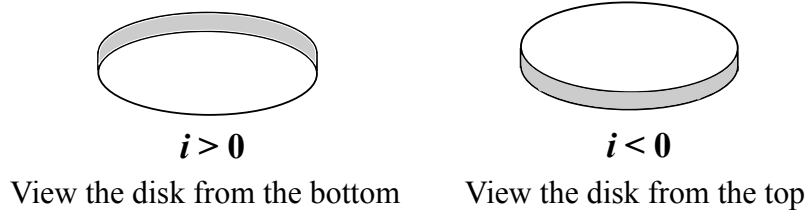


Figure 3.1: Sign of disk inclination. For a measured disk axis-ratio, the disk can tilt in two different ways with respect the plane of the sky. From the perspective of the observer, switching the sign of disk inclination flips the near side and the far side of the galaxy disk.

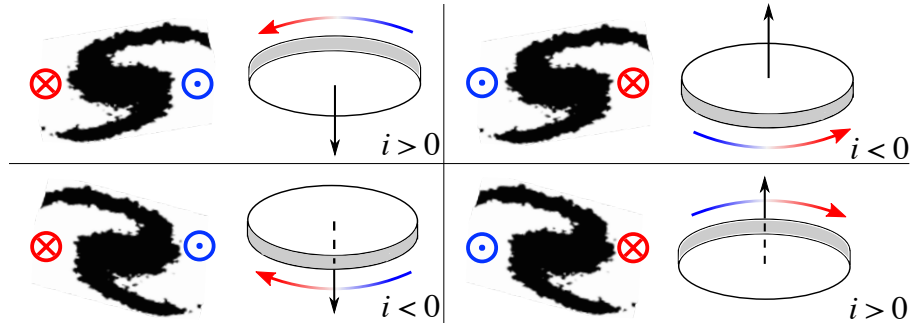


Figure 3.2: Deducing disk tilt from wrapping direction of spiral arms and measured galaxy disk rotation. On each schematic diagram of the spiral arms, the blue dot and the red cross represent the blueshifted and the redshifted sides of the measured disk rotation. The deduced disk tilt is shown on the right. The curved color arrow indicates the rotation direction of each disk, and the straight black arrow shows the corresponding angular momentum vector.

Table 3.1. Target Information and Summary of Spectroscopic Measurements

Quasar Name (1)	Galaxy Name (2)	$i$ ( $^{\circ}$ ) (3)	$\alpha$ ( $^{\circ}$ ) (4)	$z_{gal}$ (5)	$b$ (kpc) (6)	$R_g$ (kpc) (7)	$v_D^{Mg II}$ ( $\text{km s}^{-1}$ ) (8)	$\Delta v_{2796}$ ( $\text{km s}^{-1}$ ) (9)	$\Delta v_{2796}^{intr}$ ( $\text{km s}^{-1}$ ) (10)	$v_{rot}$ ( $\text{km s}^{-1}$ ) (11)
J091954+291408	J091954+291345	73	15	0.23288	88	115	$137 \pm 4$	$[-51, 292]$	$[7, 235]$	250 <sup>a</sup>
J102907+421752	J102907+421737	50	19	0.26238	65	69	$-154 \pm 9$	$[-266, -8]$	$[-208, -66]$	155
J123049+071036	J123049+071050	38	4	0.39946	98	98	$-53 \pm 15$	$[-134, 34]$	$[-76, -24]$	190
J124601+173156	J124601+173152	63	11	0.26897	19	20	$-91 \pm 34^b$	$[-172, -21]$	$[-115, -79]$	60
J142501+382100	J142459+382113	61	8	0.21295	83	85	$-299 \pm 11$	$[-404, -200]$	$[-314, -290]$	190
							$9 \pm 7$	$[-128, 221]$	$[-37, 130]$	

<sup>a</sup>We attribute this blue, weak absorption component to a red galaxy within the group. See Paper I or Section 3.2.3 for details.

<sup>b</sup>The absorption system falls in a part of the LRS spectrum without arcclamp lines. Extrapolation of the dispersion solution adds an additional error term of  $34 \text{ km s}^{-1}$  on top of the measurement error.

Note. — (1) Name of the quasar. (2) Name of the galaxy. (3) Inclination of the galactic disk. (4) Azimuthal angle, the angle between the galaxy major axis and the quasar sightline. (5) Galaxy systemic redshift measured from emission lines. (6) Sightline impact parameter. (7) Galactocentric radius. (8) Mg II Doppler shift measured from line profile fitting. (9) Measured velocity range. (10) Intrinsic velocity range (corrected for the line broadening effect due to the instrumental resolution). (11) Asymptotic galaxy rotation speed.

## 3.2 Data and Observations

We present new imaging observations of five galaxies from the galaxy–quasar pairs in Paper II and Paper IV. For these five  $z \approx 0.2$ , blue galaxies, Paper II and Paper IV detected Mg II absorption along the quasar sightlines and measured the galaxy rotation curves using the Low Resolution Imaging Spectrometer (LRIS; Oke et al. 1995; Rockosi et al. 2010) at Keck and the Double Imaging Spectrograph at the Apache Point Observatory 3.5m telescope.<sup>2</sup> Table 3.1 summarizes the key spectroscopic measurements of the five systems. This paper presents new optical images from HST Wide Field Camera 3 (WFC3) and/or AO-corrected, near infrared images from the Keck NIRC2 camera of the galaxies. These high resolution images reveal galaxy structural features that cannot be recognized in the SDSS images, e.g., the wrapping of spiral arms, the presence of companion galaxies, etc. Table 3.2 lists the imaging observations of the galaxies. We describe the HST WFC3 and Keck NIRC2 observations in Section 3.2.1 and 3.2.2, respectively. Section 3.2.3 briefly describes the environment of the galaxies.

---

<sup>2</sup> Instrument specifications can be found in the manual written by Robert Lupton, which is available at [http://www.apo.nmsu.edu/35m\\_operations/35m\\_manual/Instruments/DIS/DIS\\_usage.html#Lupton\\_Manual](http://www.apo.nmsu.edu/35m_operations/35m_manual/Instruments/DIS/DIS_usage.html#Lupton_Manual)

Table 3.2: Imaging Observations

Target Galaxy	Instrument	Exposure Time (s)	Filter	Field-of-view ( $''$ )	Plate Scale ( $''$ pixel $^{-1}$ )	PSF FWHM <sup>a</sup> ( $''$ )	Observing Dates
J091954+291345	Keck/NIRC2	600	$K_s$	$40'' \times 40''$	0.039686	0.20	2017 Jan 28
J102907+421737	HST/WFC3 UVIS	1716	F390W	$162'' \times 162''^a$	0.04	0.07	2017 Jan 25
	HST/WFC3 UVIS	700	F814W	$162'' \times 162''^a$	0.04	0.07	2017 Jan 25
	Keck/NIRC2	600	$K_s$	$40'' \times 40''$	0.039686	0.15	2017 Jan 26
J123049+071050	Keck/NIRC2	600	$K_s$	$40'' \times 40''$	0.04	0.12	2015 May 6
J124601+173152	HST/WFC3 UVIS	1629	F390W	$162'' \times 162''^a$	0.04	0.07	2017 Jan 28
	HST/WFC3 UVIS	700	F814W	$162'' \times 162''^a$	0.04	0.07	2017 Jan 28
	Keck/NIRC2	600	$K_s$	$40'' \times 40''$	0.039686	0.23	2017 Jan 26
	Keck/NIRC2	1200	$K_s$	$40'' \times 40''$	0.039686	0.31	2017 Apr 13
J142459+382113	HST/WFC3 UVIS	1674	F390W	$162'' \times 162''^a$	0.04	0.07	2017 Jun 5
	HST/WFC3 UVIS	700	F814W	$162'' \times 162''^a$	0.04	0.07	2017 Jun 5
	Keck/NIRC2	600	$K_s$	$40'' \times 40''$	0.039686	0.14	2015 May 6

<sup>a</sup> The full-width-half-maximum (FWHM) of the point spread function (PSF).

<sup>b</sup> The WFC3/UVIS channel has a rhomboidal field-of-view.

### 3.2.1 HST WFC3 Observations

We imaged three galaxies using the WFC3/UVIS channel and the F390W and F814W broadband filters (Cycle 24, PID: 14754, PI: C. L. Martin). We list the exposure time for each galaxy in Table 3.2. The table also includes the field-of-view, the plate scale, and the full-width-half-maximum (FWHM) of the point spread function (PSF) of the UVIS channel.

Individual data frames were retrieved from MAST<sup>3</sup>. These data frames were already reduced and calibrated by the standard WFC3 calibration pipeline `calwf3`.<sup>4</sup> For the F390W data frames, we drizzled the three dithered images of each target using `DrizzlePac` (Fruchter et al. 2010).<sup>5</sup> But for the F814W data frames, because we only took two exposures per target, cosmic ray removal during drizzling was sub-optimal. Therefore, we used L.A.Cosmic (van Dokkum 2001) to remove the cosmic rays from individual F814W frames. Then we drizzled the cleaned frames to produce the science images for individual targets.

### 3.2.2 Keck NIRC2 Observations

We observed all five galaxies with the NIRC2 camera on the Keck II telescope, using the paired quasar as the tip-tilt reference for the Keck laser guide star adaptive optics system (LGSAO; van Dam et al. 2006; Wizinowich et al. 2006). Paper IV described the

---

<sup>3</sup><http://archive.stsci.edu>

<sup>4</sup> Documentation of `calcf3` can be found at Gennaro, M., et al. 2018, WFC3 Data Handbook, Version 4.0, (Baltimore: STScI).

<sup>5</sup> Documentation of `DrizzlePac` can be found at Gonzaga & et al. (2012).

observation and the data reduction in detail. In brief, we observed each galaxy using the  $K_s$  broadband filter, which centered at  $2.146 \mu\text{m}$ ; Table 3.2 lists the  $K_s$  observation. We reduced the images using the data reduction pipeline provided by the UCLA/Galactic center group (Ghez et al. 2008). The final images were dark corrected, flat-fielded, sky subtracted, and corrected for geometrical distortion.

### 3.2.3 Galaxy Environment

Galaxy group environment affects the properties of Mg II absorption, such as the absorption strength and velocity dispersion (Bordoloi et al. 2011; Johnson et al. 2015; Nielsen et al. 2018), and possibly leads to uncertain host galaxy assignment of the Mg II absorption. We have flagged three of the five target galaxies as potential group members (Paper II; Paper IV).

J124601+173152 is in a rich environment, with three brighter galaxies having consistent photometric redshifts. While our target galaxy is the closest to the quasar sightline, both Paper II and Paper IV flagged this system because the host identification for the Mg II absorption may not be unique.

Because we lack spectroscopic redshifts for all but the closest galaxies in our fields, we cannot classify the environment of the absorbers as Chen & Mulchaey (2009) and Johnson et al. (2013) did. Nevertheless, we searched for potential group members using the SDSS images and photometric redshifts of the galaxies in each field, and we found two other target galaxies potentially in groups. We found there is a potential group

member near galaxy J102907+421737, but the association of Mg II absorption in the J102907+421752 sightline with the target galaxy J102907+421737 is secure, because our target galaxy is three times closer to the sightline than the other bright galaxy in the field. Secondly, around galaxy J091954+291345, two red galaxies at  $4''.4$  and  $8''.7$  away have photometric redshifts consistent with our target; these three galaxies likely form a group. The spectrum of our paired quasar detects two absorption systems. Following Paper II and Paper IV, we assign the stronger system to the blue galaxy (our target), and we consider the weaker system as potentially not produced by our target.

### **3.3 Individual Galaxies: Disk tilt and Gas Kinematic Modeling**

The new, high-resolution images reveal the spiral structures for four of the five galaxies. We deduce how these disks tilt, and then we explore how their tilts constrain the gas kinematic modeling, which aims to explain the broad Mg II velocity range measured. Section 3.3.1 shows the new images and discusses the image processing steps. Section 3.3.2 reviews the key components of the radial inflow model from Paper II. Then in Section 3.3.3, we discuss individual galaxies regarding how each disk tilts, and we explore how it combines with the inflow model in Paper II and affects the modeled inflow properties.

### 3.3.1 Deducing the Disk Tilt From High-Resolution Images

Figure 3.3 shows the images of individual galaxies and the deduced 3D disk orientations. We rotate the galaxy images such that each galaxy major axis aligns with the image x-axis, and the quasar sightline lies in the positive x-direction. Each schematic diagram in the last column illustrates the wrapping direction of spiral arms and direction of the disk rotation (curved, blue/red arrow). Following the concept illustrated by Figure 3.2, we deduce the sign of the disk inclination, i.e, which way the disk tilts.

Contrasting our high-resolution images with the color images from the Sloan Digital Sky Survey (SDSS) in Figure 3.3 highlights the resolving power of our new images. For the SDSS images, the median full-width-half-maximum (FWHM) of the point spread function (PSF) in the  $r$ -band is  $1''.3$ . This is an order of magnitude higher than that for both WFC3 optical and the NIRC2  $K_s$  images. Therefore, these images accentuate the capability of the high-resolution imaging to reveal structures and companion galaxies that low-resolution imaging fails to resolve.

When the spiral arms are not prominent in the high-resolution images, we apply additional image processing steps to visually enhance the structural features. We create three-color images for J102907+421737, J124601+173152, and J142459+382113, all of which are observed in F390W, F814W, and  $K_s$  bands. We use blue, green, and red colors to represent the three bands respectively.<sup>6</sup> The color images also allow us to visualize the spatial distribution of different stellar populations. In addition, the F390W image of

---

<sup>6</sup> We register the images before creating the color images. We resample the pixels to the pixel scale of the WFC3 images and align all images using reference point sources in the common field.



J102907+421737 and the  $K_s$  image of J123049+071050 only show weak traces of spiral arms. So, we process the images as follows to enhance the spiral features. First, we use GALFIT (Peng et al. 2002) to model the smooth galaxy emission component with an exponential disk surface brightness (SB) profile and convolve the model with the instrumental PSF. We model the instrumental PSF of the HST WFC3 using Tiny Tim (Krist et al. 2011), and for the  $K_s$  image, we fit a Moffat profile to our paired quasar. The residual image, i.e., the difference between the original image and the convolved galaxy SB model, shows traces of spiral arms. Then, we apply a median filter to the residual and add it to the original F390W or  $K_s$  images. For J102907+421737, we use the enhanced F390W image to create the three-color image. We present the processed images under the “Processed/Color Image” column in Figure 3.3.

### 3.3.2 Brief Description of the Disk Model and Radial Inflow

The simple inflow model in Paper II combines the tangential (rotational) and radial (inflow) velocity components on the disk plane. We model the rotation component as

$$\mathbf{v}_\phi(z) = v_{\text{rot}} \exp(-|z|/h_v) \hat{\phi} , \quad (3.1)$$

where  $v_{\text{rot}}$  represents the asymptotic galaxy rotation speed measured, and the velocity scale height  $h_v$  introduces a vertical velocity gradient to create a rotational lag above and below the disk midplane. Paper II discussed two cases: (1)  $h_v \rightarrow \infty$ , i.e., without a velocity gradient, and (2) a fiducial  $h_v$  value of 10 kpc, which produced vertical velocity gradients of 11 to 26 km s<sup>-1</sup> per kpc for the galaxy sample. Because the fiducial 10 kpc

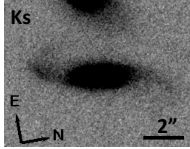
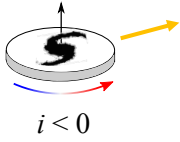
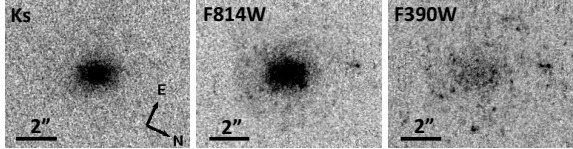
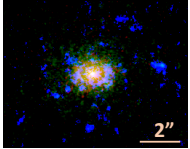
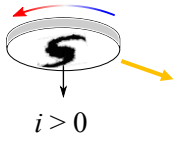
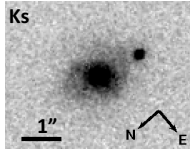
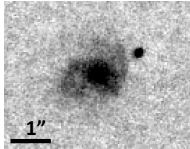
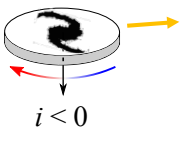
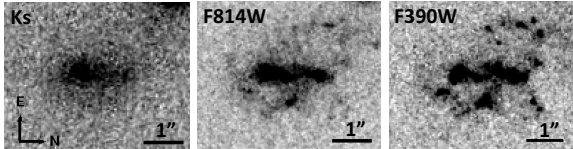
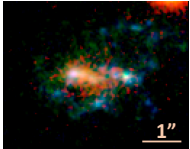
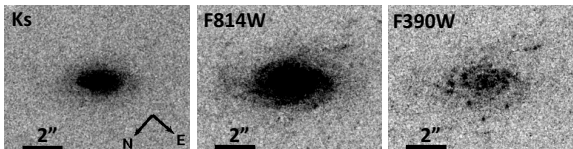
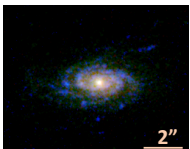
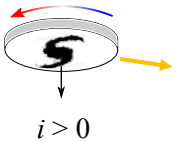
SDSS Color Image	High-resolution Image(s) Ks/F814W/F390W (if observed)	Processed/Color Image	3D Disk Orientation
<b>J091954+291345</b>		See spiral arms in the Ks image.	 $i < 0$
<b>J102907+421737</b>			 $i > 0$
<b>J123049+071050</b>			 $i < 0$
<b>J124601+173152</b>			Not Axisymmetric
<b>J142459+382113</b>			 $i > 0$

Figure 3.3: High-resolution galaxy images and the deduced 3D disk orientations. Each row (separated by the thick black line) corresponds to one galaxy. Column 1 demonstrates that the low-resolution SDSS images cannot resolve the galaxy structural features. Column 2 shows the high-resolution NIRC2  $K_s$ , WFC3 F814W, and WFC3 F390W (if observed) for individual galaxies. For galaxies with spiral arms or structures that can hardly be distinguished in the original images, column 3 shows the processed images that visually enhanced the structural features. In particular, column 3 shows the three-color images for galaxies observed in all three bands. Column 4 illustrates the wrapping direction of the spiral arms, the measured disk rotation (the curved arrow), and the deduced 3D disk orientation. Each orange arrow points toward the direction of the quasar sightline. The images for individual galaxy have the same scale and the same orientation; each galaxy major axis aligns with the image x-axis, and the quasar sightline lies in the positive x-direction.

value creates velocity gradients consistent with measurements of extraplanar gas, which extends to about 10 kpc vertically and over 20 kpc radially of nearby galaxies (Benjamin 2002; Oosterloo et al. 2007; Marasco & Fraternali 2011; Zschaechner et al. 2011, 2012; Gentile et al. 2013; Kamphuis et al. 2013), here, we follow Paper II and adopt the same fiducial  $h_v$  value when we consider disks with lagging rotation. As for the radial inflow component, we adopt a constant radial velocity,

$$\mathbf{v}_R(R, z) = v_R \hat{\mathbf{R}} , \quad (3.2)$$

where  $v_R < 0$  for inflow.

We obtain the LOS velocity  $v_{\text{los}}$  by taking the dot product between each of Equations (A.2) and (A.10) with the vector describing the quasar sightline. The impact parameter  $b$  and azimuthal angle  $\alpha$  set the orientation of the sightline with respect to the galaxy disk. The disk inclination  $i$  and the modeled thickness  $H_{\text{eff}}$  (measured from the disk midplane) limit the pathlength along the sightline that intersects the disk. Along this sightline path, the bluest and the reddest ends of the  $v_{\text{los}}$  define the resultant LOS velocity range.

### 3.3.3 Disk Tilt of Individual Galaxies and their Gas Kinematic Modeling

Using new individual galaxy images and the measured galaxy rotation curves (presented in Paper II), we determine which way the disk tilts. Then, we investigate whether and/or how the deduced disk tilt constrain the gas kinematic modeling and the inflow properties.

Specifically, we explore whether the rotating disk model, without and with radial inflow, can reproduce the broad Mg II LOS velocity range measured along the quasar sightlines.

For individual galaxies, we show position–velocity (PV) diagrams, i.e.,  $D_{\text{los}}$  vs.  $v_{\text{los}}$ , for the rotating-disk-only model (no radial inflow) and models with radial inflow for disks at  $i > 0$  and  $i < 0$ . Contrasting the two tilts demonstrates how the *a priori* knowledge of the disk tilt affects the modeling. In each PV diagram,  $D_{\text{los}} = 0$  represents the disk midplane, and  $D_{\text{los}} < 0$  ( $> 0$ ) represents the sightline at the near (far) side of the disk. The cyan shaded region represents the measured LOS velocity range of the Mg II absorption. The cyan hashes indicate the uncertainties of the measured velocity range at the blue and red ends. The gray shaded region that enclosed the modeled  $v_{\text{los}}$  (black curve) shows the line broadening effect that matches the LRIS spectral resolution. The modeled LOS velocity range (gray shaded region) agrees with the measurement only if both the bluest and reddest end of the modeled  $v_{\text{los}}$  fall within the uncertainties of the two ends of the measurement (cyan hashes). To illustrate the known problem that thin disks cannot explain broad velocity ranges, the two yellow markers in the PV diagram (left) indicate where the sightline intersects the boundary of an  $H_{\text{eff}} = 1$  kpc disk. Along the short sightline path that intersects the thin disk, because of the small variation in the LOS velocity, a thin disk can only produce a narrow velocity range.

### 3.3.3.1 J091954+291345

The galaxy J091954+291345 clearly shows the spiral arms in the  $K_s$  image. Together with the direction of disk rotation determined from the rotation curve, we deduce that the disk has a negative inclination.

To reproduce the measured LOS velocity range spanning over  $300 \text{ km s}^{-1}$  (Figure 3.4), a rotating disk without a vertical velocity gradient requires a 500-kpc thick “disk” ( $H_{\text{eff}} = 250 \text{ kpc}$ ). Alternatively, a rotating disk with a vertical velocity gradient reproduces the velocity range with a significantly thinner disk of  $H_{\text{eff}} = 15 \text{ kpc}$  ( $h_v = 10 \text{ kpc}$ , left panel);  $H_{\text{eff}}$  below 15 kpc cannot produce blue enough absorption to match the measurement. Furthermore, adding radial inflow to this  $H_{\text{eff}} = 15 \text{ kpc}$  disk can also reproduce the absorption. The negatively inclined disk allows radial inflow of at most  $30 \text{ km s}^{-1}$ ; a higher inflow speed causes the absorption not being red enough at the disk midplane (right panel).  $H_{\text{eff}}$  cannot be further reduced, otherwise the disk cannot produce blue enough absorption. If the disk were positively inclined, then the inflow speed could reach  $140 \text{ km s}^{-1}$  before the absorption becomes too red at the disk midplane, but the disk would need an  $H_{\text{eff}}$  of 25 kpc to match the blue absorption end (middle panel). Because the two disk tilts permit significantly different radial inflow scenarios, the deduced negative disk inclination tightens the constraint on the radial inflow speed to at most  $30 \text{ km s}^{-1}$ .

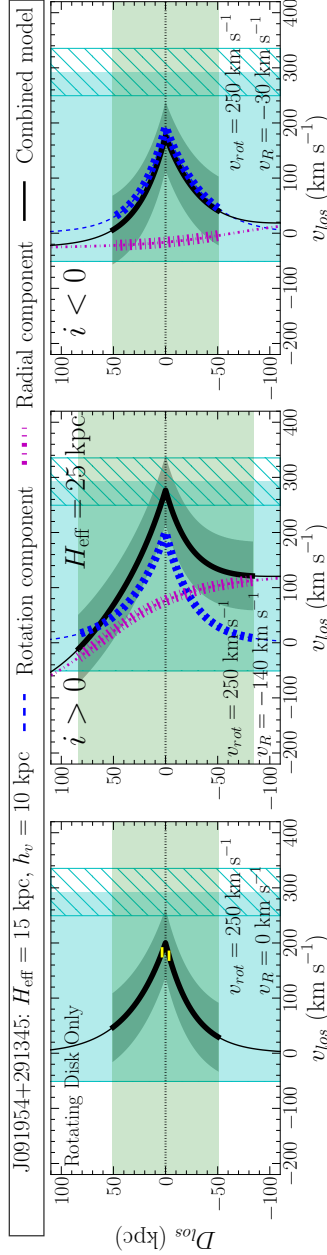


Figure 3.4: J091954+291345: Disk tilt helps tighten constraint on radial inflow speed. The galaxy disk is negatively inclined (the schematic diagram and Section 3.3.3.1). A rotating disk of  $H_{\text{eff}} = 15$  kpc and  $h_v = 10$  kpc marginally reproduces the LOS velocity range of the absorption (left), and a thinner disk cannot reproduce the blue absorption end. For example, the pathlength within an  $H_{\text{eff}} = 1$  kpc disk is short, producing only a narrow velocity range (yellow markers). Disks with positive (middle) and negative (right) inclinations allow maximum radial inflow speeds of  $140 \text{ km s}^{-1}$  and  $30 \text{ km s}^{-1}$  respectively. Otherwise, the absorption becomes too red or not red enough at the disk midplane. Hence, deducing the disk as negatively inclined limits the inflow speed to  $30 \text{ km s}^{-1}$ . Except for the middle panel with  $H_{\text{eff}} = 25$  kpc, the disks in the left and the right panels show  $H_{\text{eff}} = 15$  kpc. See the text for details.

### 3.3.3.2 J102907+421737

For J102907+421737, the F390W image shows the spiral arms most clearly, and we visually enhance the spiral features and create the color image as described in Section 3.3.1. The color image also shows that the outer disk is bluer than the inner disk. This suggests that the outer disk is younger and less metal-rich than the inner disk (de Jong 1996; Bell & de Jong 2000; MacArthur et al. 2004), indicating an inside-out disk growth. From the revealed wrapping direction of the spiral arms and the measured disk rotation, we deduce that the disk has a positive inclination.

A disk without a velocity gradient can explain the  $\sim 100 \text{ km s}^{-1}$  measured LOS velocity range. However, the disk would need an  $H_{\text{eff}}$  of 65 kpc to bring the absorption close to the galaxy systemic velocity in order to match the red absorption end. With  $h_v = 10 \text{ kpc}$ , a thinner rotating disk of  $H_{\text{eff}} = 10 \text{ kpc}$  can reproduce the LOS velocity range of the absorption within measurement uncertainties (left panel of Figure 3.5). Further reducing the disk thickness would make the absorption not red enough to match with the measurement. If we also consider radial inflow on the  $H_{\text{eff}} = 10 \text{ kpc}$  disk, then the inflow speed for a positively (negatively) inclined disk cannot exceed 40 (80)  $\text{km s}^{-1}$ . Otherwise, the absorption becomes too blue (not blue enough) at the disk midplane; see the middle (right) panel. Hence, the inferred positive disk inclination limits the radial inflow speed to at most  $40 \text{ km s}^{-1}$ .

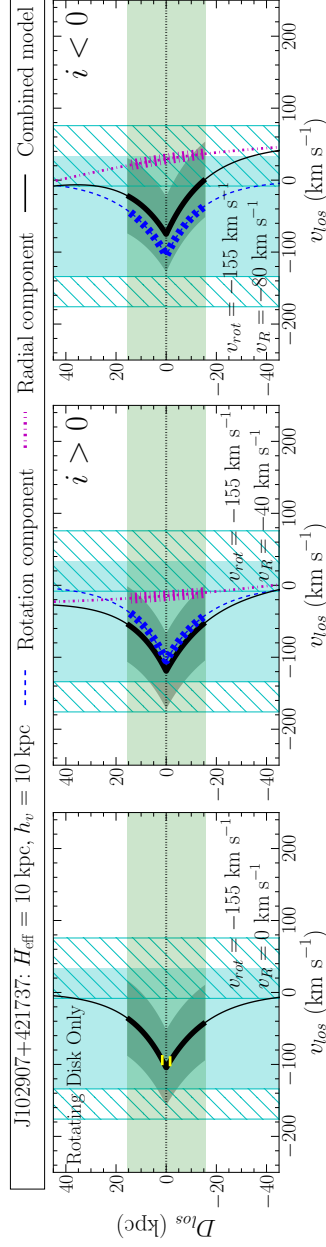


Figure 3.5: J102907+421737: Disk tilt helps tighten constraint on radial inflow speed. The galaxy has a positively inclined disk (the schematic diagram and Section 3.3.3.2). A rotating disk with  $H_{\text{eff}} = 10$  kpc can reproduce the observed LOS velocity range within measurement uncertainties. A sightline that intersects a thinner disk, e.g., an  $H_{\text{eff}} = 1$  kpc disk (yellow markers), cannot produce a broad enough velocity range. Disks with positive (middle) and negative (right) inclinations allow maximum radial inflow speeds of  $40 \text{ km s}^{-1}$  and  $80 \text{ km s}^{-1}$  respectively. Otherwise, the absorption becomes too blue or not blue enough at the disk midplane. With the inferred disk inclination being positive, the radial inflow speed cannot exceed  $40 \text{ km s}^{-1}$ .



### 3.3.3.3 J123049+071050

The high-resolution  $K_s$  image resolves the target “galaxy” into two objects: a galaxy with spiral arms and a possible satellite. The galaxy also has weak traces of spiral arms, and we visually enhance the arms as described in Section 3.3.1. From the wrapping direction of the spiral arms and the direction of disk rotation, we deduce that the disk has a negative inclination.

A rotating disk without a vertical velocity gradient can reproduce the  $160 \text{ km s}^{-1}$  measured velocity range, but the “disk” has to be 260-kpc thick ( $H_{\text{eff}} = 130 \text{ kpc}$ ) to bring the red absorption end close to the galaxy systemic velocity. In contrast, the fiducial model with a vertical velocity gradient only requires a 10-kpc thick disk ( $H_{\text{eff}} = 5 \text{ kpc}$ ) to reproduce the velocity range spanned by the absorption. But even with radial inflow, either tilt produces LOS velocity range that varies insignificantly with the inflow speed. Even as the inflow speed increases from zero to  $300 \text{ km s}^{-1}$ , the LOS velocities at both the bluest and the reddest ends change by no more than  $20 \text{ km s}^{-1}$ . This  $20 \text{ km s}^{-1}$  shift is allowed by the measurement uncertainties. This means that regardless of which way the disk tilts, an inflow speed as large as  $300 \text{ km s}^{-1}$  can always explain the measured velocity range. Hence, knowing the disk tilt *a priori* cannot tighten the constraint on the radial inflow speed. The reason of why the LOS velocity is insensitive to both the radial inflow speed and the disk tilt is because of the low disk inclination ( $i = 38^\circ$ ) and small azimuthal angle ( $\alpha = 4^\circ$ ). Section 3.4 discusses how both factors affect the effectiveness of constraining the radial radial speed.

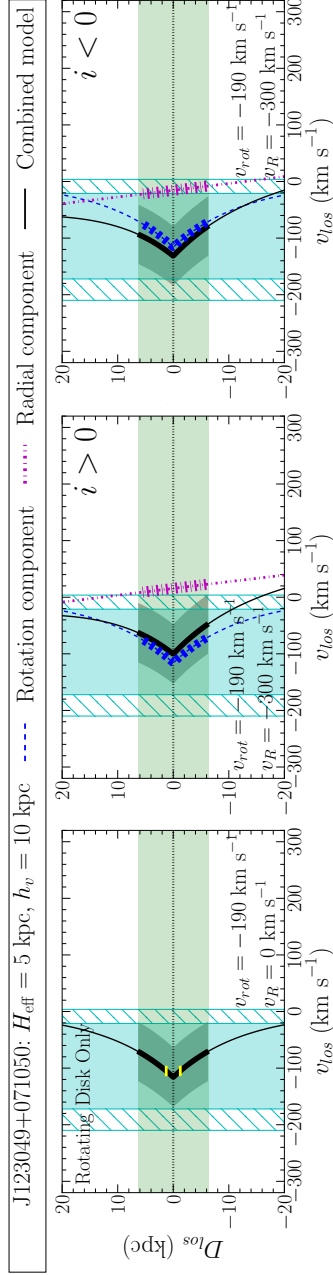


Figure 3.6: J123049+071050: Disk tilt cannot tighten constraint on radial inflow speed. We deduce the disk as being negatively inclined (the schematic diagram and Section 3.3.3.3). A rotating disk (left) of  $H_{eff} = 5$  kpc and  $h_v = 10$  kpc can explain the velocity range of the absorption, and a thinner disk cannot create broad enough absorption with the red absorption end close to the galaxy systemic velocity. Alternatively, regardless of which way the disk tilts, a radial inflow of  $300 \text{ km s}^{-1}$  changes the velocities at both the blue and the red ends by no more than  $20 \text{ km s}^{-1}$  (middle and right). Both tilts can still reproduce the measured LOS velocity range within measurement uncertainties. Hence, knowing the disk tilt *a priori* cannot tighten the constraint on the radial inflow speed.

#### 3.3.3.4 J124601+173152

Both F390W and F814W images of J124601+173152 reveal that the galaxy has an irregular, clumpy structure. In both F390W and F814W images, the galaxy shows two bright clumps along the N-S direction. However, the  $K_s$  image only detects a single nucleus that lies at the location of the southern clump. The color image also shows that the emission in  $K_s$  overlaps with the southern clump only.

Altogether, our images suggest that this galaxy has a complicated, clumpy structure instead of a typical, axisymmetric disk morphology. Hence, we do not define how this galaxy “disk” tilts, and we do not create disk models to explain the Mg II absorption.

#### 3.3.3.5 J142459+382113

Both F390W and F814W images of J142459+382113 unambiguously detect the spiral arms. From the wrapping direction of the arms and the measured disk rotation, we deduce the disk as being positively inclined.

Moreover, the color image clearly shows that the outer disk is bluer than the inner disk. The presence of the color gradient is also supported by the larger disk scalelengths measured at the bluer bands. The color gradient indicates that the outer disk has a younger stellar population and a lower metallicity than the inner disk, suggesting the disk grows inside-out. In Section 3.4, we will discuss the implications of this disk growing inside-out together with the result from our inflow modeling.

The Mg II absorption detected in the quasar sightline has a small Doppler shift. Since

the broad velocity range spans both sides of the galaxy systemic velocity, neither the line broadening by instrumental resolution nor any structure with only rotation can explain the two-sided absorption. A rotating disk also produces bluer absorption than measured near the disk midplane. The left panel of Figure 3.7 illustrates this problem using a disk with a vertical velocity gradient. A disk without a velocity gradient makes the problem worse, because the absence of the gradient makes the projected rotation velocity peak at a higher velocity (i.e., bluer) along the LOS. Therefore, while the radial inflow model can produce two-sided absorption that a rotation-only structure fails to produce, solving the problem of excess blue absorption from the disk rotation requires the LOS velocities from the inflow and the rotation components to have opposite signs near the midplane.

Only a negatively inclined disk can achieve this configuration. The right panel of Figure 3.7 illustrates that the radial inflow (rotation) component creates a positive (negative) LOS velocity near the disk midplane, and reproducing the measured velocity range requires an  $H_{\text{eff}} = 10$  kpc disk with an exceptionally high radial inflow speed of  $480 \text{ km s}^{-1}$ . The problem is that we deduce the disk as being positively inclined. Radial inflow makes the absorption even bluer than disk rotation alone, because both velocity components have the same Doppler sign near the midplane. The middle panel illustrates this problem using a fiducial inflow speed of  $100 \text{ km s}^{-1}$ . Therefore, for this galaxy, its positively inclined disk excludes the detection of radial inflow in the sightline.

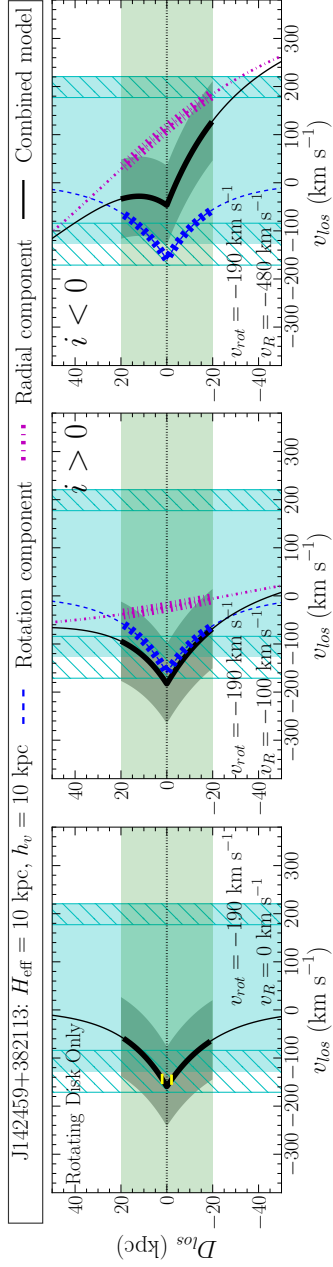


Figure 3.7: J142459+382113: Disk tilt excludes radial inflow detection. The disk is positively inclined (the schematic diagram and Section 3.3.3.5). Regardless of the thickness of the disk, disk rotation alone (left) cannot reproduce the broad absorption that spans both sides of the galaxy systemic velocity, and the rotation produces bluer absorption near the disk midplane than measured. Only a negatively inclined disk (right) can reproduce the LOS velocity range. However, the disk is positively inclined. Introducing radial inflow produces even bluer net absorption (middle) than a rotating disk (left) near the midplane. We demonstrate this problem using a fiducial inflow speed of  $100 \text{ km s}^{-1}$ . Hence, the positively inclined disk of this galaxy excludes the detection of radial inflow in the sightline.

## 3.4 Discussion and Implications

Which way a galaxy disk tilts on the sky can be deduced from the wrapping direction of the spiral arms and the direction of disk rotation (Figures 3.2 and 3.3). Using a radial inflow model with gas spiraling inward on the disk plane (as described in Paper II), the four examples in Section 3.3 have demonstrated incorporating the disk tilt as an extra parameter in modeling the circumgalactic gas kinematics. With *a priori* knowledge on the disk tilt, our examples show that we can constrain the radial inflow speed for a galaxy or even exclude radial inflow.

### 3.4.1 The Projection of Radial Inflow is Not Symmetric About a Disk Flip

In the radial inflow model, which way the disk tilts alters the projected LOS velocity from an individual velocity component and results in different LOS velocity ranges. The key to this asymmetry is the location where the sightline intersects the disk tangentially.<sup>7</sup> At this tangent point, the sightline is normal to the radial velocity vector, producing zero LOS velocity. If the disk rotation does not have a vertical velocity gradient, then this tangent point also produces the maximum rotational velocity projection of  $v_{\text{rot}} \sin |i|$ .

When the disk flips, the tangent point switches from one side to the other side of the

---

<sup>7</sup> The sightline intersects the disk tangentially only at the point where the disk radius equals to the sightline impact parameter  $b$ . In general, at different  $D_{\text{los}}$ , the sightline intersects the disk at different disk radii larger than  $b$ .

disk.<sup>8</sup> This affects whether or not the LOS velocities of the rotation and the inflow components have the same sign near the disk midplane, which determines whether the radial inflow boosts or cancels the projected rotation velocity. Consequently, flipping the disk alters the resultant LOS velocity produced by the two velocity components.

J142459+382113 most clearly demonstrates how this property affects the modeling. As explained in Section 3.3.3.5, the radial inflow has to cancel the excess blue absorption produced by the disk rotation. To achieve this configuration, this galaxy disk must have a negative inclination; the tangent point is at the far side of the disk ( $D_{\text{los}} > 0$ ), so that near the disk midplane, the rotation and radial inflow components produce blue and red Doppler velocities, respectively. However, the disk is positively inclined, and hence, this rules out the radial inflow detection in this sightline.

### 3.4.2 Constraining Radial Inflow Speed or Predicting the Disk Tilt

When we use the model to explain the measured LOS velocity range, the observationally deduced disk tilt allows us to constrain the maximum radial inflow speed or exclude radial inflow detection. For example, the observed disk tilt of J091954+291345 (Figure 3.4) and J102907+421737 (Figure 3.5) constrains the inflow speeds to 30-40 km s<sup>-1</sup>, instead of  $\approx 100$  km s<sup>-1</sup> allowed by the opposite tilt. We also exclude radial inflow detection for J142459+382113 (Figure 3.7), because its disk tilts in a direction opposite to that

---

<sup>8</sup> Whether the tangent point is at the near side or the far side of the disk does not only depend on which way the disk tilts, but also depend on the position of the quasar sightline with respect to the galaxy disk.

allowed by the model. Therefore, in principle, we can use the sign of disk inclination as an extra geometrical parameter while modeling the Mg II velocity range along the LOS, and hence, the asymmetry between the disk tilt and LOS velocity measurements helps model the circumgalactic gas kinematics.

However, our example of J123049+071050 has revealed a caveat: not all resultant LOS velocity ranges are sensitive to the radial inflow speed and/or change significantly when we flip the disk (Figure 3.6). In fact, this example has demonstrated that both the galaxy disk inclination  $i$  and the azimuthal angle  $\alpha$  of the quasar sightline affect whether or not the disk tilt can constrain the radial inflow speed. We consider these two factors separately as follows.

First, since both the rotation and radial inflow velocity vectors lie on the disk plane, a less inclined disk produces a smaller LOS velocity projection. For example, for a face-on ( $i = 0^\circ$ ) disk, because both the tangential (rotation) and radial (inflow) velocity vectors are perpendicular to the sightline, we always detect zero velocity along the LOS. Therefore, due to the projection effect, the LOS velocity and the velocity range of a low-inclination disk are insensitive to the change in the radial inflow speed.

Second, when the  $\alpha$  is small, two disks of the same inclination  $|i|$  but with opposite tilts produce similar projected LOS velocity from the radial component. The projected radial velocity switches sign where the sightline intersects the disk tangentially, and this tangent point switches sides when the disk flips (Section 3.4.1). But for an  $\alpha = 0^\circ$  sightline, the tangent point is on the disk midplane, hence flipping the disk does not



change the projected radial velocity along the LOS. As  $\alpha$  increases, the tangent point moves away from the disk midplane. Flipping the disk then changes how the projected radial velocity varies along the LOS, resulting in different resultant LOS velocities and velocity ranges when we combine the radial and rotation velocity components.

In short, a less inclined disk makes the LOS velocity insensitive to the change in the radial inflow speed, and a small azimuthal angle leads to a small difference in the resultant projected LOS velocity between the two disk tilts. Consequently, to use the disk tilt to tighten the constraint on the radial inflow speed, we should avoid configurations that produce the tangent point on or near the disk midplane. Hence, inclined disks should be used, and  $\alpha \approx 0^\circ$  sightlines should be avoided.

Since we have observationally deduced how the disk tilts for our galaxies, we use the asymmetry between the tilt and the LOS velocity range to constrain the inflow speed or reject the detection of radial inflow. But even if the disk tilt is not measured *a priori*, we can use the asymmetry to make a testable prediction on which way the disk tilts if only one of them can reproduce the measured LOS velocity range. For example, the radial inflow modeling for J142459+382113 would predict a negative disk inclination. But because we deduce a positive inclination from the rotation curve and the wrapping direction of the spiral arms, we can then conclude that the sightline does not detect radial inflow on the disk plane.

### 3.4.3 Radial Inflow Detection and Inside-out Disk Growth

A galaxy disk with a bluer outer disk but a redder inner disk indicates that the outer disk has a younger stellar population and a lower metallicity (de Jong 1996; Bell & de Jong 2000; MacArthur et al. 2004). While dust can contribute to the color gradient, it is unlikely that the gradient, especially at the outer disk, is largely due to dust extinction (Section 5 of MacArthur et al. 2004). Hence, a bluer outer disk suggests that the disk grows inside-out. For J142459+382113 and J102907+421737, we have obtained images in all F390W, F814W, and  $K_s$  bands, and the color images (Figure 3.3) show the presence of the color gradients. Hence, both disks need a gas supply to grow the disks and fuel the star formation in the outer disks.

However, for J142459+382113, neither a rotating disk nor the radial inflow model can explain the broad velocity range spanned by the Mg II absorption. This suggests that the sightline does not detect radial inflow near the disk plane. A disk growing inside-out but without radial inflow detected may seem contradictory. However, inflow may not need to be axisymmetric, such as the infalling gas streams seen in simulations (e.g., Nelson et al. 2013; Stewart et al. 2017). Our sightline may simply miss the inflow: both observations and simulations suggest that inflows have a small covering factor. Down-the-barrel spectral observations only identify inflows in a few percent of galaxies (Martin et al. 2012; Rubin et al. 2012), a result consistent with inflow covering a small solid angle, and thereby agrees with simulations that predict a small covering factor for cold accretion streams (e.g., Faucher-Giguère & Kereš 2011; van de Voort & Schaye 2012). Therefore,

whether or not we detect radial inflow near the disk plane does not imply the presence or absence of a disk color gradient or inside-out disk growth. Instead, our result possibly informs us about the spatial geometry of the inflowing gas.

On the other hand, for J102907+421737, we have constrained the maximum radial inflow speeds as  $40 \text{ km s}^{-1}$ ; hence, the inflow possibly feeds the growing disk. We are also able to constrain the radial inflow speeds for another galaxy, J091954+291345, as  $30 \text{ km s}^{-1}$ . A  $30\text{-}40 \text{ km s}^{-1}$  radial inflow speed is consistent with inflow gas measurements and models of the Milky Way and nearby galaxies. For example, Complex C falls towards the Galactic plane at  $50\text{-}100 \text{ km s}^{-1}$  (Wakker et al. 1999), and the extraplanar H I gas in the Milky Way has shown evidence of infall motion at  $20\text{-}30 \text{ km s}^{-1}$  (Marasco & Fraternali 2011). As for nearby galaxies, the H I gas of NGC 2403 moves radially inward at  $10\text{-}20 \text{ km s}^{-1}$  (Fraternali et al. 2002), and the Si IV absorbing gas in M33 has a modeled vertical accretion speed of  $110 \text{ km s}^{-1}$  at the disk-halo interface (Zheng et al. 2017). In our model, we have only considered infall in the radial direction on the disk plane but not infall perpendicular to the disk plane. Since our sightlines have impact parameters of tens of kpc instead of a few kpc as in Zheng et al. (2017), it becomes unphysical if the gas falls towards the extended disk plane at large radii but not towards the central region of the galaxy, where the gravitational potential is the lowest. And because of the corotation between the Mg II gas and the disk rotation (Paper II and Paper IV) and the formation of extended gas disks in simulations (see Section 4.1), we have modeled radial inflow in the disk plane instead of spherical inflow. We emphasize, however, that although the

gas kinematics require the CGM to have a component of angular momentum aligned with that of the disk, they do not directly constrain the location of the absorbing gas along the LOS. Radial inflow in the disk plane is consistent with these constraints, but other solutions may be possible, e.g., satellites accreting onto the galaxy, series of gas clouds intercepted by the sightline but not all clouds are spiraling toward the galaxy, etc. Our simple radial inflow model predicts inflow speeds that are at least consistent with measurements for the Milky Way and nearby galaxies.

### 3.5 Conclusion

The growth of galaxy disks requires a continuous gas supply, and studying the circumgalactic gas kinematics sheds light on how the CGM feeds galaxy disks. In this paper, we have examined the use of 3D orientation of galactic disks to constrain circumgalactic gas flow models. We have obtained new images from Keck/NIRC2 (with LGSAO) and HST/WFC3 to determine the orientation of galaxy disks on the sky. Since spiral arms trail the direction of rotation, the rotation curve measurements and the wrapping direction of spiral arms reveal the disk orientation in 3D-space, i.e., the 3D disk orientation (Figure 3.2 and 3.3).

In addition to the disk axis-ratio and position angle, defining the 3D disk orientation requires the sign of disk inclination. The sign of disk inclination indicates which way a galaxy disk tilts on the sky. Switching the sign flips the near side and the far side of the disk with respect to the observer. For a disk model with multiple velocity components

along different directions, flipping the disk changes how the velocity vectors add together, resulting in different LOS velocities and velocity ranges. With this asymmetry, gas flow models can produce a testable prediction on the sign of disk inclination, or the measured disk tilt can serve as an extra constraint for gas flow models.

We have modeled the Mg II gas kinematics measured at four quasar sightlines around  $z \approx 0.2$ , star-forming galaxies. We have selected the galaxy–quasar pairs from Paper II and Paper IV, and all sightlines intersect the inner CGM and lie within  $30^\circ$  from the galaxy major axes. We have determined the 3D disk orientation of the galaxies using the wrapping direction of spiral arms and rotation curve measurements. Together with our inflow model with gas spiraling inward near the disk plane, we have modeled the broad LOS velocity range spanned by the Mg II absorption, for which the broad velocity ranges are known to pose challenges in kinematic modeling.

Our radial inflow model and the measured disk tilt can constrain the inflow speed or rule out radial inflow detection. We have constrained the maximum radial inflow speeds for two galaxies as  $30\text{--}40 \text{ km s}^{-1}$ , consistent with inflow measurements for the Milky Way and nearby galaxies. Such inflow speeds also agree with those for galaxies of similar masses in the **EAGLE** simulations; the comparable mass inflow rates (order of unity in  $M_\odot \text{ yr}^{-1}$ ) and galaxy star formation rates suggest that the inflowing gas plausibly sustains the galaxy star-forming activities (Paper V). and the gas precesses and aligns its angular momentum vector with the pre-existing cold gas in the galactic disk (Stevens et al. 2017). Low-redshift, Milky Way-like galaxies in the **FIRE** simulations

also show order-of-unity mass inflow rates in total, which include the contribution from distinct sources of materials growing the galaxy, e.g., fresh accretion from the intergalactic medium, accretion of wind materials expelled by the galaxies themselves and/or the gas exchange between galaxies via winds (Muratov et al. 2015; Anglés-Alcázar et al. 2017). On the other hand, in contrast to using the disk tilt to constrain the inflow speed, the disk of one galaxy tilts in a direction opposite to that permitted by the model. We have thereby excluded the detection of radial inflowing gas along the sightline of this galaxy.

Our galaxies show bluer outer disks; this indicates that the outer disks are younger and less metal-rich than the inner disks, consistent with disks growing inside-out. This may seem at odd with not detecting radial inflow for the one galaxy. However, the galaxy disk may accrete gas from infalling streams, but our sightline has not fortuitously intersect the streams due to their small covering factor. The “non-detection” thereby informs us about the spatial geometry and the distribution of the feeding gas.

One of our examples has demonstrated that the disk inclination angle and the azimuthal angle of the quasar sightline also affect whether the disk tilt can effectively constrain the radial inflow speed. For a less inclined disk, the projected LOS velocity becomes insensitive to the variation of the radial inflow speed. For a sightline at small azimuthal angle, because the tangent point lies near the disk midplane, the two disk tilts produce LOS velocities that are hardly distinguishable. Hence, in the future, to search for and model radial inflow on the galactic disk plane, observers should select inclined disks and avoid  $\alpha \approx 0^\circ$  sightlines.

We thank the referee for the thoughtful comments and suggestions that improved the organization of the manuscript. The rotation curve data used here were obtained at the Apache Point Observatory (APO) 3.5-meter telescope, which is owned and operated by the Astrophysical Research Consortium. Observing time was allocated to the New Mexico State University through Chris Churchill, who is supported by the National Science Foundation under AST-1517816. These APO data were previously published in Paper II and Paper IV, and we gratefully thank our co-authors, Chris Churchill and Glenn Kacprzak, for collaborating and also conducting some of the observations. Some of the data used herein were obtained at the W. M. Keck Observatory, which is operated as a scientific partnership among the California Institute of Technology, the University of California and the National Aeronautics and Space Administration. The Observatory was made possible by the generous financial support of the W. M. Keck Foundation. The authors wish to recognize and acknowledge the very significant cultural role and reverence that the summit of Maunakea has always had within the indigenous Hawaiian community. We are most fortunate to have the opportunity to conduct observations from this mountain. This research was supported by Space Telescope Science Institute under grant HST-GO-14754.001-A and the National Science Foundation under AST-1817125.

## Chapter 4

# How Gas Accretion Feeds Galactic Disks

Numerous observations indicate that galaxies need a continuous gas supply to fuel star formation and explain the star formation history. However, direct observational evidence of gas accretion remains rare. Using the **EAGLE** cosmological hydrodynamic simulation suite, we study cold gas accretion onto galaxies and the observational signatures of the cold gas kinematics. For **EAGLE** galaxies at  $z = 0.27$ , we find that cold gas accretes onto galaxies anisotropically with typical inflow speeds between 20 and 60 km s<sup>-1</sup>. Most of these galaxies have comparable mass inflow rates and star formation rates, implying that the cold inflowing gas plausibly accounts for sustaining the star-forming activities of the galaxies. As motivation for future work to compare the cold gas kinematics with measurements from quasar sightline observations, we select an **EAGLE** galaxy with an



extended cold gas disk, and we probe the cold gas using mock quasar sightlines. We demonstrate that by viewing the disk edge on, sightlines at azimuthal angles below  $10^\circ$  and impact parameters out to 60 pkpc can detect cold gas that corotates with the galaxy disk. This example suggests that cold gas disks extending beyond the optical disks possibly explain the sightline observations that detect corotating cold gas near galaxy major axes.

## 4.1 Introduction

Observations have indicated the need for gas accretion onto galaxies. Infalling gas prolongs the gas consumption times of galaxies, or else the star formation of galaxies would exhaust the gas within a few gigayears (Gyr; Bigiel et al. 2008, 2011; Leroy et al. 2008, 2013; Rahman et al. 2012). Gas infall helps regulate galaxy star formation and is responsible for the color of galaxy disks along the Hubble sequence (Kennicutt 1998). Continuous accretion of metal-poor gas explains the relative paucity of low-metallicity stars in the disk, known as the G-dwarf problem in the solar neighborhood (van den Bergh 1962; Schmidt 1963; Sommer-Larsen 1991), and is also observed in other galaxies (e.g., Worthey et al. 1996). These observations strongly suggest the need for galaxy gas accretion.

However, direct observation of gas accretion onto galaxies remains sparse (Putman et al. 2012). Although the Milky Way (MW) is accreting gas (e.g., the Magellanic Stream; Fox et al. 2014), our location in the MW makes it difficult to detect inflowing gas besides

high-velocity clouds (Zheng et al. 2015). Beyond the local universe, the detection rate of net inflow identified from galaxy spectra stays low at roughly 5% (Martin et al. 2012; Rubin et al. 2012). These down-the-barrel galaxy observations have been challenged by the fact that inflowing gas can be identified only if the Doppler shift can be distinguished from the velocity dispersion of the interstellar medium (ISM). Otherwise, the inflowing gas will produce absorption that overlaps with the dense ISM in wavelength (or velocity) space, and the true inflow mass flux will be underestimated.

In contrast to down-the-barrel observations, transverse sightlines through the circumgalactic medium (CGM; Tumlinson et al. 2017) eliminate the problem of overlapping absorption from the intervening CGM and the ISM. Transverse sightlines probe the CGM against bright background sources such as quasars. Recent quasar sightline studies use a series of metal absorption-line systems to provide better constraints on the significant cool ( $\sim 10^4$ – $10^5$  K) gas mass in the CGM. Together with the warm-hot phase, the CGM potentially accounts for at least half and up to all of the missing baryons associated with galaxy halos (Werk et al. 2014; Prochaska et al. 2017; also see Stocke et al. 2013).

Recent measurements of circumgalactic absorption along quasar sightlines draw attention to the inhomogeneous distribution of baryons in the CGM. Sightlines along the galaxy major or minor axes frequently detect absorption systems with large equivalent widths and broad velocity ranges, but these strong absorbers are largely absent from sightlines that do not align with either of the two axes (Bouché et al. 2012; Kacprzak et al. 2012, 2015; Nielsen et al. 2015). This bimodality in spatial geometry suggests that

the position of the sightline relative to the galactic disk potentially distinguishes the origin of the circumgalactic absorption.

Sightlines along galaxy major axes often detect circumgalactic absorption with the Doppler shift sharing the same sign as the galactic disk. This implies that the CGM corotates with the galaxy disks out to large radii (Steidel et al. 2002; Kacprzak et al. 2010, 2011; Bouché et al. 2013, 2016; Diamond-Stanic et al. 2016; Paper II; Paper IV). However, a simple rotating disk poorly reproduces the broad velocity ranges spanned by the absorption (Steidel et al. 2002; Kacprzak et al. 2010, 2011; Paper II). Some studies even demonstrate that the corotation can be modeled as inflowing gas with a disk-like geometry (Bouché et al. 2016; Bowen et al. 2016; Paper II). Hence, probing the CGM along galaxy major axes provides a promising strategy to explore how galaxies obtain their gas.

From the theoretical perspective, circumgalactic gas, especially for gas accreted in “cold-mode,” has significant angular momentum, which can lead to corotation. In contrast to the “hot-mode,” where shock-heated gas cools and accretes onto the central galaxies isotropically (Fall & Efstathiou 1980; Mo et al. 1998), cold-mode gas has a cooling time shorter than the time needed to establish a stable shock (Kereš et al. 2005; Dekel & Birnboim 2006). Recent hydrodynamical simulations emphasize the importance of cold-mode accretion. In addition to accreting along filamentary streams, cold-mode gas has a higher specific angular momentum than its dark matter and hot-mode gas counterparts (Kereš et al. 2009; Brook et al. 2011; Kimm et al. 2011; Stewart et al. 2011, 2013, 2017; Teklu et al. 2015; Stevens et al. 2017).

In hydrodynamical simulations, galactic disks grow by accreting cooling, high angular momentum gas from the CGM. As gas streams fall toward a galaxy, torques generated by the disk align the infalling gas with the pre-existing disk (Danovich et al. 2012, 2015). The newly accreted gas forms an extended cold flow disk, which corotates with the galaxy out to large radii (Stewart et al. 2011, 2013). With gas accreted at later times having higher specific angular momentum, galaxy disks thereby grow inside out (Kimm et al. 2011; Pichon et al. 2011; Lagos et al. 2017; El-Badry et al. 2018).

This paper presents results from the **EAGLE** simulation suite (Crain et al. 2015; Schaye et al. 2015; McAlpine et al. 2016). **EAGLE** has been found to produce a realistic galaxy population and broadly reproduce a number of observations. These include the  $z \sim 0$  galaxy stellar mass function and the Tully–Fisher relation (Schaye et al. 2015), the evolution of galaxy masses (Furlong et al. 2015), the color bimodality of galaxies (Trayford et al. 2015, 2016), and the atomic (Bahé et al. 2016; Crain et al. 2017) and molecular gas (Lagos et al. 2015) content of galaxies. Similar to other hydrodynamical simulations that show cold gas with high specific angular momentum, Stevens et al. (2017) have demonstrated that both cooling gas and hot gas in **EAGLE** have higher specific angular momentum than the dark matter halo. Previous works using the **EAGLE** simulations (and **OWLS**; Schaye et al. 2010) have also demonstrated the importance of cold gas accretion onto galaxies (van de Voort et al. 2011; Correa et al. 2018a,b). Turner et al. (2017) have compared **EAGLE** mock spectra with metal-line absorption data of  $z \approx 2$  star-forming galaxies (Turner et al. 2014) in the Keck Baryonic Structure Survey (KBSS; Rudie et al.

2012; Steidel et al. 2014). The comparison has found evidence of infalling gas that explains the observed redshift-space distortions.

Using the **EAGLE** simulations, we examine how cold gas accretes onto galaxies and relate the gas kinematics to measurements in quasar sightline observations. We identify the inflowing gas particles using two methods: (i) the analytical ballistic approximation that predicts the motion of particles under the influence of gravity, and (ii) tracking particles through time in **EAGLE**, which includes full hydrodynamic calculations. We study and compare the inflow properties from identifying inflow particles using the two methods, and we gain insight into the factors that affect whether a cold gas particle reaches the inner galaxy within a disk rotation period. To motivate the use of **EAGLE** simulations to explain the CGM observations in the future, we use mock sightlines to probe the cold gas around one of the **EAGLE** galaxies. We identify the structural features that can reproduce the corotation signature and the broad velocity ranges detected in quasar sightline observations. We defer the spectral analysis and the use of a large galaxy sample to a future paper.

We present the paper as follows. Section 4.2 describes the **EAGLE** galaxy selection at  $z = 0.27$ , and we demonstrate that the short gas consumption time demands an external gas supply. Then we identify the cold inflowing gas that feeds the inner galaxies and examine the inflow properties. We show the results of using the ballistic approximation and particle tracking in Section 4.3 and 4.4 respectively. In Section 4.5, we probe the cold gas around an **EAGLE** galaxy using mock quasar sightlines, and we focus on the

gas structures that corotate with the disk and span broad velocity ranges. Finally, we summarize our results in Section 4.6.

## 4.2 Galaxy Selection from the EAGLE Simulation

### 4.2.1 Simulation Overview

The **EAGLE** simulation suite consists of a large number of cosmological, hydrodynamic simulations (Crain et al. 2015; Schaye et al. 2015; McAlpine et al. 2016). **EAGLE** was run on a modified version of the  $N$ -body Tree-PM smoothed particle hydrodynamics (SPH) code **GADGET-3** (last described in Springel 2005). State-of-the-art subgrid models were implemented to capture unresolved physics, including radiative cooling and photoheating, star formation, stellar evolution and enrichment, stellar feedback, black hole growth, and feedback from active galactic nuclei. The simulations also varied in cosmological volumes, resolutions, and subgrid physics, and the stellar feedback was calibrated to reasonably reproduce the sizes of disk galaxies and the galaxy stellar mass function at  $z \sim 0$ .

**EAGLE** defines galaxies as gravitationally bound subhalos identified by the **SUBFIND** algorithm (Springel et al. 2001; Dolag et al. 2009). In brief, first the friends-of-friends (FoF) algorithm (Davis et al. 1985) places dark matter particles into the same group if the particle separation is below 0.2 times the average particle separation. Baryons are associated with the same FoF halo (if any) as their closest dark matter particle. Then, within FoF halos, **SUBFIND** defines self-bound overdensity substructures as subhalos, and

Table 4.1. Characteristics of the Ref-L012N0188 simulation used in this paper.

	Simulation Property	Value
(1)	Box size $L$ (cMpc)	12.5
(2)	Number of particles $N$	$188^3$
(3)	Initial baryonic particle mass $m_g$ ( $M_\odot$ )	$1.81 \times 10^6$
(4)	Dark matter particle mass $m_{\text{dm}}$ ( $M_\odot$ )	$9.70 \times 10^6$
(5)	Gravitational softening length $\epsilon_{\text{com}}$ (ckpc)	2.66
(6)	Maximum softening length $\epsilon_{\text{prop}}$ (pkpc)	0.70

Note. — (1) Comoving box size. (2) Number of dark matter particles (initially there is an equal number of baryonic particles). (3) Initial baryonic particle mass. (4) Dark matter particle mass. (5) Comoving Plummer-equivalent gravitational softening length. (6) Maximum proper softening length.

each subhalo represents a galaxy. Within each FoF halo, the subhalo that contains the particle with the lowest value of gravitational potential is the central galaxy. The remaining subhalos are classified as satellite galaxies.

In this pilot study, we use the simulation Ref-L012N0188 with a box size of 12.5 cMpc. In the future, we will expand our study to large simulations and with higher resolutions. We summarize the simulation parameters in Table 4.1. We use the particle data output<sup>1</sup> and mainly focus on galaxies at a single “snapshot” of  $z = 0.271$ ; this redshift is comparable to the galaxy redshifts in quasar absorption-line studies that measure the CGM kinematics of low-redshift galaxies (e.g., Paper II; Paper IV). In Section 4.4, we also show results from particle tracking at time steps finer than consecutive snapshots; we use the reduced set of particle properties in “snipshots.”

---

<sup>1</sup> Particle data from snapshots can be downloaded from <http://icc.dur.ac.uk/Eagle/database.php>

### 4.2.2 Defining Cold Gas

In the simulation, we identify cold gas particles using temperature cutoffs. For most of this work, especially when we focus on cold inflowing gas (Section 4.3 and 4.4), we select cold gas using a temperature cutoff of  $2.5 \times 10^5$  K. This cutoff has been commonly used to distinguish between cold-mode and hot-mode accretion (Kereš et al. 2005, 2009; Stewart et al. 2013, 2017). However, when we compare cold gas kinematics to quasar sightline observations (Section 4.5), which detect absorption from low-ionization ions (e.g., Mg II, Si II, Fe II), we redefine the cutoff as  $3 \times 10^4$  K. This is because low ions such as Mg II do not exist at  $\sim 10^5$  K (Oppenheimer & Schaye 2013; Tumlinson et al. 2017).

In addition, we assign all star-forming gas as “cold” gas, because in **EAGLE**, the temperature of the star-forming (i.e., interstellar) gas is artificially increased to reflect the effective pressure. **EAGLE** lacks the resolution to resolve the interstellar gas phase of  $T_{\text{gas}} \ll 10^4$  K. Hence, **EAGLE** imposes a temperature floor, such that the corresponding effective equation of state prevents numerical Jeans fragmentation, due to the finite resolution (Schaye & Dalla Vecchia 2008; also see Robertson & Kravtsov 2008 and Schaye & Dalla Vecchia 2008).

### 4.2.3 Galaxy Selection

We select galaxies at  $z = 0.271$  with a stellar mass range of  $\log(M_{\star}/M_{\odot})$  between 9.5 and 10.5, comparable to that of the galaxy samples in Paper II and Paper IV, who studied the CGM kinematics of low-redshift galaxies. To measure the stellar mass of



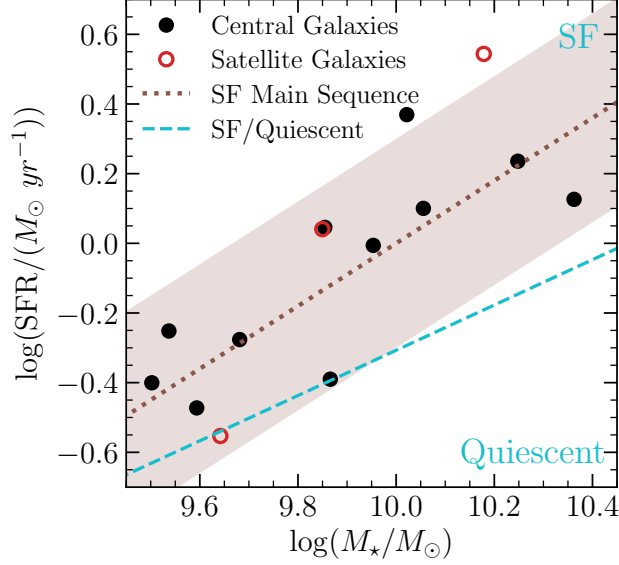


Figure 4.1: Galaxies on the SFR– $M_\star$  plane. Black filled and red empty circles represent central and satellite galaxies, respectively. The brown dotted line and the shaded region show the star-forming main sequence and the 0.3 dex scatter from Peng et al. (2010), which fit the SDSS star-forming galaxies in Brinchmann et al. (2004). The cyan dashed line divides the sample into star forming or quiescent, depending on whether the galaxies lie above or below the line (Moustakas et al. 2013). The selected galaxies lie along the main sequence, and most galaxies are star forming.

each galaxy, we use a 3D aperture with a radius of 30 pkpc from the galaxy center<sup>2</sup> and sum over the masses of star particles that belong to the subhalo (as defined in Schaye et al. 2015). Figure 4.1 shows the selected galaxies on the SFR– $M_\star$  plane, for which we use the same 30 pkpc aperture to measure the SFR. We show the SFR– $M_\star$  main sequence from Peng et al. (2010), fitted to the star-forming galaxies in the Sloan Digital Sky Survey (SDSS) from Brinchmann et al. (2004). We also plot the line that divides star-forming and quiescent galaxies (Moustakas et al. 2013); the line comes from a redshift-dependent relation using  $\sim 120,000$  galaxies with spectroscopic redshifts from

<sup>2</sup> The galaxy center is defined as the location of the most-bound particle of the subhalo.

the PRism Multi-object Survey (PRIMUS; Coil et al. 2011; Cool et al. 2013) and SDSS. Figure 4.1 shows that our selected galaxies lie along the main sequence. Star-forming galaxies dominate our sample, with most of them being central galaxies.

The halo virial masses of our sample range from  $\log(M_{\text{vir}}/M_{\odot})$  of 11.5 to 12.6. We define the virial radius  $r_{\text{vir}}$  as the radius that encloses an average density of  $\Delta_{\text{vir}}(z)\rho_c(z)$ , where  $\rho_c(z)$  represents the critical density at redshift  $z$ , and the overdensity  $\Delta_{\text{vir}}(z)$  follows the top-hat spherical collapse calculation in Bryan & Norman (1998).<sup>3</sup>

#### 4.2.4 Global Gas Consumption Timescale

The gas consumption timescale is sometimes referred to the “Roberts time” (Roberts 1963), which is defined using the following relation (Kennicutt et al. 1994, hereafter K94),

$$\tau_R = \frac{M_{\text{gas}}/\text{SFR}}{1 - R}, \quad (4.1)$$

where  $R$  is the returned gas fraction. The  $(1 - R)^{-1}$  correction factor accounts for the gas re-cycling and future time dependence on SFR. K94 have analyzed how  $(1 - R)^{-1}$  changes with different parameters, such as initial mass functions, star formation laws, and gas surface density, etc. From their time-dependent modeling of the gas return rate (from stars), they suggest that re-cycling gas extends the  $\tau_R$  of typical star-forming disks by 1.5–4 times.

For our selected EAGLE galaxies, we calculate the gas consumption time  $\tau_R$  using

---

<sup>3</sup> At  $z = 0.271$ ,  $\Delta_{\text{vir}}(z) = 124$ .

Equation (4.1). Including gas beyond the star-forming region will overestimate the actual gas depletion time in the inner galaxy regions, where star formation takes place. To avoid this overestimation, first we define the star-forming radius  $r_{\text{SFR90}}$  as the radius that encloses 90% of the galaxy SFR, and we round it up to the closest 5 pkpc.<sup>4</sup> Then, we calculate  $\tau_R$  using the gas mass and SFR within a 3D aperture of radius  $r_{\text{SFR90}}$ . In addition, we impose limits on gas temperature  $T_{\text{gas}}$  while calculating the gas mass: all  $T_{\text{gas}}$ ,  $T_{\text{gas}} \leq 2.5 \times 10^5$  K, and  $T_{\text{gas}} \leq 3 \times 10^4$  K.

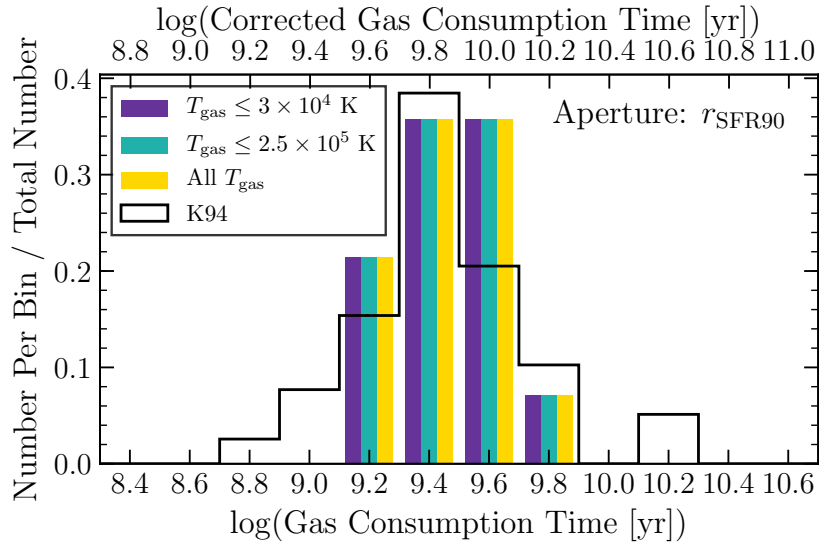


Figure 4.2: Distribution of gas consumption time. We calculate the gas consumption time using the gas mass and SFR within the star-forming radius  $r_{\text{SFR90}}$ . Within each histogram bin, different colors of the filled histograms distinguish the use of gas masses with different temperature limits. The bottom and top axes show the timescale before and after applying the gas re-cycling correction factor, i.e.,  $(1 - R)^{-1} = 1$  or 2.5. The black histogram shows the gas consumption time distribution of nearby galaxies in Kennicutt et al. (1994), and their calculation includes only the gas mass within the star-forming disk. Even with the  $(1 - R)^{-1}$  correction factor, at least half of the EAGLE galaxies have gas consumption timescales shorter than the Hubble time.

<sup>4</sup> We round up to the closest 1 pkpc, if the star-forming radius is below 5 pkpc.

Figure 4.2 shows the distribution of the gas consumption time  $\tau_R$  of the galaxies. We show  $\tau_R$  before and after applying the  $(1-R)^{-1}$  correction factor, i.e., set  $(1-R)^{-1} = 1$  or use an assumed value of 2.5. The latter is consistent with K94,<sup>5</sup> and Figure 4.2 shows that their nearby galaxy sample (black histogram) and our selected galaxies have comparable gas consumption times. If we adopt a fixed 30 pkpc aperture, i.e., the same aperture used to measure the stellar mass and SFR of a galaxy, then the  $\tau_R$  of each galaxy increases by over 50% (0.2 dex). This is because star-forming regions are generally smaller than 30 pkpc, and hence a 30 pkpc aperture includes a larger gas reservoir without increasing the SFR. This phenomenon agrees with K94, who have also shown that including gas outside the star-forming radius increases  $\tau_R$ .

The gas consumption times of several Gyr for our galaxies are also comparable to the atomic and molecular consumption timescales (uncorrected) of galaxies in other observed samples. For example, the nearby disk galaxies in the HERACLE survey have  $\text{H}_2$  consumption timescales of  $\sim 2.4$  Gyr (Bigiel et al. 2008, 2011), and the low-redshift,  $M_\star \sim 10^{10} M_\odot$  galaxies in the COLD GASS survey have H I and  $\text{H}_2$  consumption timescales of  $\sim 3$  Gyr and  $\sim 1$  Gyr respectively (Schiminovich et al. 2010; Saintonge et al. 2011); also see Section 4 of Lagos et al. (2015) for a detailed comparison of  $\text{H}_2$  consumption timescales between **EAGLE** and COLD GASS galaxies.

Furthermore, while Figure 4.2 shows that the  $\tau_R$  of the **EAGLE** galaxies do not vary significantly with the temperature cuts,  $\tau_R$  shows a stronger temperature dependence if we adopt a fixed 30 pkpc aperture. This suggests that cold gas with temperature below

---

<sup>5</sup>  $(1-R)^{-1} = 2.5$  is also adopted in other publications, e.g., Boselli et al. (2001).

$3 \times 10^4$  K dominates the total gas mass within  $r_{\text{SFR}90}$ .

Regardless of our gas temperature limit, and even if we apply the  $(1 - R)^{-1}$  correction factor, Figure 4.2 shows that the gas consumption timescales of at least half of the galaxies are significantly shorter than the Hubble time. This implies that in order to sustain the star-forming activity, the galaxies have to replenish their gas supply.

### 4.3 Identification of Inflowing Cold Gas

We aim to understand how galaxies get the gas to fuel star formation. Hot, virialized gas does not directly accrete onto galaxies. Even in the hot-mode accretion scenario, the virialized gas has to cool and condense, before being accreted to form stars. In the cold-mode scenario, the accreted gas remains cold during accretion. Therefore, we focus on the accretion of cold gas onto galaxies. In Section 4.4, by identifying inflowing gas through tracking particles, we will verify that, at least for our selected central galaxies in EAGLE, inflow from hot gas is negligible. That will justify our focus on only cold gas in this section.

We want to identify the cold gas particles that will fall into the galactic disk within a rotation period. In principle, we can do so by tracking particles through time. However, the simulation only produces snapshot output at coarse redshift (i.e., time) intervals typically larger than a rotation period. And in general, tracking the particle positions at time steps finer than the default simulation output requires rerunning the simulation, which may be impossible if one only has access to output at preset time intervals. Running

future cosmological simulations will also become more computationally expensive, making it hard or even impossible to save the full simulation output at fine time steps. As a result, the reconstruction of gas infall rates by tracking particles through time will be difficult. Therefore, in this section, we introduce a procedure to estimate the infall from the simulation output at a single time step.

We ignore pressure forces on the cold gas and calculate the orbits of gas particles in the gravitational potential. Orbits that reach pericenter beyond the galactic disk cannot feed the disk. We are interested in the orbits that intersect the galactic disk, because the collision of the cloud with the gas disk or the dense star-forming region will dissipate energy. We assume such gas will be incorporated into the disk as fuel. We then estimate a mean accretion rate and the average inflow speed over a disk rotation period. We also examine the distribution of the inflowing gas and its angular momentum. Then, in Section 4.4, we will discuss the validity and the caveats of this simple, analytical calculation of the ballistic approximation, and we will explore whether the ballistic approximation can reasonably reproduce the inflow properties. For the analysis in this section and Section 4.4, we will only focus on the central galaxies and exclude the satellite galaxies.

### 4.3.1 Ballistic Approximation

To identify the inflowing cold gas ( $T_{\text{gas}} \leq 2.5 \times 10^5$  K), we predict whether individual cold gas particles can reach the star-forming region within a rotation period. We define the star-forming region as a spherical region of radius  $r_{\text{SFR90}}$  (defined in Section 4.2.4)

from the galaxy center. We set the rotation period as  $4 \times \sqrt{3\pi/(16G\langle\rho\rangle)}$ , where  $\langle\rho\rangle$  represents the average density of the star-forming region. We calculate each particle orbit within a rotation period of the star-forming region. Each particle conserves energy and angular momentum, and the particle moves in a centrally directed gravitational field characterized by the dark matter. In the absence of hydrodynamical interactions between particles, the gravitational force determines the particle trajectory. Hence, we characterize the radial motion of each particle by

$$\ddot{r} = f_{\text{grav}}(r) + \frac{j^2}{r^3}, \quad (4.2)$$

$$\varepsilon = \frac{1}{2}\dot{r}^2 + \frac{j^2}{2r^2} + \Phi_{\text{grav}}(r), \quad (4.3)$$

where  $f_{\text{grav}}(r) = -\partial\Phi_{\text{grav}}(r)/\partial r$  represents the gravitational force per unit mass at radius  $r$ , and  $j$  and  $\varepsilon$  represent the constant specific angular momentum and energy of the particle. If the particle orbit ever intersects the star-forming region, then we consider the particle as inflowing.

We justify our assumption of gravitational force dominating over the pressure force on the cold gas as follows. Analogous to a multiphase ISM model, gases of different phases, e.g., cold ( $\sim 10^4$  K) and hot ( $\sim 10^6$  K) gas, reach pressure equilibrium and thereby share a similar pressure gradient, i.e.,  $\nabla P_{\text{cold}} \approx \nabla P_{\text{hot}}$ . The cold gas has a higher density, i.e.,  $\rho_{\text{cold}} \gg \rho_{\text{hot}}$ , because gas density scales inversely with temperature. As a result, the cold gas experiences a smaller pressure force because  $|\nabla P_{\text{cold}}/\rho_{\text{cold}}| \ll |\nabla P_{\text{hot}}/\rho_{\text{hot}}|$ . For the virialized hot gas, the pressure force balances the gravitational pull and prevents the

gas from collapsing, due to its own gravity. Because the cold gas experiences a smaller pressure force than the hot gas, the pressure force on the cold gas is negligible compared to gravity. Hence, for the cold gas, the gravitational force dominates.

We expect the ballistic approximation to break down under the following circumstances. First, if the cold gas clouds intercept hot gas with a comparable mass column density, then the cold gas will be suspended by the hot gas, which prevents the cold clouds from falling in. Because this scenario violates the assumption of the ballistic approximation that the gravitational force dominates over the pressure force, the ballistic approximation becomes invalid. Second, although we assume any gas that reaches the star-forming region will be incorporated into the disk, this ignores the presence of galactic winds. Not only can winds remove gas that has once accreted onto the star-forming disk, they can also push out gas that would otherwise be accreted. Consequently, whether the gas remains in the disk as fuel is sensitive to feedback, which the ballistic approximation ignores. Third, gas particles may lose angular momentum, due to the interactions and collisions between them, e.g., with other cold infalling gas particles or with the pre-existing disk (Danovich et al. 2015; Stevens et al. 2017).<sup>6</sup> The angular momentum dissipation thereby depends on the distribution of the gas particles and the frequency of particle collision, which the ballistic approximation ignores. Keeping these caveats in mind, we will identify the inflowing gas and predict the inflow properties using this analytical calculation. Section 4.4 will explore the validity of the ballistic approximation.

---

<sup>6</sup> Specifically, Stevens et al. (2017) used **EAGLE** and studied the change of angular momentum of the cooling gas, i.e., gas that transitioned from the hot to the cold phase, and found non-negligible angular momentum loss.



We will show that although the ballistic approximation can estimate the mass inflow rate to within a factor of 2 compared to that from particle tracking, the prediction is less accurate for the average radial inflow speed. Our analysis will thereby suggest that generally, the reconstruction of gas inflow properties, including inflow rates and inflow speeds, will benefit from simulation output at higher time cadence, e.g., at the order of the rotation timescale of  $\sim 100$  Myr.

### 4.3.2 Geometry of the Inflowing Cold Gas

In this section, we examine the distribution and the morphological structure of the inflowing cold gas. As an example, we show a galaxy (ID: 37448) in Figure 4.3, and we project the cold gas particles ( $T_{\text{gas}} \leq 2.5 \times 10^5$  K) onto 2D planes. First, panels (a) to (c) indicate that the galaxy has a rotating structure. The blueshifted and redshifted particle projected velocities clearly show that the galaxy has an approaching and a receding side. Second, panel (a) also illustrates that most particles reside in a thin structure, and the galaxy resembles a disk morphology. To visualize the distribution of the inflowing gas, in panels (d) to (f), the colors of the gas particles show whether the particles will reach the star-forming region, i.e., inflowing. Most inflowing gas particles (red dots) reside in the outer spiral arms.

Analogous to Figure 4.3, Figure 4.4 shows the remaining 10 central galaxies, and we use the same color scheme as in Figures 4.3(d) to (f) to distinguish the inflowing particles. A similar figure with particles color-coded by the particle projected velocities can be found

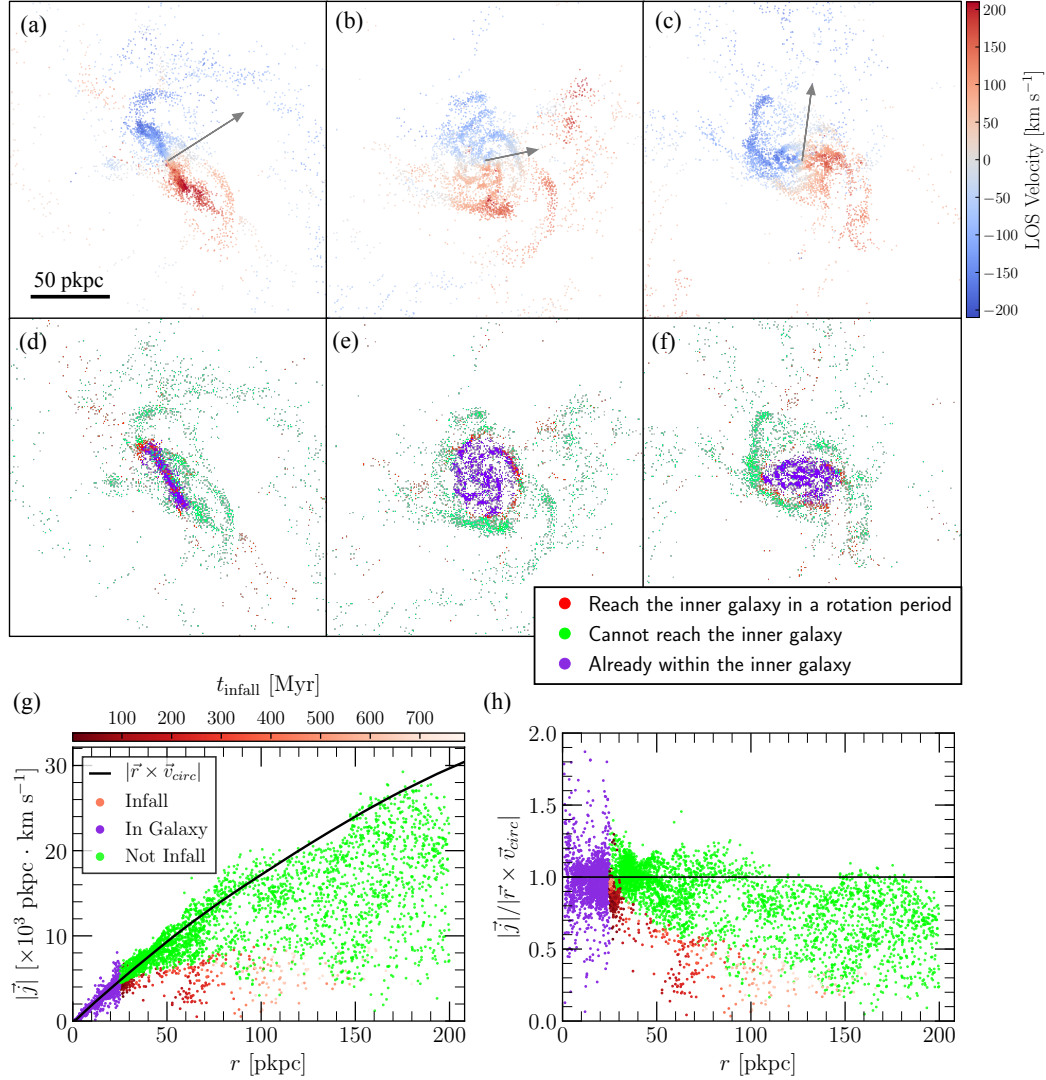


Figure 4.3: Cold gas with  $T_{\text{gas}} \leq 2.5 \times 10^5 \text{ K}$  of a disk galaxy (galaxy ID: 37448). The top two rows (panels a to f) show the projection plots of cold gas particles, and each column shows a cut in the  $x$ ,  $y$ , and  $z$  planes, respectively. Each panel is  $200 \text{ pkpc} \times 200 \text{ pkpc}$ . (*Top row, panels a to c*) Particles are color-coded by their projected line-of-sight (LOS) velocities, which clearly show a disk-like rotating structure. The gray arrows show the direction of the net angular momentum (projected onto each 2D plane) of the inner cold gas disk. The galaxy has an approaching (blueshifted) and a receding (redshifted) side, which indicates the presence of a rotating structure. (*Middle row, panels d to f*) Particles are color-coded by whether they will reach the star-forming region in our ballistic approximation. Most inflowing gas particles (red) reside at the outer spiral arms. (*Bottom row, panels g and h*) The left panel shows the specific angular momentum  $|\vec{j}|$  of each particle. The black line shows the specific angular momentum required for the particle to be rotationally supported, i.e.,  $|\vec{r} \times \vec{v}_{\text{circ}}|$ , where  $\vec{v}_{\text{circ}}$  is the circular velocity at radius  $r$ . The right panel normalizes each particle  $|\vec{j}|$  by  $|\vec{r} \times \vec{v}_{\text{circ}}|$ . Most inflowing gas particles lack sufficient angular momentum to maintain circular orbits, because  $|\vec{j}|/|\vec{r} \times \vec{v}_{\text{circ}}| < 1$  for most inflowing particles.

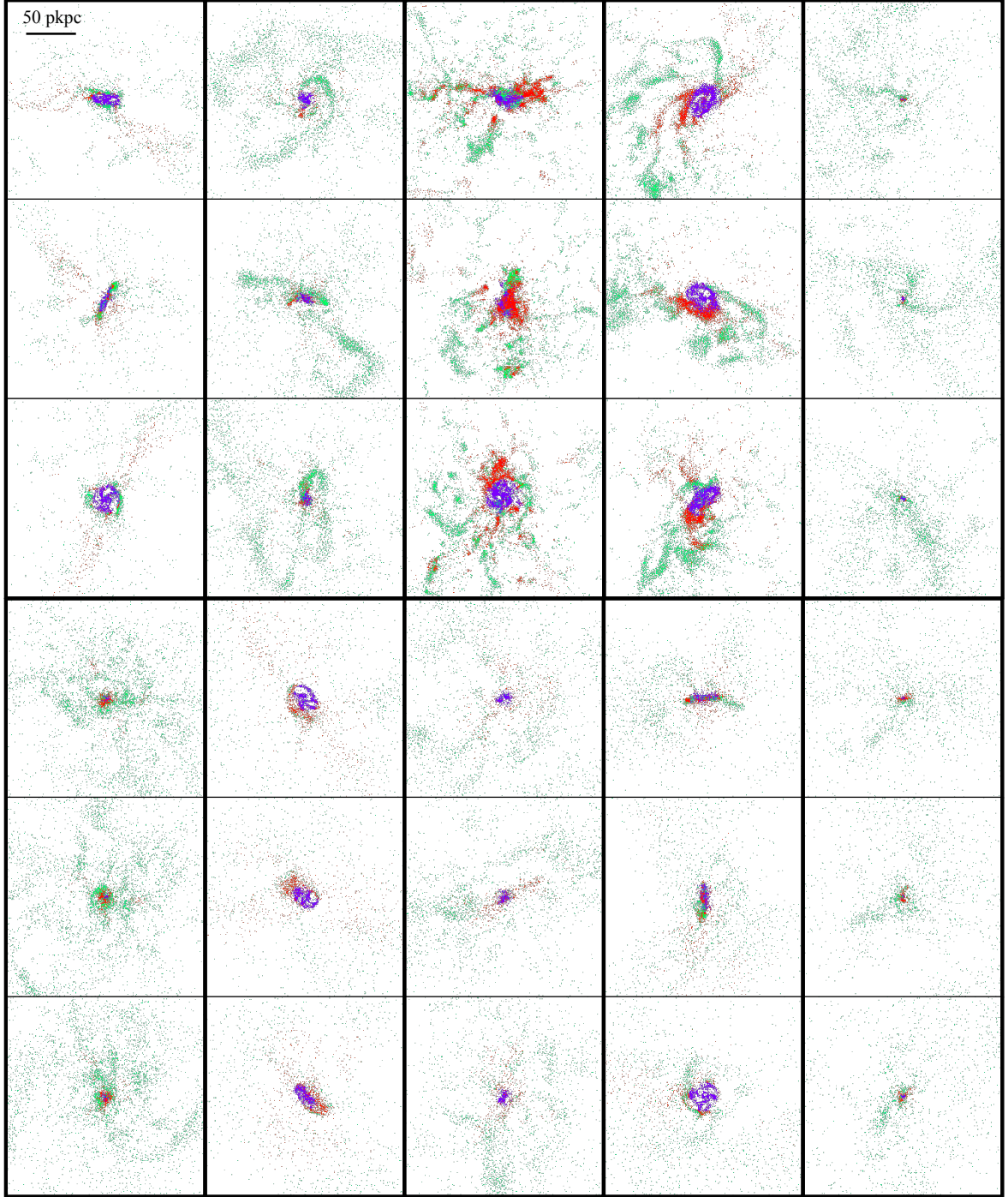


Figure 4.4: Particle projection plots showing whether the cold gas particles can reach the star-forming region within a rotation period. The particles have the same color-coding as in panels (d) to (f) of Figure 4.3. Each galaxy occupies  $3 \text{ rows} \times 1 \text{ column}$ , enclosed by the thick black lines. For individual galaxies, from top to bottom, each panel represents the cut in the  $x$ ,  $y$ , and  $z$  plane respectively, and has a side length of 200 pkpc. The plotted central galaxies are in order of decreasing stellar masses, from left to right, and top to bottom.

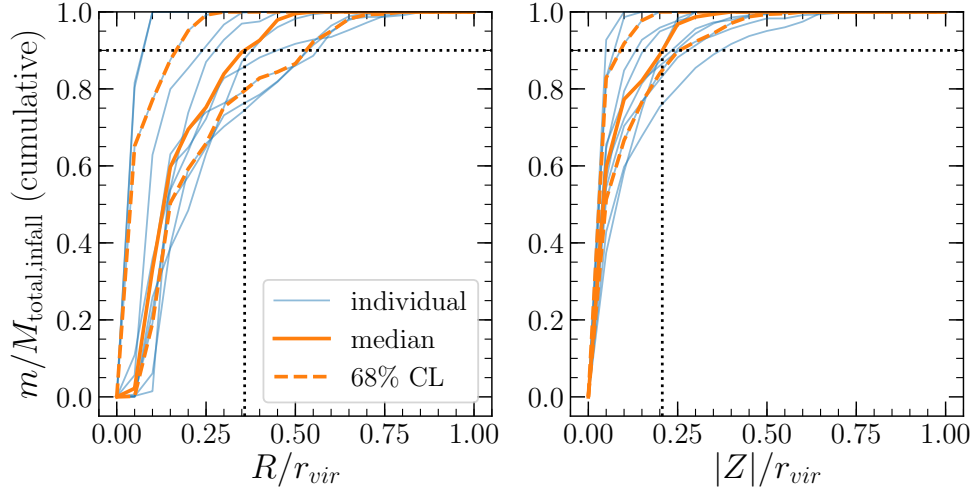


Figure 4.5: Spatial distribution of cold inflowing gas particles relative to warped disk planes. The left and the right panels show the cumulative mass profiles of the inflowing gas in the radial  $R$  and perpendicular  $|Z|$ -directions relative to the disk planes (i.e., in cylindrical coordinates), respectively. Both  $R$  and  $|Z|$  are normalized by the galaxy virial radius  $r_{\text{vir}}$ , and the mass profiles are normalized by the total mass of the infalling gas. The thin cyan lines represent individual central galaxies, and the thick orange solid and dashed lines show the median and the 68% confidence level. As measured from the median profiles, enclosing 90% of the inflowing gas mass requires  $R \approx 0.35r_{\text{vir}}$  and  $|Z| \approx 0.2r_{\text{vir}}$  (black dotted lines). The inflowing gas particles extend farther in the  $R$ -direction compared to the  $|Z|$ -direction.

in Figure C.1 of Appendix C. The particle projection plots in Figure 4.3 and 4.4 (and Figure C.1) show that despite the different morphologies among galaxies, most galaxies have rotating structures. The infalling gas particles are distributed anisotropically and form a variety of structures, e.g., particles are concentrated along streams or are located near the thin, “disk-like” structures as in Figure 4.3.

To quantify the spatial distribution of inflowing gas particles, we calculate their positions relative to the plane of the cold gas disk. For each galaxy, we define the disk plane using the net angular momentum vector of cold gas. We allow the disk plane to change with radius, because H I observations often find warped gas disks (e.g., Heald

et al. 2011; Zschaechner et al. 2012), and we measure the net angular momentum vector in concentric shells with thickness of  $\Delta r = 10$  pkpc. Figure 4.5 shows the cumulative mass profiles of the inflowing gas relative to the warped disk planes. The thin cyan lines represent individual galaxies, and the thick orange solid and dashed lines represent the median and the 68% confident levels of the sample. The profiles show that the inflowing particles extend farther in the  $R$ -direction on the disk plane than in the  $|Z|$ -direction perpendicular to the disk plane. As an illustration, the black dotted lines show that from the median profiles,  $R \approx 0.35r_{\text{vir}}$  encloses 90% of the inflowing gas mass, in contrast to  $0.2r_{\text{vir}}$  in the  $|Z|$ -direction. On the one hand,  $0.2r_{\text{vir}}$  or tens of pkpc (Table 4.2 shows  $r_{\text{vir}}$  of each galaxy) along the  $|Z|$ -direction implies that the infalling particles do not just lie on a thin disk. But on the other hand, as the inflowing gas particles extend farther in the  $R$ -direction than in the  $|Z|$ -direction, the gas tends to have a cylindrical structure, instead of an isotropic distribution.

Table 4.2: Mass inflow rate and mass-weighted average inflow speed of cold gas ( $T_{\text{gas}} \leq 2.5 \times 10^5$  K) at central galaxies

Galaxy ID	$\log(M_*/M_\odot)$	$r_{\text{vir}}$ (kpc)	SFR ( $M_\odot \text{ yr}^{-1}$ )	$\dot{M}_{\text{in}}^{\text{ballistic}}$ ( $M_\odot \text{ yr}^{-1}$ )	$\langle v_r \rangle_{\text{in}}^{\text{ballistic}}$ ( $\text{km s}^{-1}$ )	$\langle v_r \rangle_{\text{in, top10\%}}^{\text{ballistic}}$ ( $\text{km s}^{-1}$ )	$\dot{M}_{\text{in}}^{\text{tracking}}$ ( $M_\odot \text{ yr}^{-1}$ )	$\langle v_r \rangle_{\text{in}}^{\text{tracking}}$ ( $\text{km s}^{-1}$ )	$\langle v_r \rangle_{\text{in, top10\%}}^{\text{tracking}}$ ( $\text{km s}^{-1}$ )
(1)	(2)	(3)	(4)	(5)	(6)	(7)	(8)	(9)	(10)
37448	10.36	238	1.34	1.49	34	132	0.982	17	67
43166	10.25	197	1.72	2.23	62	161	1.67	42	164
32523	10.06	190	1.26	2.12	37	123	1.14	34	103
30497	10.02	219	2.34	11.5	61	206	6.57	48	140
40127	9.95	227	0.99	6.00	35	143	3.29	39	117
48386	9.87	186	0.41	0.863	30	100	0.0380	20	26
44548	9.85	185	1.11	4.14	40	155	2.89	40	148
57650	9.68	156	0.53	2.75	36	117	1.10	18	55
46369	9.59	177	0.34	1.85	45	102	1.08	59	99
51643	9.54	168	0.56	1.74	39	128	1.63	22	61
53907	9.50	166	0.40	1.73	17	49	1.15	25	57

Note. — (1) Galaxy ID. (2) Stellar mass. (3) Virial radius. (4) Star formation rate. (5) Average mass inflow rate from inflow particles in the ballistic calculation. (6) Mass-weighted average inflow speed from inflow particles in the ballistic calculation. (7) Mass-weighted average inflow speed (10% mass with highest inflow speeds) from inflow particles in the ballistic calculation. (8) Average mass inflow rate from tracking inflow particles. (9) Mass-weighted average inflow speed from tracking inflow particles. (10) Mass-weighted average inflow speed (10% mass with highest inflow speeds) from tracking inflow particles.

### 4.3.3 Angular Momentum of Inflowing Gas

Figures 4.3(g) and (h) show the specific angular momentum  $|\mathbf{j}|$  of each cold gas particle. To be rotationally supported, each particle requires a specific angular momentum of  $|j_{\text{circ}}| = |\mathbf{r} \times \mathbf{v}_{\text{circ}}|$  (solid line), where  $\mathbf{v}_{\text{circ}}$  is the circular velocity at radius  $r$ . Except for the inflowing gas at  $r \approx r_{\text{SFR90}}$ , most inflowing particles have  $|j|/|j_{\text{circ}}| < 1$ . Thus, these particles lack sufficient angular momentum to be on circular orbits. The inflowing gas of other central galaxies also show the same characteristics.

Without angular momentum, a particle will fall radially toward the galaxy center due to gravity. Angular momentum provides rotational support for a particle. Under the assumption of angular momentum conservation, the particle  $|\mathbf{j}|$  defines the pericenter of the particle orbit, and only particles with pericenters smaller than the star-forming radius  $r_{\text{SFR90}}$  can possibly be considered inflowing. In reality, however, a particle may lose angular momentum, due to tidal interactions with the existing disk. Hence, the predicted pericenter represents an upper limit, and more particles than predicted may reach  $r_{\text{SFR90}}$  within a rotation period.

### 4.3.4 Average Mass Inflow Rate and SFR

Unless galaxies replenish their gas, galaxies will eventually quench due to the lack of fuel. The inflow rate provides an important clue of whether a galaxy can sustain its star formation rate. To calculate the average mass inflow rate  $\dot{M}_{\text{in}}^{\text{ballistic}}$ , we sum over the mass of the inflowing cold gas and divide it by the rotation period of each galaxy. We list the

$\dot{M}_{\text{in}}^{\text{ballistic}}$  for individual galaxies in Table 4.2. Figure 4.6 compares  $\dot{M}_{\text{in}}^{\text{ballistic}}$  to the galaxy SFR (blue circles), and the figure shows that  $\dot{M}_{\text{in}}^{\text{ballistic}}$  exceeds the SFR for all central galaxies.

Equality between the average mass inflow rate and the galaxy SFR does not imply a sustainable star formation rate. Gas outflows remove gas from the galaxy and thereby demand a higher inflow rate to support star formation, whereas the re-cycling stellar gas reduces the need for new gas supply. In a self-sustaining evolution model, i.e., an equilibrium model, a galaxy reaches equilibrium when the gas inflow rate is equal to a linear combination of the SFR and the gas outflow rate (Bouché et al. 2010; Davé et al. 2012). Under the equilibrium condition, we express the inflow rate  $\dot{M}_{\text{gas,in}}$  as

$$\dot{M}_{\text{gas,in}} = (1 - R)\dot{M}_{\star} + \dot{M}_{\text{gas,out}}, \quad (4.4)$$

where  $\dot{M}_{\text{gas,out}}$  and  $\dot{M}_{\star}$  represent the mass outflow rate and SFR, respectively. The  $(1 - R)$  factor corrects for the gas re-cycling fraction, and hence  $(1 - R)\dot{M}_{\star}$  represents the corrected net SFR. The mass outflow rate scales with the SFR according to the mass-loading factor,  $\eta = \dot{M}_{\text{gas,out}}/\text{SFR}$ . For simplicity, we use  $R = 0.52$  as in Bouché et al. (2010).<sup>7</sup> While  $\eta$  is not well constrained in observations, due to the uncertainties in mass outflow rates, we adopt  $\eta \sim 1$  and 2 (dotted and dotted-dashed lines, respectively, in Figure 4.6), typically inferred from observations for galaxies with stellar masses similar to our **EAGLE** galaxies (Martin et al. 2012; Kacprzak et al. 2014; Heckman et al. 2015), as well as dwarf galaxies (Martin 1999) and infrared-luminous galaxies (Rupke et al. 2005).

---

<sup>7</sup> Adopting  $R = 0.6$  as in Section 4.2.4 will have a negligible effect on the equilibrium expectation in Figure 4.6.



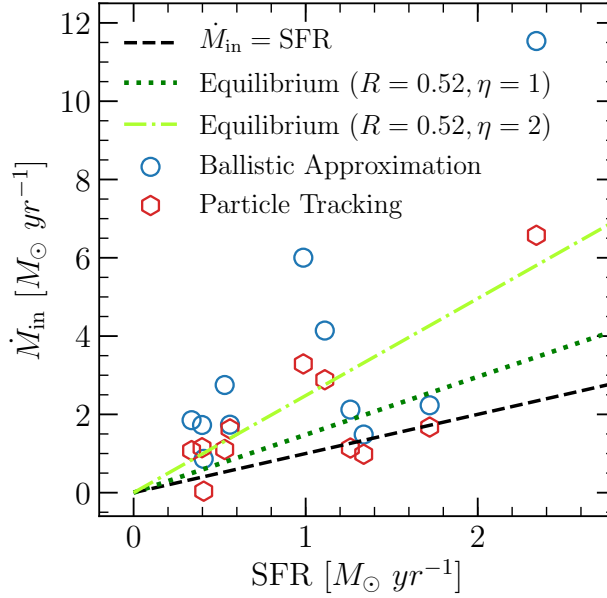


Figure 4.6: Comparison between the average mass inflow rates and SFRs of central galaxies. The ballistic approximation (blue circles) generally overestimates the cold gas inflow rate compared to particle tracking (red hexagons). The inflow rates are comparable to those suggested by the equilibrium model; we show the case for  $R = 0.52$  and  $\eta = 1$  (dotted) and  $\eta = 2$  (dotted-dashed) in Equation 4.4. The cold gas inflow plausibly accounts for sustaining the galaxy star formation activities.

Figure 4.6 shows that the inflow rates are comparable to that expected from the equilibrium models, suggesting that the cold inflowing gas plausibly accounts for sustaining the galaxy star formation activities. We further discuss the comparison between inflow rates and SFRs and the implication in Section 4.4.2.

### 4.3.5 Mass-weighted Average Inflow Speed

To estimate the average inflow speed over the rotation period, we take the mass-weighted average of the inflow speeds of individual inflowing cold gas particles. First, for each inflowing cold gas particle, we calculate its inflow speed from the change in radial distance

from the galaxy center,  $\Delta r$ , and divide it by the rotation period. However, the ballistic approximation breaks down when the particle enters the star-forming region. Once the gas particle collides with the dense gas clouds in the star-forming region and dissipates energy, our assumption of energy conservation no longer holds. Therefore, we estimate  $\Delta r$  by differencing the initial particle radial position and the star-forming radius  $r_{\text{SFR90}}$ ; we assume the particle halts once it reaches  $r_{\text{SFR90}}$ . Then, we weight the inflow speeds of all inflowing gas particles by their particle masses, and we obtain the mass-weighted average inflow speed  $\langle v_r \rangle_{\text{in}}^{\text{ballistic}}$  for each galaxy.

Table 4.2 lists the mass-weighted average inflow speed  $\langle v_r \rangle_{\text{in}}^{\text{ballistic}}$  for the central galaxies, which ranges from 17 to 62 km s<sup>-1</sup>. Although most particles have low inflow speeds, resulting in low  $\langle v_r \rangle_{\text{in}}^{\text{ballistic}}$ , the particle inflow speeds often span a large range, and the distribution has a high-velocity tail. To characterize the spread in individual inflow speeds, we also estimate the mass-weighted average inflow speed using the subset of particles with the highest inflow speeds; this particle subset accounts for 10% of the total inflowing gas mass. We show this average inflow speed from the “high-speed tail” as  $\langle v_r \rangle_{\text{in,top10\%}}^{\text{ballistic}}$  in Table 4.2. For most galaxies,  $\langle v_r \rangle_{\text{in,top10\%}}^{\text{ballistic}}$  exceeds 100 km s<sup>-1</sup>. The significant difference between  $\langle v_r \rangle_{\text{in}}^{\text{ballistic}}$  and  $\langle v_r \rangle_{\text{in,top10\%}}^{\text{ballistic}}$  demonstrates the large spread in particle inflow speeds despite the low mass-weighted average.

## 4.4 Ballistic Approximation versus Hydrodynamic Calculations

Instead of tracking particles through continuous time, the ballistic approximation provides an alternate method to predict the properties of gas inflows. To understand how the gas inflow properties from the ballistic approximation compare to those from the hydrodynamic calculations in **EAGLE**, we track the gas particles through “snipshots.” Snipshots are output from the same **EAGLE** run, sampled at finer time intervals but with less information per particle compared to the full “snapshot” output. This allows us to select the time slice around the rotation period of a galaxy. In Section 4.4.1, we explain how we track particles to define inflowing cold gas. Section 4.4.2 compares the average mass inflow rate obtained from both the ballistic approximation and particle tracking, whereas Section 4.4.3 compares the mass-weighted average inflow speed using the two methods. In Section 4.4.4, we explore how the newly accreted gas contributes to recent star formation. Section 4.4.5 discusses the limitations of the ballistic approximation and the caveats of comparing its inflow prediction to the outcome of **EAGLE**’s hydrodynamical calculations.

### 4.4.1 Tracking Gas Particles to Identify Inflowing Gas

We follow each gas particle through **EAGLE** snipshots, sampled at every  $\sim 70$  Myr around  $z \sim 0.271$ . To identify the inflowing cold gas particles for each galaxy, first we choose

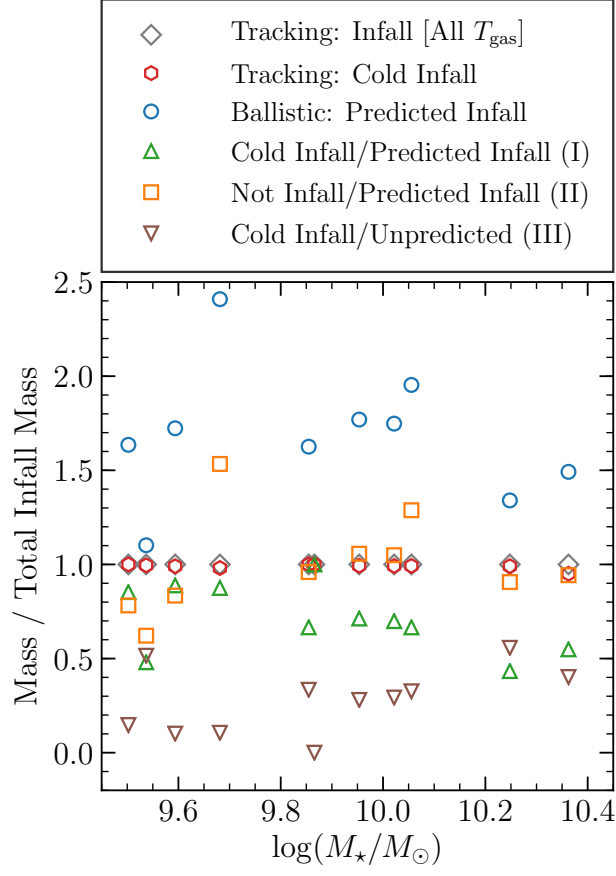


Figure 4.7: Comparison of inflowing gas mass between ballistic approximation and particle tracking. The masses of inflowing gas of different subsets (see the legend) are normalized by the total mass of inflowing gas at all temperatures. Compared to the “true” inflow mass that has reached the star-forming region, our ballistic approximation generally overestimates the inflowing mass by a factor of 1.5–2. See Section 4.4.2 for details.

the snapshot for which the time evolved from  $z = 0.271$  is closest to the galaxy rotation period. Hence, we use different snapshots for different galaxies. We define cold gas using the same criteria in Section 4.2.2. To classify a gas particle as inflowing, the particle has to reside beyond  $r_{\text{SFR90}}$  at  $z = 0.271$  and have reached  $r_{\text{SFR90}}(z = 0.271)$  or deeper after the rotation period in the selected snapshots. If this particle has been converted into a star, we still classify it as an inflowing gas particle. Because only a tiny fraction of inflowing gas particles have turned into stars after a rotation period, our conclusions will not change even if we exclude this inflowing particle subset.

In our ballistic approximation, we have assumed that inflow from hot gas is negligible and only focused on cold gas with  $T_{\text{gas}} \leq 2.5 \times 10^5$  K. Figure 4.7 justifies this assumption. Through particle tracking, comparing the inflow mass with and without applying a temperature cutoff  $T_{\text{gas}}(z = 0.271)$  (red hexagons and gray diamonds) shows that over 95% of the tracked inflowing gas (by mass) is cold. This implies that for our selected **EAGLE** galaxies, inflow from cold gas dominates.

Using the results of particle tracking and the prediction of the ballistic approximation, Figure 4.7 compares the inflowing gas mass from both methods. The inflow mass from the ballistic approximation generally exceeds the traced inflow mass by a factor of 1.5–2 (blue circles). To understand what contributes to this factor of 2 overestimation, we subdivide the gas particles into three categories: (I) predicted cold inflow from the ballistic approximation, and the particles have reached  $r_{\text{SFR90}}$  (green triangles), (II) predicted cold inflow from the ballistic approximation, but the particles still reside outside

of  $r_{\text{SFR90}}$  (orange squares), and (III) not predicted as cold inflow, but the particles have reached  $r_{\text{SFR90}}$  (inverted brown triangles). While over 50% of the predicted inflowing gas really reaches the star-forming region (type I), a significant fraction of the predicted inflow fails to be accreted (type II). In contrast, the amount of unpredicted inflowing gas (type III) stays relatively low. Therefore, the factor of 2 difference in inflowing mass comes from the correct inflow prediction, as well as from the compensation between the unpredicted inflow and the particles incorrectly predicted as inflow. As we will discuss in Section 4.4.5, this discrepancy is mainly caused by feedback.

#### 4.4.2 Average Mass Inflow Rate from Particle Tracking

We calculate the average mass inflow rate by summing the masses of identified inflow gas particles and dividing it by the time evolved from  $z = 0.271$  to the selected snapshot. Table 4.2 lists the inflow rate in column  $\dot{M}_{\text{in}}^{\text{tracking}}$ .

Figure 4.8 shows the tracked inflow rate from cold gas particles, and we compare that with the tracked inflow rate from gas at all temperatures and the predicted inflow rate from the ballistic approximation. The tracked inflow rate from cold gas matches that from gas at all temperatures. This suggests that most inflowing gas is cold (as deduced from Figure 4.7). Figure 4.8 also shows that the predicted inflow rates from the ballistic approximation correlate with the tracked inflow rates. All predicted inflow rates exceed the tracked inflow rates, however, and with the exception of two galaxies, the overestimations are within a factor of 2. For the galaxy that shows the largest

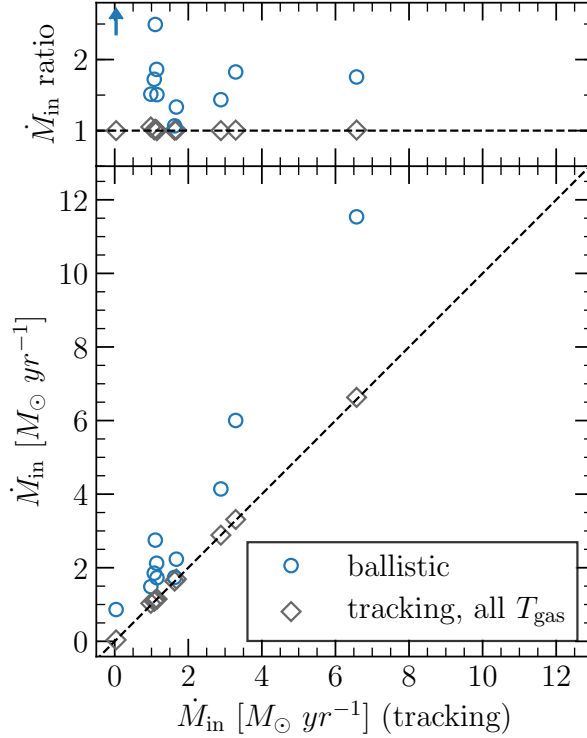


Figure 4.8: Average mass inflow rate from ballistic approximation and particle tracking. The horizontal axis shows the tracked inflow rate from cold gas ( $T_{\text{gas}} \leq 2.5 \times 10^5$  K) of the 11 central galaxies. The cyan circles show the predicted inflow rates from cold gas using the ballistic approximation, and the gray diamonds show the tracked inflow rates from gas at all temperatures. The top panel shows the ratio between each of these quantities and the tracked inflow rate from cold gas. The upward-pointing arrow indicates that the value exceeds the axis limit.

discrepancy (ID: 48386), feedback has removed most of the gas from the star-forming region, resulting in a low average inflow rate. We will discuss how feedback affects the average mass inflow rate in Section 4.4.5.

We also compare the tracked inflow rates to the galaxy SFRs in Figure 4.6 (red hexagons). Although the inflow rates from particle tracking are lower than those from the ballistic approximation, Figure 4.6 still shows that most galaxies have comparable inflow rates and SFRs. This suggests that even without other types of inflows, such as

satellite accretion and hot gas accretion (negligible as deduced in Figure 4.7), the cold gas infall alone can account for most of the fuel needed to sustain the star formation in galaxies.

### 4.4.3 Mass-weighted Average Inflow Speed from Particle Tracking

We calculate the average inflow speed as in Section 4.3.5, but with two differences. First, instead of assuming the inflowing gas particles halt at  $r_{\text{SFR90}}$ , we calculate  $\Delta r$  as the change in radial distance relative to the galaxy center. Second, we divide  $\Delta r$  by the time evolved from  $z = 0.271$  to the selected snapshot, instead of the galaxy rotation period. In Table 4.2,  $\langle v_r \rangle_{\text{in}}^{\text{tracking}}$  shows the mass-weighted average inflow speed, and  $\langle v_r \rangle_{\text{in, top10\%}}^{\text{tracking}}$  shows the mass-weighted average from only the 10% of particles by mass that have the highest inflow speeds. Figure 4.9 shows these two sets of average inflow speeds calculated from the cold gas and compares them with the predicted inflow speeds from the ballistic approximation.

The average inflow speeds calculated from particle tracking share similar characteristics to those from the ballistic approximation: (1) low mass-weighted average inflow speed of  $\lesssim 60 \text{ km s}^{-1}$ , (2) large range of individual particle inflow speeds with a “high speed tail,” and (3) if we only consider 10% of the particles by mass with the highest individual inflow speeds, then the mass-weighted average ( $\langle v_r \rangle_{\text{in, top10\%}}^{\text{tracking}}$ ) often exceeds  $100 \text{ km s}^{-1}$ . In addition, for both sets of average inflow speeds, i.e., either from all cold gas or only



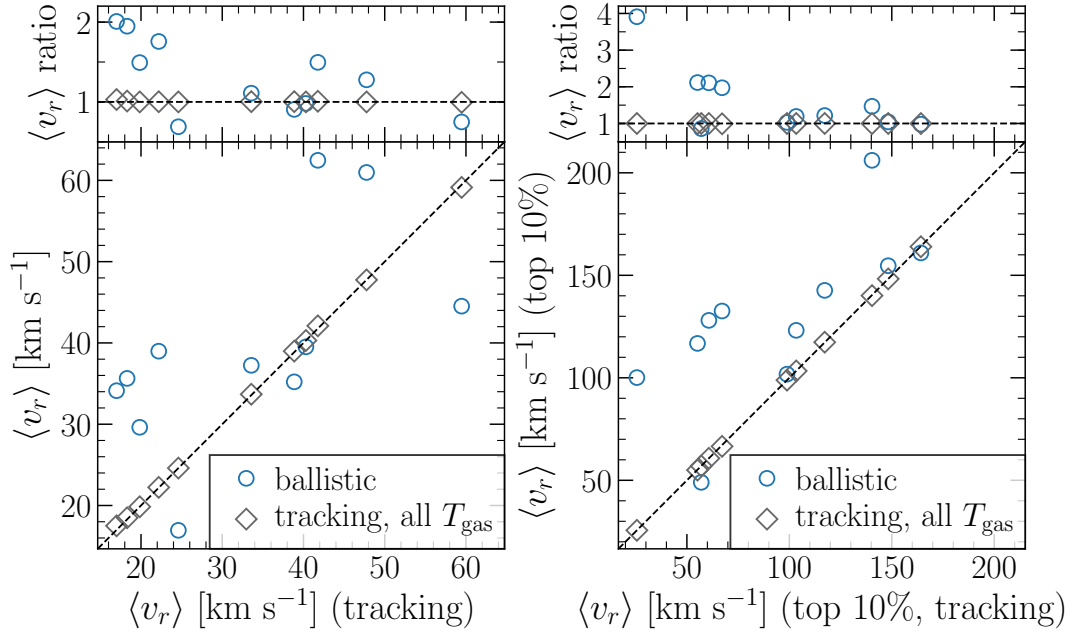


Figure 4.9: Mass-weighted average inflow speed from ballistic approximation and particle tracking. The left panel shows the mass-weighted average inflow speed, and the right panel shows the mass-weighted average calculated from 10% of the particles by mass that have the highest particle inflow speeds. Each horizontal axis shows the average inflow speed of the cold gas ( $T_{\text{gas}} \leq 2.5 \times 10^5$  K) in particle tracking. The cyan circles show the mass-weighted average from cold inflowing gas using the ballistic approximation, and the gray diamonds show the mass-weighted average of the tracked inflow gas at all temperatures. The top panels show the ratio between each of these quantities to the mass-weighted average inflow speed of the tracked cold gas (i.e., the quantity plotted on the horizontal axis).

cold gas particles at the high end of inflow speeds, the ballistic approximation overestimates the average inflow speeds for most galaxies. The differences in inflow speeds from the ballistic approximation and particle tracking mostly stay within a factor of 2. The only exception is the galaxy (ID: 48386) with feedback removing most of the gas from the star-forming region (see Section 4.4.2 and 4.4.5).

However, unlike the mass inflow rate, which shows a correlation between the prediction from the ballistic approximation and the calculation from particle tracking, inflow speeds do not reveal the same characteristic. While one possible explanation is the mismatch of

inflowing particles identified by the two methods, another reason is due to the assumption of the ballistic approximation. When we calculate the average radial inflow speed for the ballistic approximation, because the approximation breaks down when a particle interacts with the dense clouds in the star-forming region, we assume the particle halts when it reaches the star-forming region. However, in reality, where the particle ends up depends on the density and the distribution of cold gas within the star-forming region, both of which the ballistic approximation ignores. Therefore, even though the average radial inflow speeds from ballistic approximation and particle tracking agree within a factor of 2, the lack of correlation suggests that the ballistic approximation does not provide a satisfactory estimate of the inflow speed. Hence, this suggests that inflow speed estimation and, generally, the reconstruction of inflow properties, require tracking particles at series of simulation output with higher time cadence, preferably of the order of  $\sim 100$  Myr, i.e., around (or shorter than) the rotation period of a galaxy.

#### 4.4.4 Star Formation from Gas Accreted onto the Inner Galaxy

Gas accreted onto galaxies eventually forms stars. For each galaxy, we identify the gas at  $z = 0.271$  that has turned into stars at the selected snapshot after a rotation period. Although most of these particles reside within  $r_{\text{SFR}90}(z = 0.271)$  at both times, on average, around 10% of the new stars are formed from the newly accreted gas that originally resided outside of  $r_{\text{SFR}90}$ .

Figure 4.10 shows two galaxy examples, and the red points illustrate the gas particles

that have turned into stars after a rotation period. Most of these particles originally resided along the spiral arms. After a rotation period, these particles become more concentrated near each galaxy center, where some of these particles are newly accreted from outside of  $r_{\text{SFR90}}$ . This demonstrates the fueling of star-forming activity from newly accreted gas. Moreover, some stars are formed outside the star-forming radius, which indicates the growth of the star-forming disk and the stellar disk. This qualitatively supports the picture of inside-out galaxy growth.

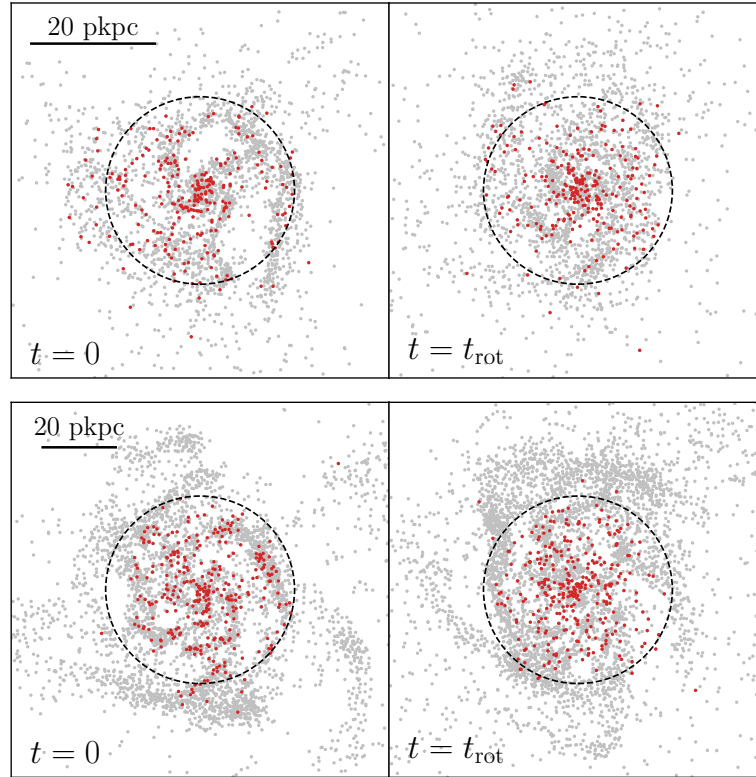


Figure 4.10: Cold gas moves toward the inner galaxy to form stars. By projecting cold gas particles onto a 2D plane, each row shows a different galaxy: 43166 (*top*) and 37448 (*bottom*). The left and right columns show the particle distribution before and after a rotation period, respectively, i.e.,  $t = 0$  at  $z = 0.271$ , and  $t = t_{\text{rot}}$ . Each gray point represents a cold gas particle at both times. Each red point represents a cold gas particle at  $z = 0.271$  (*left*) that has turned into a star after a rotation period (*right*). Each dashed circle represents the  $r_{\text{SFR90}}$  of each galaxy, defined at  $z = 0.271$ .

#### 4.4.5 Limitations of the Ballistic Approximation

Using the ballistic approximation, both predicted inflow rate and mass-weighted average velocity generally agree with those from particle tracking to within a factor of 2. In addition to the breakdown conditions of the ballistic approximation stated in Section 4.3.1, here we describe another cause of discrepancies between the two sets of inflow properties. We also discuss two caveats of comparing predictions from ballistic approximation to the outcome from the hydrodynamical calculations in **EAGLE**.

By following the gas particles in continuous time steps, i.e., at multiple times for each galaxy, we find that feedback plays an important role. The ballistic approximation ignores the effect of feedback and predicts each particle trajectory by considering only gravity. But within a rotation period, feedback and winds expel some recently accreted gas particles to large radii. In the most extreme case (galaxy ID: 48386), not only does the feedback expel the newly accreted gas, but the feedback also disrupts the star-forming region and disperses all of the cold gas.

The temperature increase of the cold gas particles also provides evidence for feedback; **EAGLE** implements the stellar feedback by stochastically heating particles to high temperature, known as the stochastic thermal feedback (Dalla Vecchia & Schaye 2008, 2012; Schaye et al. 2015). We focus on the change of temperature for particles that are predicted to reach the galaxy within a rotation period (by the ballistic approximation) but failed to do so (according to particle tracking). For the 11 central galaxies, around 50% of the particles that fail to be accreted have at least doubled their temperatures after

a rotation period; the fraction varies among galaxies, from around 30% to 75%. For the most extreme case (galaxy ID: 48386), the particles have increased their temperatures by over 100 times to  $\sim 10^7$  K, indicating that the particles are strongly affected by feedback.

Because we identify inflowing gas using the location of particles after a rotation period, we have tracked the net inflow as the difference between the newly accreted gas and the gas expelled from the galaxy due to outflows. As some particles have once reached the star-forming region but have been expelled at later times due to feedback and winds, these particles explain the non-negligible fraction of predicted inflow particles that fail to be in the star-forming region after a rotation period (orange squares in Figure 4.7). In other words, whether or not a particle can accrete onto a galaxy and stay at the star-forming region without being expelled depends strongly on feedback. This phenomenon also qualitatively agrees with the results in Nelson et al. (2015) with **AREPO** and Correa et al. (2018b) with **EAGLE**; at  $z \leq 5$  and  $z \leq 2$ , feedback suppresses the accretion rates onto galaxies with halo masses below  $10^{12} M_{\odot}$ .

We emphasize that the comparison between the ballistic approximation and particle tracking only explores whether or how well the former resembles the hydrodynamical calculations in **EAGLE**. This comparison, however, has two caveats: there exist at least two factors that will result in different inflow properties deduced from different hydrodynamical simulations. First, because whether the gas can accrete onto galaxies is sensitive to feedback, this means the method of feedback implementation and the feedback strength will alter the inflow properties deduced from hydrodynamical simulations. Second, the

inflow properties may be code dependent. Nelson et al. (2013; also see Nelson et al. 2015) studied the cosmological gas accretion of  $\simeq 10^{11} M_{\odot}$  halos at  $z = 2$ . They found that compared to the SPH code **GADGET-3**, **AREPO**, a moving mesh code, produces an order of magnitude higher in the hot accretion rate, but a factor of 2 lower in the cold accretion rate. Therefore, this demonstrates that the properties of inflowing gas are affected by the nature of the numerical approach.

## 4.5 Interpreting Cold Gas Kinematics from Observations

Previous sections have demonstrated the ubiquitousness of gas accretion onto the **EAGLE** galaxies. In contrast, observations rarely detect inflowing gas directly, as down-the-barrel galaxy observations can identify inflowing gas only if its Doppler shift can be distinguished from the ISM velocity dispersion. As a result, quasar sightline observations have provided the best observational probe of gas inflows, and these sightline observations have advanced our understanding of the gas kinematics of the CGM.

Quasar sightline observations have revealed important results regarding the cold gas kinematics of the CGM. First, through quasar sightlines that probe the CGM near galaxy major axes, observations often show that the cold CGM ( $\sim 10^4$  K), which is traced by low-ionization-state ions such as Mg II, corotates with the galaxy disks. Combining galaxy rotation curves and Mg II absorption profiles from quasar spectra, studies find

cold absorbing gas that corotates with the disks at various redshifts: from low redshifts of  $z \sim 0.1$  (Kacprzak et al. 2011) and  $z \sim 0.2$  (Paper II; Paper IV), to intermediate redshifts of  $z \sim 0.5$  (Steidel et al. 2002; Kacprzak et al. 2010). While similar types of data rarely exist at higher redshifts, there exist evidence suggesting that the cold gas shows similar kinematic properties to the lower redshift counterparts. Using other low-ionization-state ions (e.g., Zn II, Cr II), Bouché et al. (2013, 2016) studied two galaxies at  $z = 2.3283$  and  $z = 0.9096$ , respectively, and detected corotating cold gas out to 26 and 12 kpc. Second, for the observed corotating gas, the sightline impact parameters range from around 10 kpc to even  $\sim 100$  kpc. This exceeds the typical gas disk sizes of nearby galaxies measured from deep H I 21 cm observations,<sup>8</sup> e.g.,  $\sim 20$  kpc in radius down to a H I column density of  $\sim 5 \times 10^{19} \text{ cm}^{-2}$  for NGC 5023 and UGC 2082 from the HALOGAS survey (Heald et al. 2011; Kamphuis et al. 2013), and  $\sim 30$  kpc in radius for NGC 891 down to  $10^{19} \text{ cm}^{-2}$  (Sancisi & Allen 1979; Oosterloo et al. 2007). Third, the low-ion absorption typically spans over  $100 \text{ km s}^{-1}$ . Despite the corotation, a thin rotating disk fails to reproduce the broad velocity range. This problem demonstrates the need for additional components to describe the observed cold gas kinematics.

Inspired by these observations, we now observe the cold CGM kinematics in **EAGLE** using mock quasar sightlines. In this pilot study, limited by the galaxy sample size and resolution, our following discussion aims to encourage future work and focuses on one

---

<sup>8</sup> The observed H I disk size (diameter) depends on the depth of the observation; deeper observations measure H I emission down to a lower column density limit, resulting in a larger H I disk size. As an example, for NGC 5023, the H I diameter is 19 kpc at a column density limit of  $10^{20} \text{ cm}^{-2}$ , but the disk extends to about 27 kpc in diameter at  $2 \times 10^{19} \text{ cm}^{-2}$  (Kamphuis et al. 2013).

edge-on ( $i = 90^\circ$ ) galaxy. We will show that with this single galaxy, we can detect cold gas kinematics with characteristics similar to those detected in real quasar sightline observations. Therefore, this case study serves as motivation for future studies to “observe” the cold CGM using **EAGLE** simulations with larger box sizes and a higher resolution, and to include the analysis of mock absorption-line spectra.

Figure 4.11 shows the example galaxy to be studied in this section. This figure is similar to Figure 4.3, but in order to compare with cold gas traced by low-ionization-state ions, here we only show cold gas particles with  $T_{\text{gas}} \leq 3 \times 10^4$  K. Not only do the particles form a structure with a redshifted and a blueshifted side, which thereby indicates rotation, but the more extended particle distribution in the radial than in the  $Z$ -direction implies the rotating structure morphologically represents a disk (panel (a)). Furthermore, out to around 60 pkpc, the majority of the cold gas particles have angular momenta comparable to those required to be on circular orbits (panel (c)). This suggests a rotating disk radius of around 60 pkpc. Therefore, from both morphological and kinematical perspectives, this selected galaxy clearly has a giant, rotating cold gas disk.

Panel (d) shows that this extended gas disk is warped. By finding the net angular momentum vector at each concentric 10 pkpc shell, we calculate the angle between the net vector at the  $i$ th shell and that at the innermost shell, or at the  $(i - 1)$ th shell. The small but nonzero variations of both angles out to 60 pkpc imply that the disk plane changes orientation with radius, i.e., the gas disk is warped. Warped gas disks are also commonly found in hydrodynamical simulations, a result of cooling gas accreting onto



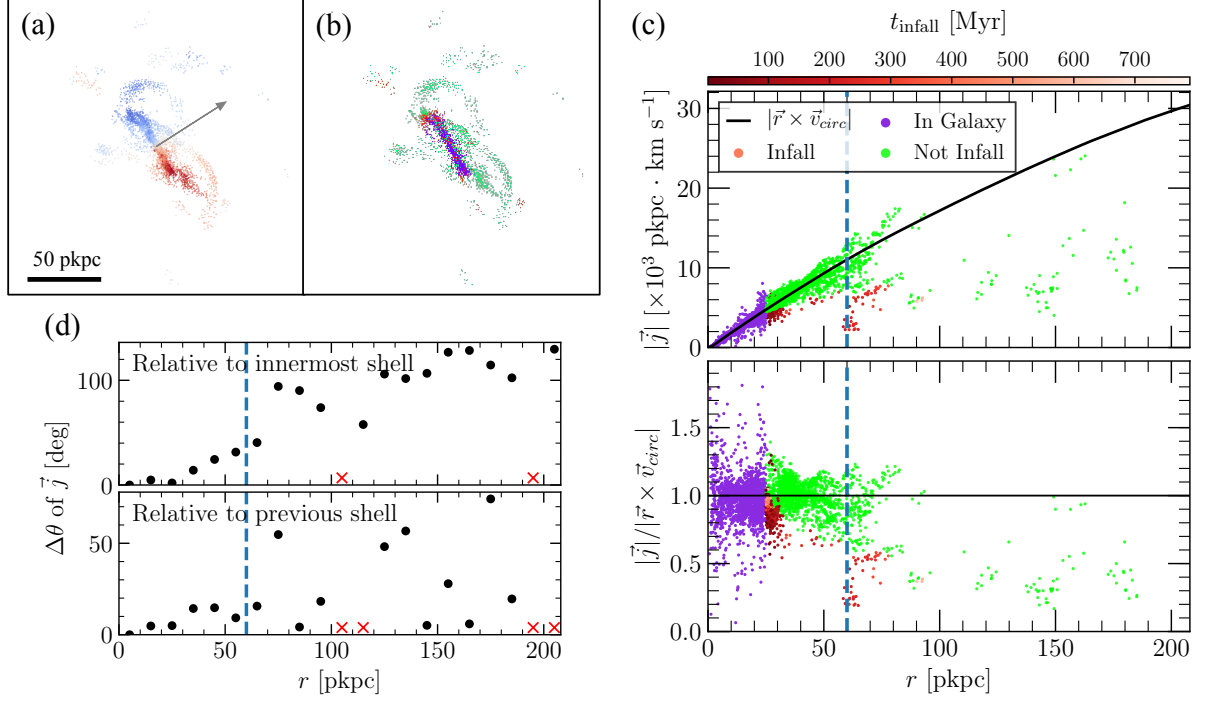


Figure 4.11: Distribution of cold gas particles ( $T_{\text{gas}} \leq 3 \times 10^4$  K) of a disk galaxy (ID: 37448) and the particle angular momenta. Panels (a) and (b) show cold gas particles projected onto 2D planes. Each particle is color-coded as in the top and middle rows, respectively, of Figure 4.3. The gray arrow in panel (a) shows the direction of the net angular momentum of cold gas at the innermost 10 pkpc disk. Similar to the bottom row of Figure 4.3, panel (c) shows the specific angular momentum of each cold gas particle. By first finding the net angular momentum vector of each concentric 10 pkpc shell, panel (d) shows the angle between the net vector at each shell ( $i$ th shell), and that at the innermost shell, or at the previous ( $(i-1)$ th) shell. Red crosses indicate cold gas particles do not exist at the  $i$ th shell (or at the  $(i-1)$ th shell). The vertical dashed lines in panels (c) and (d) mark the radius of the cold gas disk of 60 pkpc.

galaxies and aligning its angular momentum vector with the central disks (e.g., Roškar et al. 2010; Stewart et al. 2011). In particular with the **EAGLE** simulations, Stevens et al. (2017) showed that the angular momentum directions of both hot and cooling gas differ from that of the cooled gas by tens of degrees. This means that the gas particles precess as they cool, and their angular momenta align with the pre-existing cold gas in the galaxy. This leads to the formation of an extended, warped gas disk, similar to our example galaxy in Figure 4.11.

In this section, first we describe how we generate the mock sightlines in Section 4.5.1. In Section 4.5.2, by measuring the mean line-of-sight (LOS) velocities along sightlines, we explore which sightlines can detect cold gas that corotates with the galaxy disk. Then in Section 4.5.3, we study how the LOS velocity varies along sightlines, and we discuss the galaxy structures that can also produce velocity ranges comparable to those measured in real quasar sightline observations.

### 4.5.1 Creating Mock Quasar Sightlines

To create the mock quasar sightlines, first we define the disk plane of the galaxy. Within the innermost 10 pkpc of the galaxy, we calculate the net angular momentum vector of the cold gas and use this vector to define the disk plane. For a fixed galaxy inclination angle  $i$  (e.g.,  $i = 90^\circ$ ), we generate sightlines with impact parameter  $b$  between 10 and 100 pkpc and azimuthal angle<sup>9</sup>  $\alpha$  from  $0^\circ$  to  $90^\circ$ . Figure 4.12 illustrates the grid of sightlines

---

<sup>9</sup> Measured from the galaxy center, the azimuthal angle  $\alpha$  is the angular separation of the sightline from the galaxy major axis. A sightline at  $\alpha = 0^\circ$  lies on the major axis, whereas a sightline at  $\alpha = 90^\circ$  lies on the minor axis.

relative to the galaxy major axis. Then, for each combination of  $i$ ,  $b$ , and  $\alpha$ , we produce 12 LOSs by changing the location of the observer; each sightline runs along a different direction relative to the simulation box, but as viewed from the “relocated” observer, the sightlines still intersect the disk at the given  $i$ ,  $b$ , and  $\alpha$ . Moreover, because in this work we are interested in the kinematic signatures of cold gas within the halo, we create each LOS to extend only to the galaxy virial radius  $r_{\text{vir}}$ .

Analogous to observations, which trace cold gas using low ions (e.g., Mg II, Si II, Fe II), we redefine the cold gas temperature cutoff to be  $3 \times 10^4$  K (see Section 4.2.2). We use `yt` (Turk et al. 2011) to convert the cold gas particle fields to grid-based fluid quantities. We extract the cold gas density and velocity at cells intersected by each sightline. Then, we calculate the mean LOS velocity, and we explore how the LOS velocity changes along sightlines in Section 4.5.2 and 4.5.3 respectively.

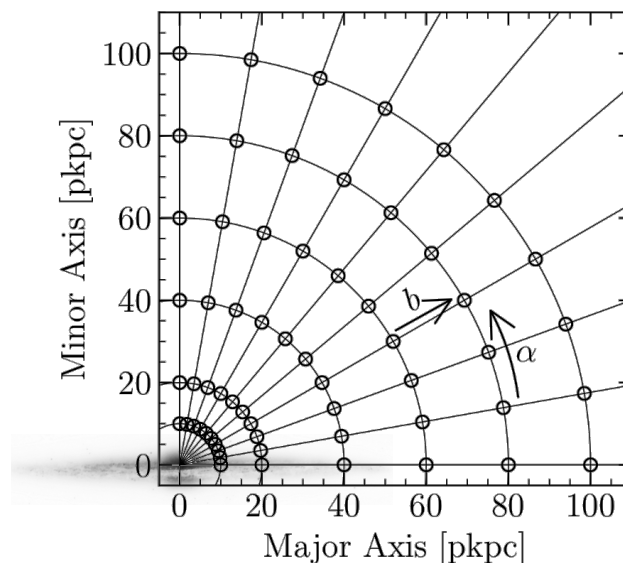


Figure 4.12: Grid of mock sightlines relative to the galaxy major axis. The origin of the coordinate grid represents the center of the galaxy. Each circle represents the position of a sightline.

### 4.5.2 CGM Corotation with Galactic Disk

We pose the question of which sightlines can detect cold gas that corotates with the inner galaxy disk. Using the mock sightlines that probe the edge-on galaxy, for each of the 12 LOSs at different  $b$  and  $\alpha$ , we calculate the mean LOS velocity (column density weighted). If this mean LOS velocity has the same sign as the disk rotation and is at least  $10 \text{ km s}^{-1}$  away from the galaxy systemic velocity, then we classify the LOS as detecting corotating gas. The latter criterion prevents misassigning cold gas that moves randomly within thermal and turbulent velocity as corotating.

Before discussing the detection of cold corotating gas, we note that not all LOSs intersect cold gas. The top panel of Figure 4.13 shows that among the 12 LOSs per  $b$ - $\alpha$  combination, the number of LOSs that intersects cold gas decreases with increasing  $b$  and  $\alpha$ . This can be explained by the decreasing cold gas density when the radial separation from the galaxy center increases (e.g., see the cold gas distribution in Figure 4.11(a)).

Using the sightlines that have intersected cold gas, we explore what ranges of  $b$  and  $\alpha$  can detect corotating gas. At each  $b$ - $\alpha$  combination, first we find the number of LOSs that intersects cold gas  $N_{\text{cold}}$  and the number of LOSs with corotating cold gas detected  $N_{\text{cr}}$ . Using binomial statistics (Gehrels 1986), we calculate the  $1\sigma$  lower limit of the rate of detection of corotating cold gas  $p_{\text{cr},1l}$ . The bottom panel of Figure 4.13 isolates the sightlines in the  $b$ - $\alpha$  plane with  $p_{\text{cr},1l} > 0.5$ ; within the  $1\sigma$  level of confidence, it is unlikely that these sightlines have randomly moving cold gas detected. This is because with random gas motion, sightlines will detect corotation at half of the time,

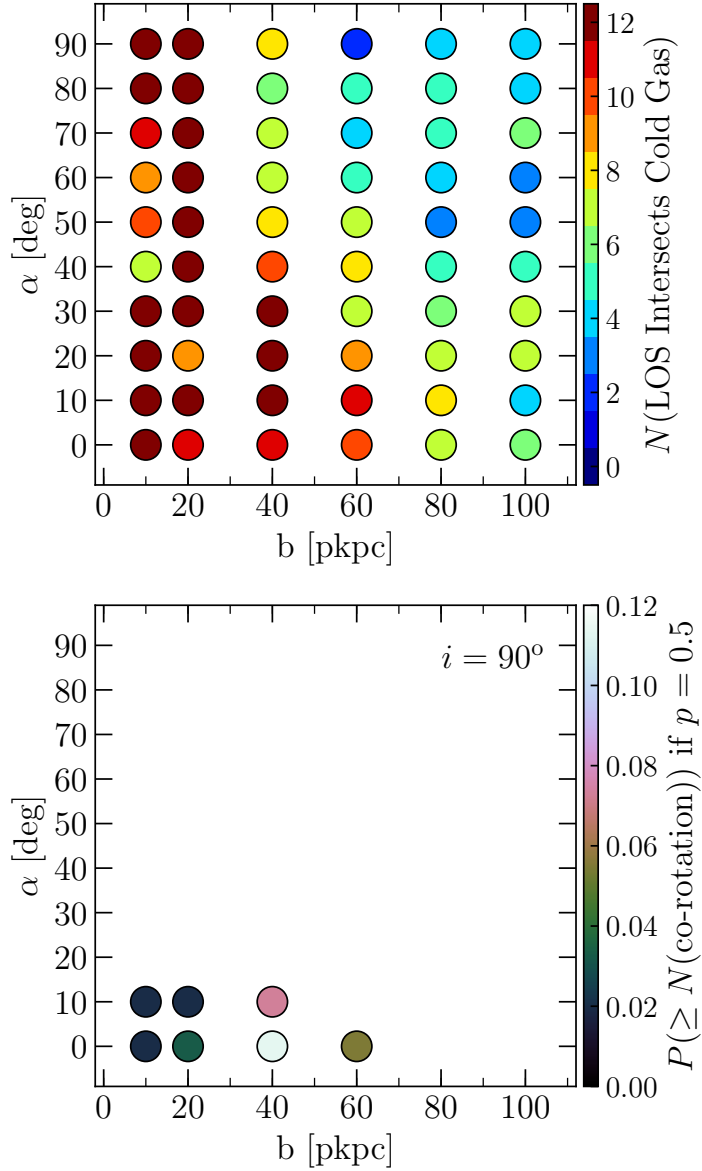


Figure 4.13: Locations of sightlines that detect corotating cold gas around an edge-on ( $i = 90^\circ$ ) galaxy (galaxy ID: 37448). (*Top*) Number of LOSs (out of 12) that intersects cold gas with  $T_{\text{gas}} \leq 3 \times 10^4$  K. Fewer LOSs at large  $b$  and high  $\alpha$  intersect cold gas within the galaxy virial radius. (*Bottom*) This panel only shows the sightlines along which we rule out random gas motion at the  $1\sigma$  level of confidence. Sightlines at  $\alpha = 0^\circ$  and  $10^\circ$  detect corotating cold gas out to 60 pkpc and 40 pkpc, respectively. In particular, *if* the gas had moved randomly, then the probabilities of detecting  $\geq N_{\text{cr}}$  LOSs with corotating cold gas at  $\alpha = 0^\circ$  and  $10^\circ$  within  $b = 20$  pkpc would lie below 5% (indicated by the colors). This implies that these sightlines have corotating cold gas detected.

and the probability of detecting corotating gas at one sightline will be  $p = 0.5$ . This probability, however, is excluded at the  $1\sigma$  level of confidence if  $p_{\text{cr},ll} > 0.5$ . Then, among these sightlines in the  $b$ - $\alpha$  plane, we also ask the following question: if the gas moves randomly, what is the probability of having  $\geq N_{\text{cr}}$  LOSs that detect corotating gas among the  $N_{\text{cold}}$  LOSs. We show this probability using the color scale in the bottom panel of Figure 4.13. Among the selected  $b$ - $\alpha$  locations, the chances of detecting  $\geq N_{\text{cr}}$  sightlines with corotating gas lie below 12%. In particular, at  $b = 10$  pkpc and 20 pkpc, the probabilities at both  $\alpha = 0^\circ$  and  $10^\circ$  lie below 5%. Thus, the calculation suggests that sightlines shown in the lower panel of Figure 4.13, i.e., sightlines at  $\alpha = 0^\circ$  and  $10^\circ$  out to 60 pkpc and 40 pkpc, respectively, have unlikely intersected randomly moving gas. In other words, we can detect corotating cold gas along these sightlines.

Our edge-on galaxy example demonstrates that quasar sightlines are more likely to detect corotating cold gas near the galaxy disk plane—at sightlines with  $b \leq 60$  pkpc and low  $\alpha$  of  $\leq 10^\circ$ . This can be naturally explained by sightlines intersecting the rotating gas disk as shown in Figure 4.11(a). Because real quasar sightline observations often detect corotating cold gas along sightlines near the galaxy major axes, our example suggests that these sightlines have likely intersected cold gas disks that extend beyond the optical disks.

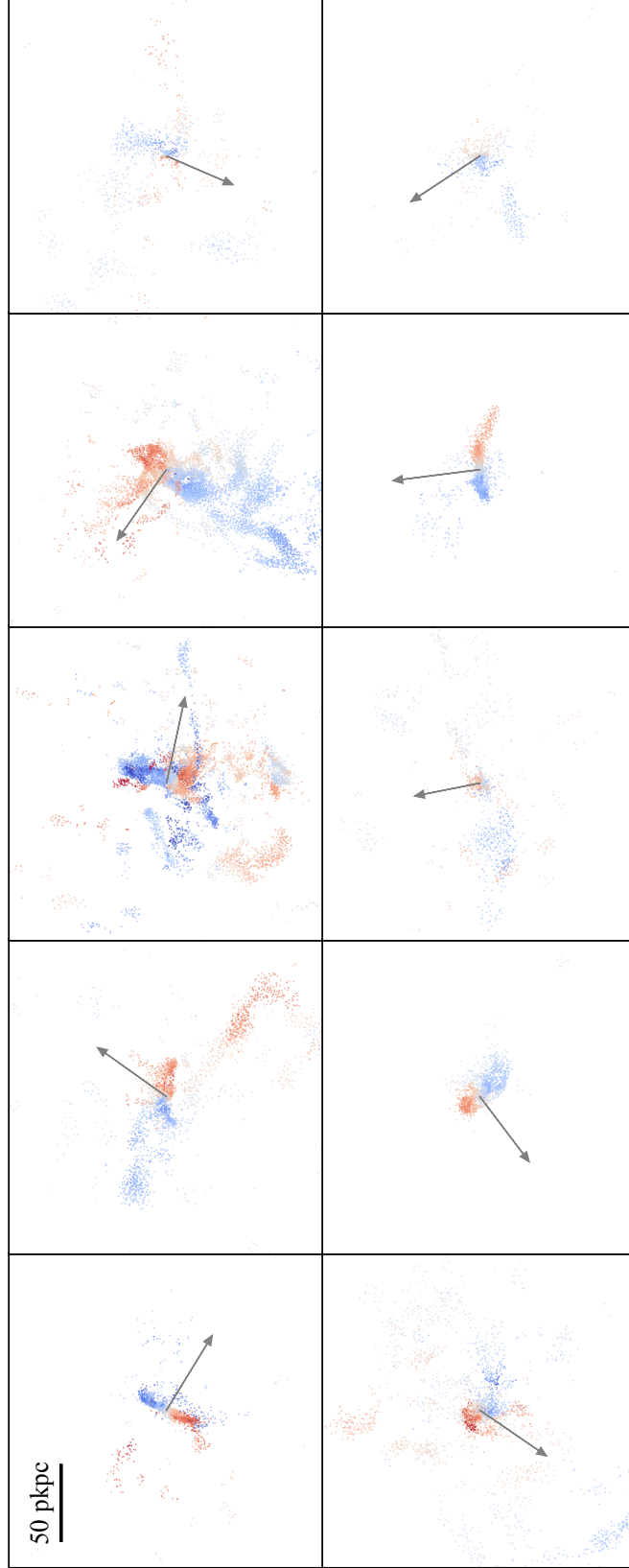


Figure 4.14: Projected LOS velocities of cold gas particles with  $T_{\text{gas}} \leq 3 \times 10^4$  K. Each panel projects the cold gas particles of each central galaxy onto a 2D plane. Every particle is color-coded by its projected LOS velocity. Red and blue colors represent redshifted and blueshifted cold gas particles, respectively, and we use the same velocity scale as in the top row of Figure 4.3. The gray arrow shows the direction of the net angular momentum of the cold gas, which is measured within an aperture of 10 pkpc from the galaxy center. More than half of the galaxies show signs of rotation. Each panel has the same spatial scale of  $200 \text{ pkpc} \times 200 \text{ pkpc}$ .

While we use one **EAGLE** galaxy to demonstrate the possibility of detecting corotating cold gas using mock quasar sightlines, the presence of rotating structures, which can give rise to corotating gas detection, is not unique to this galaxy. Figure 4.14 shows the cold gas distribution of the remaining 10 central galaxies, and we color each particle by its projected LOS velocity. Although the spatial distribution of particles indicates that not all galaxies have thin-disk-like morphologies, at least half of the galaxies have cold gas structures that show signs of rotation, i.e., an approaching side and a receding side. Rotating gas structures are not only common among our selected galaxies—simulated galaxies with halo mass  $\gtrsim 10^{11} M_{\odot}$  from the **FIRE** project also show clear signs of rotation, even though the gas distribution is not morphologically “disky” (El-Badry et al. 2018). Hence, sightlines through all these galaxies may also detect corotating cold gas as in our example, and this may imply that corotation detection is not a rare phenomenon.

### 4.5.3 Velocity Range along the LOS

Quasar sightline observations often detect broad LOS velocity ranges that cannot be explained by a thin rotating disk model. Therefore, using our example galaxy that has an extended rotating disk, we investigate the velocity ranges that this galaxy can produce.<sup>10</sup> By examining how LOS velocity varies along different sightlines, we discuss the resultant velocity ranges that can possibly be created by different gas structures.

---

<sup>10</sup> In spectroscopic observations, whether or not the cold gas can be detected and the measured velocity ranges depend on the equivalent widths of the absorption systems and the spectroscopic sensitivity. Our discussion focuses on the velocity ranges that can be produced by the cold gas, and we implicitly assume that all cold gas can be detected.



We choose individual sightlines that intersect different components of the cold gas structure: (1) the thin disk—at small  $b$  and along the galaxy major axis ( $\alpha = 0^\circ$ ) , (2) the thick disk—at small  $b$  and at least several kpc above the disk plane (e.g.,  $\alpha = 20^\circ$ ), and (3) a gas stream. Specifically for our edge-on galaxy example, a sightline that intersects the disk midplane represents the thin-disk component. Because **EAGLE** imposes a temperature floor of 8000 K to prevent metal-rich gas particles from cooling to very cold, interstellar gas (Crain et al. 2015; Schaye et al. 2015), this sets a minimum disk height, considerably larger than the physical scale height for observed edge-on galaxies (de Grijs 1998; Kregel et al. 2002). As a result, **EAGLE** cannot produce very flat galaxies (also see Lagos et al. 2018 for a related discussion). We select our sightline that intersects the thick disk component  $\sim 10$  pkpc above the disk midplane, avoiding the “unresolved” thin disk. We call this the “thick disk” component also because the 10 kpc thickness is comparable to that of the modeled rotating gas disks (tens of kiloparsecs tall) in explaining the measured CGM kinematics (e.g., Steidel et al. 2002; Paper II; Paper III).

Figure 4.15 shows the variation of the LOS velocity and cold gas density along each of the three sightlines. Along the path of each sightline,  $D_{\text{los}} = 0$  pkpc separates the near side and the far side of the edge-on disk. Although our sightlines extend to  $r_{\text{vir}}$ , we only plot  $|D_{\text{los}}| \leq 80$  pkpc. Beyond this path length, the sightlines rarely intersect any cold gas within  $r_{\text{vir}}$ . Even if cold gas is intersected, it has orders-of-magnitude lower density than the intersected cold gas within  $|D_{\text{los}}| \leq 80$  pkpc. In addition, a positive LOS velocity indicates that it has the same sign as the disk angular momentum, i.e., the

intersected cold gas corotates with the galaxy disk. For each of the three sightlines that intersect the three structures, the LOS velocities stay positive. This indicates that the intersected cold gas always shares the same sense of rotation as the inner galaxy disk. In the following, we briefly discuss the velocity variation along individual sightlines.

First, the sightline that intersects the thin disk detects the broadest LOS velocity range. The LOS velocity  $v_{\text{los}}$  reaches  $210 \text{ km s}^{-1}$  at  $D_{\text{los}} = 0$ , where the cold gas density also peaks (red line in Figure 4.15). The large  $v_{\text{los}}$  is produced by the circular motion of the gas on the disk, and the rotation velocity vector is tangent to the sightline at  $D_{\text{los}} = 0$ . Increasing  $|D_{\text{los}}|$  then reduces the magnitude of  $v_{\text{los}}$  significantly, because the LOS no longer runs in parallel with the rotation velocity vector. Along this sightline, because the LOS velocity varies from around  $30$  to  $210 \text{ km s}^{-1}$ , this sightline can detect a broad LOS velocity range of  $180 \text{ km s}^{-1}$ .

Second, the sightline that intersects the thick disk component produces a narrower velocity range. The LOS velocity reaches maxima of around  $70$  and  $110 \text{ km s}^{-1}$  at the near and the far sides of the disk, respectively, and the velocity minimum along the sightline is around  $30 \text{ km s}^{-1}$  (orange line in Figure 4.15). The density peaks at the two locations of the velocity maxima, which indicates that the thick disk component does not comprise a uniform disk. This is evident from the gas distribution in Figure 4.3, which shows the gas having spiral structures instead of being a solid disk. Because this sightline detects LOS velocity that varies from around  $30 \text{ km s}^{-1}$  to a maximum of  $110 \text{ km s}^{-1}$ , the velocity range reaches  $80 \text{ km s}^{-1}$ , which significantly exceeds the thermal line width.

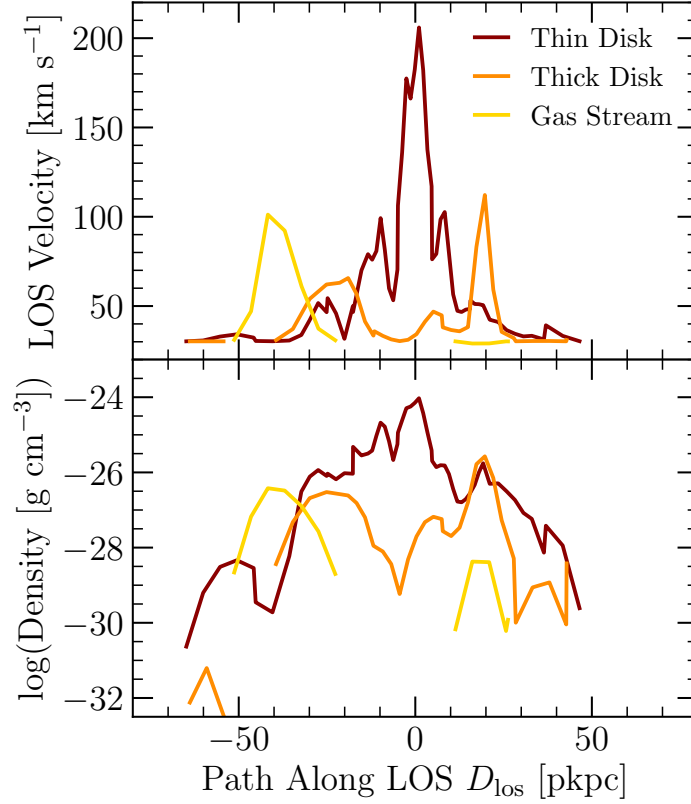


Figure 4.15: Variation of LOS velocity and cold gas density along selected sightlines of the example edge-on galaxy (galaxy ID: 37448). The top and the bottom panels show how the LOS velocity and cold gas density vary along sightlines that individually intersect three structural components: a thin disk (red), a thick disk (orange), and a gas stream (yellow). A positive LOS velocity indicates the LOS velocity has the same sign as the disk angular momentum.  $D_{\text{los}} = 0$  separates the near side and the far side of the galaxy disk with respect to the observer. Any discontinuity along  $D_{\text{los}}$  indicates that cold gas is not intersected by that section of the sightline. We only show  $|D_{\text{los}}| \leq 80$  pkpc along the path, beyond which all three sightlines rarely intersect any cold gas.

As for the sightline that intersects a gas stream, only discrete sections along the sightline have intersected cold gas. The sightline intersects the gas stream at around  $D_{\text{los}} = -40$  pkpc (yellow line in Figure 4.15). At the far side of the disk of  $D_{\text{los}} = 20$  pkpc, the sightline intersects cold gas with density 100 times lower. The higher density gas stream produces LOS velocities from around  $30 \text{ km s}^{-1}$  to a maximum of  $100 \text{ km s}^{-1}$ . Therefore, this sightline produces an LOS velocity range comparable to that of the thick disk component.

Using the three cases of our example edge-on galaxy, we have demonstrated that velocity ranges of over  $100 \text{ km s}^{-1}$  in observations can be produced by a sightline that intersects a thin rotating disk edge on. Sightlines that intersect the thick disk component or a gas stream can detect LOS velocity ranges that are significantly broader than the thermal line width. All these gas structures likely contribute to the broad line profiles in real observations, especially because the observed profiles broadened by instrumental resolution are expected to consist of multiple velocity components.

However, we emphasize that while the three example sightlines can produce broad velocity ranges in principle, such sightlines are extremely rare. As a result, they cannot explain the large number of broad absorption systems observed. Moreover, the observed velocity range of the absorption depends on the column density and thereby the ionization state of the gas, which is beyond the scope of this paper. Therefore, in the future, we will conduct the ionization analysis and use mock sightlines to study the absorption-line profiles of different ionic species. This will provide us deeper insight into the circumgalactic

gas kinematics measured in quasar sightline observations.

## 4.6 Summary and Conclusions

Galaxies grow and fuel star formation by accreting gas, yet direct observation of gas inflows onto galaxies remains sparse. In this pilot study, we have studied the properties of cold inflowing gas around **EAGLE** galaxies at  $z = 0.27$ . We have identified the cold inflowing gas using two methods: (i) a ballistic approximation that calculates the trajectories of particles moving under gravity, and then predicts which particles accrete onto the inner galaxy within a rotation period, and (ii) tracking particles through the same time interval in **EAGLE**, which includes full hydrodynamic calculations. We have compared the two sets of deduced inflow properties and discussed the limitations of the ballistic approximation. To gain insight into understanding cold gas kinematics measured from quasar sightline observations, we have probed the cold CGM ( $\sim 10^4$  K) using mock quasar sightlines. Our analysis has focused on the CGM corotation with the galactic disk, as well as the velocity ranges produced by different galaxy structures.

Using either the ballistic approximation or particle tracking, we find that the galaxies typically have low inflow speeds of around  $20\text{--}60 \text{ km s}^{-1}$ . The mass inflow rates deduced from the two methods agree to within a factor of 2, and the ballistic approximation often overestimates. We have attributed the major cause of the discrepancy to feedback, which has removed the newly accreted gas or can even disrupt the star-forming regions. In other words, feedback reduces the overall amount of cold gas accreted and thereby suppresses

the mass inflow rates. Nevertheless, the mass inflow rates are generally comparable to the galaxy SFRs. This suggests that the cold inflowing gas plausibly sustains the galaxy star formation activities and thereby prolongs the disk lifetimes.

Inspired by recent observational measurements of cold gas kinematics along quasar sightlines, we have used mock quasar sightlines to probe the cold gas within  $r_{\text{vir}}$  around a selected **EAGLE** galaxy. This galaxy has an extended cold gas disk, and the measurements of its cold gas kinematics share similar characteristics to sightline observations. This motivates future work using larger simulation boxes with a higher resolution to “observe” the cold gas kinematics in detail.

We have posed the question of which sightlines can detect cold gas that corotates with the inner galaxy disk. By viewing the selected **EAGLE** galaxy edge on, we have found that sightlines with azimuthal angles of  $\alpha = 0^\circ$  and  $10^\circ$  can detect corotating cold gas out to 60 pkpc and 40 pkpc, respectively. Because quasar sightline observations often detect corotating cold gas near the galaxy major axes, our results suggest that it is possible that the observed sightlines have intersected cold gas disks that extend beyond the optical disks.

Because quasar sightline observations also often detect broad velocity profiles, we have explored whether sightlines that individually intersect a thin-disk component, a thick-disk component (i.e., above the disk plane), and a gas stream can produce comparable velocity ranges. We have demonstrated that sightlines intersecting these three gas components can produce velocity ranges of over  $70 \text{ km s}^{-1}$ , significantly broader than the thermal line

width. All these structures possibly contribute to the broad line profiles in observational measurements, especially because the observed line profiles are expected to consist of multiple velocity components.

In the future, we will use **EAGLE** simulations with large box sizes and higher resolutions to study cold gas kinematics. With larger cosmological volumes, we can increase the sampling size of galaxies. This will produce better statistics on the probabilities of detecting corotating cold gas along sightlines and finding galaxies with extended cold gas disks. Using simulations with better resolution will allow us to generate high-resolution, mock absorption-line spectra and compare them to quasar sightline measurements. This will allow us to interpret quasar sightline observations using **EAGLE** simulations and thereby gain insight into understanding the measured cold gas kinematics.

We thank the referee for the thoughtful and detailed comments that improved the manuscript. We gratefully acknowledge Joop Schaye for the inspirational discussions on both the technical and scientific aspects of this paper. We thank Marie Lau and Michael Lipatov for their suggestions on the manuscript. We also thank Suoqing Ji and Nathan Goldbaum for the helpful discussion regarding the use of **yt**. Material presented in this paper is based in part upon work supported by the National Science Foundation under grant No. 1817125. We acknowledge the Virgo Consortium for making their simulation data available. The **EAGLE** simulations were performed using the DiRAC-2 facility at Durham, managed by the ICC, and the PRACE facility Curie based in France at TGCC,

CEA, Bruyères-le-Châtel. This work has made use of the `yt` astrophysics analysis and visualization tool (Turk et al. 2011).



# Chapter 5

## Summary and Future Prospects

The growth of galactic disks requires a continuous gas supply. Being the gas reservoir surrounding the galaxies, the CGM feeds the galactic disk and fuels the galaxy star formation. Yet, how exactly the circumgalactic gas reaches the galactic disk remains unclear. This thesis focuses on the question: how galaxies get their gas? Our observational analysis and the study using the **EAGLE** simulation suite highlight the importance of the angular momentum of the CGM. Through studying the kinematics of the inner CGM, our results shed light on understanding how gas accretes onto galaxies. The key findings of our studies are as follows.

1. No quasar sightlines within  $45^\circ$  from the galaxy major axes detect counter-rotating low-ionization Mg II gas, suggesting the gas corotates with the galactic disk.
2. The Mg II Doppler shifts detected in quasar sightlines are smaller than both the projected rotation speeds on the disk plane and the halo circular velocities, indi-

cating that the Mg II gas is sub-centrifugal.

3. Quasar sightlines near the galaxy major axes detect Mg II velocity ranges broader than a thin rotating disk model can explain. A simple radial inflow model with gas spiraling inward near the disk plane generally provides a plausible explanation for the velocity range spanned by the Mg II absorption.
4. Using the wrapping direction of the spiral arms and the galaxy rotation curve, we determined which way a galactic disk tilts on the sky and thereby established the 3D disk orientation. The disk tilt serves as an extra constraint for the radial inflow model while modeling the measured Mg II velocity ranges measured in quasar sightlines. For example, we constrained the radial inflow speed as  $30\text{--}40 \text{ km s}^{-1}$  for two galaxies and ruled out a velocity component from radial inflow in one sightline.
5. Inflowing gas around **EAGLE** galaxies have similar radial inflow speeds to those predicted by the radial inflow model in explaining the Mg II velocity ranges. The mass inflow rates of **EAGLE** galaxies are comparable to their star formation rates, indicating that the inflows can sustain the star-forming activities of the galaxies. There also exist galaxies in **EAGLE** with rotating inflow disks extending to radii comparable to the impact parameters of our quasar sightlines. Hence, the analysis with **EAGLE** further supports our inflow interpretation for the circumgalactic kinematic observations.

Altogether, our studies establish the kinematic structure of the inner CGM and rule

out the schema for the inner CGM that lacks rotation. Our results indicate that the inner CGM has significant angular momentum, and the centrifugal support of the circumgalactic gas delays accretion onto galaxies. Hence, the corotating inner CGM plausibly feeds the growth of the galactic disk and fuels the galaxy star formation activities.

While our analysis has revealed the presence of the corotating inner CGM, our results do not uniquely identify the physical structure that explains the corotation. Paper IV showed that the covering fraction of Mg II drops significantly when the sightline intersects the disk plane at radii larger than 70 kpc, beyond which the Mg II Doppler shift also no longer correlates with the projected rotation velocity on the disk plane. This suggests that at radius smaller than 70 kpc, the corotating CGM is likely axisymmetric. However, Paper II and previous work (e.g., Steidel et al. 2002; Kacprzak et al. 2010, 2011) showed that a centrifugally supported disk fails to explain the broad velocity range spanned by the Mg II absorption, ruling out the picture of the inner CGM as a thin rotating disk. Paper II and III presented a plausible model with partially centrifugally supported gas, i.e., the gas spirals towards the inner disk near the galactic disk plane. Alternatively, other structures as seen from numerical simulations potentially explain the detection of corotating circumgalactic gas, e.g., extended warped gas disks (Stewart et al. 2011, 2013), rotating structures that are less “disky” (El-Badry et al. 2018; Paper V), or inflowing gas streams from satellite winds (Hafen et al. 2018). But unless we can directly image the low-density CGM, it remains challenging for quasar sightline observations to uniquely map the physical structure of the corotating gas.

Despite being model dependent, one plausible way to understand the physical structure of the inner corotating CGM is to resolve and model individual velocity components. A single sightline possibly intersects multiple structures, e.g., the extended gas disk and the biconical outflows (Bowen et al. 2016; Diamond-Stanic et al. 2016). However, our current quasar spectra lack sufficient spectral resolution to resolve the absorption into individual components. Obtaining high resolution quasar spectra, e.g., with Keck/HIRES, would be a crucial next step for testing more complicated, multi-components kinematic models. This would allow us to better constrain the inflow and outflow properties and build a more realistic physical picture of the low-ionization-state gas in the CGM.

As we have revealed the corotating low-ionization-state gas in the CGM (i.e., the cool CGM), it opens the question of whether the warm-hot CGM also corotates with the galactic disk. The highly ionized O VI gas is commonly believed to trace the warm-hot ( $\sim 10^{5.5}$  K) CGM; the traditional viewpoint of O VI production is via collisional ionization in the warm-hot gas that cools from a virially-shocked phase. This contrasts the alternative “low pressure scenario” supported by Stern et al. (2018); O VI is produced via photoionization by the UV background and exists beyond the accretion shock at only half the virial radius. Hence, the ubiquitous detection of O VI absorption around blue,  $\sim L^*$  galaxies (Tumlinson et al. 2011) have sparked discussions regarding the ionization mechanism of the CGM, the phase structure of the CGM, and the location of the O VI gas as well as the accretion shock. Kinematically, while O VI components often demonstrate some kinematic correspondence with the low-ionization components (Werk et al. 2014,

2016), to date, only Kacprzak et al. (2019) have compared the kinematics of the O VI gas and the galactic disk. Although their 10 galaxy–quasar pairs seem to suggest the lack of correlation between the two components, this result has to be examined carefully; not only because of their small sample size, but also because of the important implications of the result. Recent hydrodynamical simulations have shown that high-ionization gas behind the virial shocks has significant rotation (Oppenheimer 2018), and the gas cools and precesses to align with the existing cold gas disk (Stevens et al. 2017). The “low pressure scenario” also predicts that the O VI corotates with the disk; O VI traces large-scale inflows, which feed the gas reservoir in the inner CGM and result in the corotation between the O VI gas and the inner CGM, and hence, the galactic disk. Therefore, the lack of correlation between the O VI gas and galactic disk kinematics in Kacprzak et al. (2019) questions these physical pictures of the O VI gas, calling for alternative explanations that also describe the observed O VI kinematics. Given that we have measured the disk and low-ionization-state gas kinematics for a uniform galaxy sample, measuring their O VI gas kinematics and compare the kinematics of all three components together would provide new insight into understanding the kinematics of the O VI absorbers. This would contribute to the recent debates on the origin of the O VI gas and improve our understanding of the interplay between the warm-hot and the cool CGM.

The physical origin of the sub-centrifugal, corotating low-ionization-state gas should also be explored. We have suggested that this gas spirals inward and feeds the galac-

tic disk, but our measurements do not distinguish among gas freshly accreted from the intergalactic medium (IGM), recycled wind materials, and satellite accretion (e.g., Ford et al. 2014; Anglés-Alcázar et al. 2017; Hafen et al. 2018). In the FIRE cosmological simulations, the inner CGM mainly consists of recycled wind materials, whereas IGM accretion dominates the CGM gas mass at the virial radius (Anglés-Alcázar et al. 2017; Hafen et al. 2018). We should conduct a similar analysis with other cosmological simulations, e.g., EAGLE, to trace the origin of the CGM. This would allow us to understand the robustness of the origin of CGM in simulations, and what causes the differences among them. We can also use the simulations to understand the role of satellites and satellite interaction in supplying chemical enriched gas to the CGM, which eventually accretes onto the galaxies (e.g., Wetzel et al. 2015), and also how merger events (especially gas rich major mergers) impact the CGM. As for observational measurements, one way to at least separate IGM accretion from the other origins is the chemical abundance; gas accreted from the IGM should have a lower metallicity, because the gas is not polluted by metals ejected from supernovae explosions.

Another possible future work related to the metallicity of the CGM is to establish its relationship with the gas-phase chemical abundance and chemical evolution of the galactic disk. Simulations show that disks grow inside out, a result from gas accreted at later time has higher specific angular momentum (Kimm et al. 2011; Pichon et al. 2011; Lagos et al. 2017). Observations also support this inside-out growth picture; a bluer outer disk than the inner disk suggests the outer disk has a younger stellar population

and a lower metallicity (Bell & de Jong 2000; Gogarten et al. 2010; Barker et al. 2011). Because galaxies accrete gas from the CGM, the CGM potentially follows a similar chemical abundance gradient, analogous to the measurements that show similar values for the stellar and gas-phase (in H II regions) abundances at the same disk radii (Bresolin et al. 2016). We can verify this simple picture by measuring the abundance gradients both across the disk and the CGM. Characterizing the abundance gradient of the CGM requires multiple sightlines, i.e., multiple quasars fortuitously located behind each galaxy. Because nearby galaxies span large angular sizes on the sky, they become the best candidates for this chemical abundance comparison. As for the chemical abundance across the disk, there exist a number of studies analyzing the gas-phase metallicities and the radial abundance profiles using the H II regions in nearby galaxies (e.g., Rosolowsky & Simon 2008; Bresolin et al. 2009; Bresolin 2011; Goddard et al. 2011; Patterson et al. 2012). Therefore, analyzing the chemical abundance across the disk and the CGM provides us an opportunity to connect the chemical evolution between the disk and the CGM, placing the study of the CGM in the larger context of galaxy formation and evolution.

# Appendix A

## The Inflow Model

To interpret the data we have presented in Papers II and III, we describe a simple model introduced by (Steidel et al. 2002, hereafter S02).<sup>1</sup> The simple model extends the galactic disk far enough in radius that the quasar sightline intersects it. The inclination of the disk and its rotation speed, which we assume are independent of radius, are well constrained by observations of the galaxy. To address the failures of this description, we introduce a radial infall model motivated by simulations that show recently accreted gas near the plane of the galactic disk (Stewart et al. 2011, 2013; Danovich et al. 2015). The full model combines these components and is described by four parameters that can be varied in order to change the velocity range of the absorption: the disk thickness  $H_{\text{eff}}$ , the velocity scale height  $h_v$ , the radial velocity  $v_R$ , and the sign of the inclination, which describes the orientation of the disk flip.

---

<sup>1</sup> We change the sign convention. We adopt a sign convention for which gas moving toward (away from) the observer will give a negative (positive) line-of-sight velocity. See Equations (A.2)–(A.4) and Figure A.1.



## A.1 Kinematic Signatures of Circular Orbits in Disks

We adopt a right-handed coordinate system with the origin at the center of the galaxy. The  $z$ -axis is perpendicular to the disk plane, i.e., the  $xy$ -plane as illustrated in Figure A.1. Without the loss of generality, we place the sightline in the  $x = p$  plane. When projected onto the sky, the  $x$ -axis is aligned with the major axis of the galactic disk, and the length of the impact parameter projected onto the galaxy major axis is  $p$ . We define  $y_0$  as the  $y$ -coordinate of the sightline where it intersects the midplane of the disk. The geometry in Figure A.1 shows that a sightline at azimuthal angle  $\alpha$  and impact parameter  $b$  is described by

$$p = b \cos \alpha \quad \text{and} \quad y_0 \cos i = b \sin \alpha . \quad (\text{A.1})$$

This geometry allows two orientations of the disk, which are indistinguishable from galaxy morphology alone. We select the positive direction of the  $z$ -axis to always lie on the quasar's side of the disk. When the  $y$ -coordinate of the quasar is positive, as shown in Figure A.1, we give the inclination of the disk a positive value. To describe the situation where the disk is rotated  $45^\circ$  about the  $x$ -axis, and the  $y$ -coordinate of the quasar becomes negative, we introduce the concept of a negative inclination. From the perspective of an observer, this flip about the major axis corresponds to interchanging the near and far sides of the disk. For circular orbits in the disk plane, the primary observable signature of this geometrical flip is the wrapping direction of trailing spiral

arms relative to the direction of rotation.

The thickness of the disk,  $H_{\text{eff}}$  in Figure A.1, and the vertical gradient in rotation speed can be varied to model the data. We describe the  $|z|$ -dependence of the rotation speed with the exponential velocity scale height,  $h_v$ , adopted by S02. Projection of this thick rotating disk,

$$\mathbf{v}_\phi(z) = v_{\text{rot}} \exp(-|z|/h_v) \hat{\phi} , \quad (\text{A.2})$$

onto the vector describing the quasar sightline,

$$\mathbf{L} = (\sin i) \hat{\mathbf{y}} + (\cos i) \hat{\mathbf{z}} , \quad (\text{A.3})$$

yields line-of-sight velocities

$$v_{\text{los}} = \mathbf{v}_\phi \cdot \mathbf{L} = \frac{v_{\text{rot}} \sin i}{\sqrt{1 + (y/p)^2}} \exp\left(-\frac{|y - y_0|}{h_v \tan i}\right) . \quad (\text{A.4})$$

With the right-handed coordinate system, the rotation velocity  $v_{\text{rot}}$  is positive (negative) when the angular momentum vector aligns with the positive (negative)  $z$ -axis of the disk. Panel (d) of Figure A.1 displays  $v_{\text{los}}$  along the sightline defined by

$$D_{\text{los}} = (y - y_0) / \sin i , \quad (\text{A.5})$$

such that  $D_{\text{los}} = 0$  represents the midplane of the disk.

The disk thickness  $H_{\text{eff}}$  sets boundaries on the range of  $y$ -values,

$$y_0 - H_{\text{eff}} \tan i < y < y_0 + H_{\text{eff}} \tan i , \quad (\text{A.6})$$

within the disk. The green shaded region in Figure A.1(d) indicates the portion of the quasar sightline within the disk. Increasing the  $H_{\text{eff}}$  broadens the range of  $v_{\text{los}}$  from the projected rotation speed at the point where the sightline is tangent to the disk,  $v_t$ , toward

an asymptotic value  $v_{los} \rightarrow 0$ .

As suggested by S02, we introduce a velocity scale height  $h_v$  to govern how quickly the rotation velocity drops from  $v_t$  toward zero with distance along the sightline. Choosing  $h_v \gg H_{\text{eff}}$  produces a linear decline in rotation speed with height above the disk

$$v_\phi(z) \approx v_{rot}(1 - |z|/h_v)\hat{\phi} . \quad (\text{A.7})$$

As a fiducial reference point, we adopt  $h_v = 10$  kpc, which produces a vertical rotation gradient consistent with measurements for extraplanar gas above nearby galaxies (Benjamin 2002, 2012).

The position–velocity ( $D_{los}$  vs.  $v_{los}$ ) diagrams illustrate the variation in line-of-sight velocity along a particular sightline. For example, consider a very large velocity scale height, which effectively describes cylindrical rotation. In the limit  $\lim h_v \rightarrow \infty$ , inspection of Equation (A.4) shows that the maximum Doppler shift is contributed by gas at  $y = 0$ . The sightline is tangent to the disk at the point  $y = 0$ , and the maximum line-of-sight velocity becomes

$$v_t \equiv v_{los}(y = 0) = v_{rot} \sin i . \quad (\text{A.8})$$

The vertical velocity gradient steepens with decreasing  $h_v$ , which moves the maximum Doppler shift along  $D_{los}$  from  $y = 0$  toward the disk midplane. The three curves in Figure A.1(d) demonstrates this shift when  $h_v$  decreases from 2000 kpc to 10 kpc. The exponential term in Equation (A.4) quantitatively describes the shift.

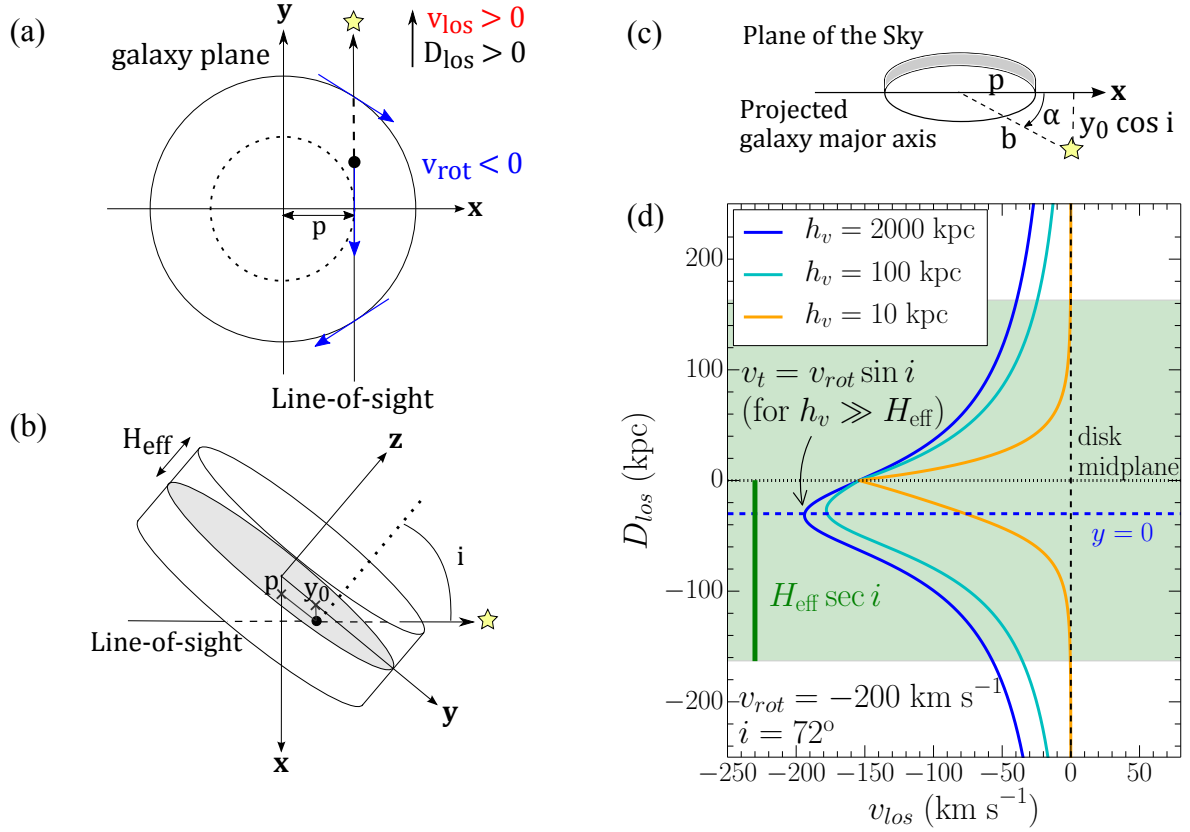


Figure A.1: Rotating disk model. The four diagrams show the setup of the coordinate system and the graphical representation of each variable, similar to those in Steidel et al. (2002) except for the direction of the sightline. These panels also show the sign conventions of line-of-sight velocity  $v_{los}$  and rotation velocity  $v_{rot}$ , with red and blue arrows indicate whether redshifted or blueshifted velocities are detected. (a) The plane of the galactic disk. (b) Side view of the disk. (c) The galaxy projected onto the sky. (d) The position–velocity diagram. The line-of-sight velocity component is plotted as a function of distance along the quasar sightline. The green shaded region indicates the portion of the sightline intersecting the disk. Decreasing the velocity scale height  $h_v$  from 2000 to 10 kpc moves the maximum Doppler shift along  $D_{los}$  from  $y = 0$  toward the disk midplane.

## A.2 Kinematics Signatures of Radial Infall in the Disk Plane

We add a velocity component so that the gas motion in the disk plane becomes

$$\mathbf{v}(R, z) = \mathbf{v}_R(R, z)\hat{\mathbf{R}} + \mathbf{v}_\phi(R, z)\hat{\boldsymbol{\phi}} . \quad (\text{A.9})$$

For purposes of illustration, we consider only constant infall speeds such that

$$\mathbf{v}_R(R, z) = v_R\hat{\mathbf{R}} , \quad (\text{A.10})$$

where  $v_R < 0$  for infalling gas.

Similar to Equation (A.4), the line-of-sight velocity due to this radial velocity component alone is

$$v_{los,R} = \mathbf{v}_R \cdot \mathbf{L} = (v_R \sin i) \frac{y}{\sqrt{y^2 + p^2}} , \quad (\text{A.11})$$

which gives a total line-of-sight velocity of

$$v_{los} = v_{los,\phi} + v_{los,R} . \quad (\text{A.12})$$

The line-of-sight velocity of the radial infall changes sign along the sightline as illustrated by Figure A.2. In the last column, the line-of-sight velocity from the rotation component lies entirely to one side of the systemic velocity while the infall component changes sign. The inflection point for the infall velocity corresponds to the point where the sightline is tangent to the disk, and the projected rotation component reaches a maximum.

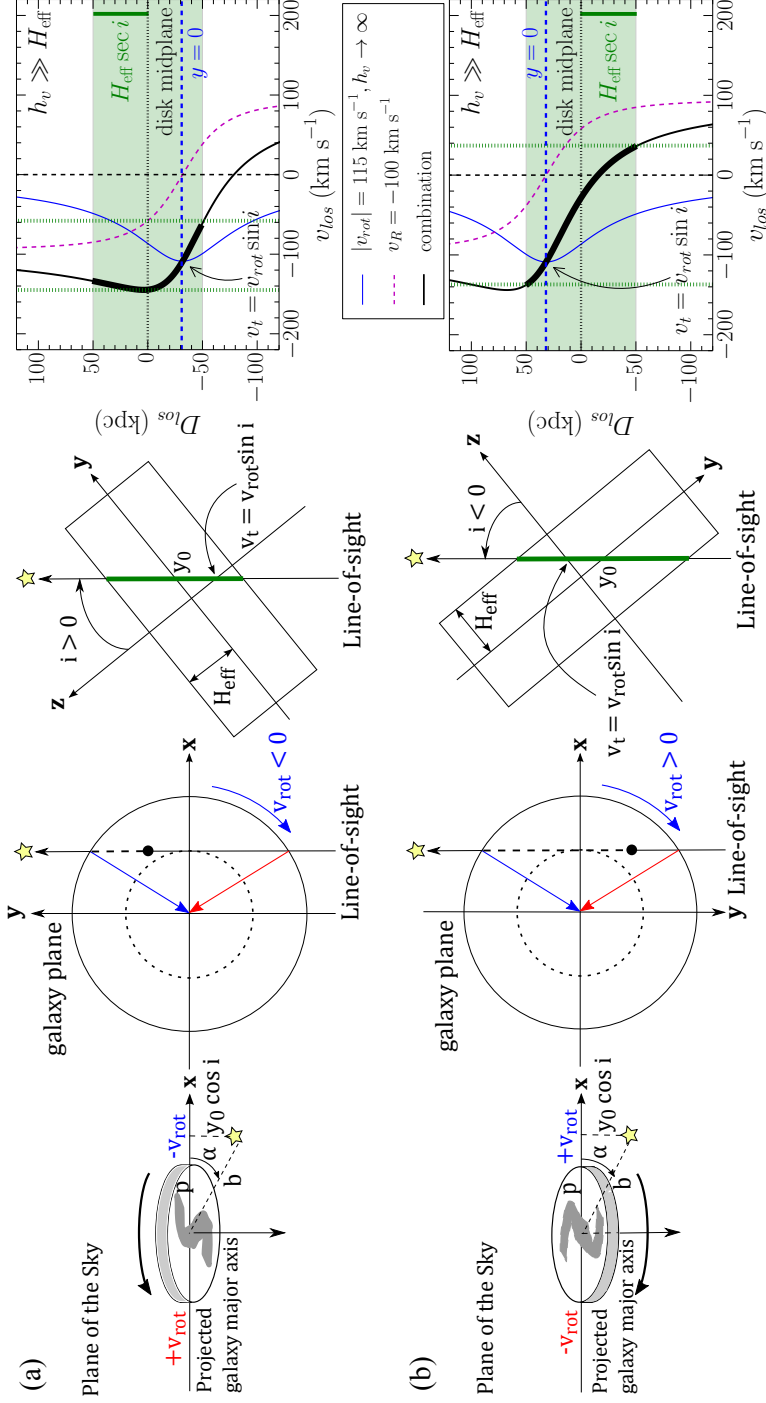


Figure A.2: Radial infall in the disk plane plus rotation. The radial infall contributes redshifted (blueshifted) absorption on the near (far) side of the sightline's passage through the disk. For a disk with a measured  $b/a$ -ratio, the two possible tilts of the disk with respect to the plane of the sky are shown; we label these as positive and negative inclinations for clarity. In the first two columns,  $v_{\text{rot}}$  changes sign between the two tilts even a blueshifted rotation component is detected along each quasar sightline; this is because the coordinate system is right-handed. The third column shows that the disk tangent point falls on opposite sides of the disk midplane for the two tilts. The  $D_{\text{los}} - v_{\text{los}}$  curves shift in the last column. Since the height of the disk ( $H_{\text{eff}}$ ) is symmetric with respect to the midplane, the portion of the sightline with gas shifts with the disk tilt. The two tilts produce absorption over a different range of velocity (enclosed by vertical green dashed lines) when inflow is included.

Flipping the disk changes how the radial and azimuthal vector velocities add together. Only in the limit of large  $H_{\text{eff}}$  will the velocity ranges of the two orientations be identical. To our knowledge, this asymmetry has not been previously described. In the last column of Figure A.2, we illustrate how the boundaries imposed by the disk thickness can lead to only one orientation producing absorption that spans the systemic velocity. We indicate the velocity range of absorption using a pair of green dashed lines. In our example, only the disk tilt with negative inclination produces absorption across the systemic velocity.

Another interesting situation is that the orientation of the flip moves the location of the maximum Doppler shift along the sightline. In our example in Figure A.2, when the disk inclination is positive, the maximum Doppler shift is contributed by gas near the disk midplane. Flipping the disk, however, moves the maximum Doppler shift away from the midplane. When the model includes radial inflow, the sign of the disk inclination therefore changes the kinematics of an absorption-line system.

## Appendix B

# Rotation Curves of Galaxies in the Quasars Probing Galaxies Program

The Quasars Probing Galaxies (QPG) program studies the kinematics of the inner CGM of  $z \approx 0.2$ , star-forming galaxies. The program targets at quasars fortuitously located behind the foreground galaxies, measures the low-ionization Mg II absorption that traces the cool ( $\sim 10^4$  K) gas, and then characterizes the circumgalactic gas kinematics relative to the reference frame of the galactic disk. Hence, in addition to measuring the Mg II absorption in the quasar spectrum, we use the galaxy spectrum to obtain the rotation curve of the galaxy. This appendix describes how we measure and model the galaxy rotation curves.

We observe the galaxy using a longslit or a slitmask; Table B.1 lists the observations. We produce the position–velocity (PV) map by fitting a Gaussian function to the



emission-line profile at different spatial positions on the two-dimensional spectra.<sup>1</sup> We then calculate the projected rotation velocity relative to the galaxy systemic redshift. To estimate the uncertainty of the velocity measured along the slit, we perturb each 2D spectrum by adding a random value within  $[-\sigma, \sigma]$  at each pixel, where  $\sigma^2$  represents the variance of the flux density. With 1000 synthetic spectra, we obtain the line centroid and its uncertainty from the median and 68% confidence interval of the probability distribution.

We model the intrinsic rotation curve using an arctan function, i.e.,

$$v(R) = v_\infty (2/\pi) \arctan(R/R_{RC}), \quad (\text{B.1})$$

where  $R$  represents the galactocentric radius, and  $v_\infty$  and  $R_{RC}$  correspond to the asymptotic rotation speed and the turnover radius, respectively. Then, we project the arctan model onto the slit. For a slitlet at an angle  $\zeta$  from the galaxy major axis, we calculate the line-of-sight (LOS) velocity  $v_{\text{los}}$  and the projected distance  $\rho$  along the slit with respect to the galaxy center using the following equations,

$$\rho = \frac{R}{\sqrt{1 + \sin^2 \zeta \tan^2 i}} \quad (\text{B.2})$$

$$v_{\text{los}}(\rho) = \frac{\sin i \cos \zeta}{\sqrt{1 + \sin^2 \zeta \tan^2 i}} v_{\text{rot}}(R), \quad (\text{B.3})$$

where  $i$  represents the disk inclination (see Table 2 of Paper IV for the disk geometry of each galaxy, e.g., the inclination and position angle (PA) of the galaxy major axis).

---

<sup>1</sup> We generally used the extended H $\alpha$  emission line to construct the PV maps. The exceptions are J123049+071050 and J160951+353838, which we used H $\beta$  and [N II]  $\lambda$ 6583, respectively.

Lastly, we convolve the projected model with a Gaussian model for the seeing disk and fit to the Doppler velocities measured along the slits.

Figures B.1 to B.6 show the PV map and the rotation curve for individual galaxy. We show two panels for each galaxy. In the top panel, the solid squares represent the LOS velocity measured along the slit, and the solid curve shows the best fit, projected rotation curve model after convolving with the seeing disk. The arrow points to the direction of the quasar sightline, i.e., whether the quasar sightline lies at the approaching or the receding side of the rotating disk. At the upper left, we state the angle  $\zeta$  between the slitlet and the galaxy major axis. For some galaxies, the measured LOS velocities are asymmetric about the galaxy systemic velocity. In that case, we offset the projected model to match the measurements; the spatial offset along the slit ( $\Delta l$ ) and the LOS velocity offset ( $\Delta v$ ) are listed in the lower right. In the bottom panel, we deproject all quantities onto the disk plane. The open circles represent the deprojected Doppler velocities at different galactocentric radii  $R$ , and the dashed line shows the rotation curve.

## Acknowledgements

Some rotation curve data were obtained at the Apache Point Observatory 3.5-meter telescope, which is owned and operated by the Astrophysical Research Consortium. Observing time was allocated to the New Mexico State University through our collaborator, Chris Churchill. We thank Chris Churchill and Glenn Kacprzak for collaborating and conducting some of the observations. Some of the data used herein were obtained at the

W. M. Keck Observatory, which is operated as a scientific partnership among the California Institute of Technology, the University of California and the National Aeronautics and Space Administration. The Observatory was made possible by the generous financial support of the W. M. Keck Foundation. The authors wish to recognize and acknowledge the very significant cultural role and reverence that the summit of Maunakea has always had within the indigenous Hawaiian community. We are most fortunate to have the opportunity to conduct observations from this mountain.

Table B.1: Observations for Galaxy Rotation Curve Measurements

Galaxy Name	Instrument	Observing Date	Exposure (s)	Slit PA
J080507+112208	APO/DIS	2017 Mar 22	7200	41.42
J081708+091750	APO/DIS	2017 Jan 7	3400	−29.00
J084235+565358	Keck/LRIS	2015 Mar 21	3520	43.46
J084725+254104	Keck/LRIS	2015 Mar 22	3520	75.00
J085215+171137	Keck/LRIS	2014 May 2	2640	−2.50
J090743+532427	Keck/LRIS	2015 Mar 21	3520	−13.00
J091954+291345	Keck/LRIS	2015 Mar 22	1760	−17.28
J095423+093711	APO/DIS	2017 Mar 22	3000	46.98
J101711+183237	APO/DIS	2017 Mar 21	7200	164.25
J102907+421737	APO/DIS	2016 Apr 10	7200	26.13
J103643+565119	Keck/LRIS	2015 Mar 22	1760	87.90
J104151+174558	APO/DIS	2016 Apr 10	7000	−20.27
J122413+495515	Keck/LRIS	2014 May 3	1760	30.00
J123049+071050	Keck/LRIS	2015 Mar 21	3520	162.69
J123249+433244	APO/DIS	2016 May 13	4200	50.00
J123318+103542	Keck/LRIS	2014 May 3	1760	255.50
J124601+173152	Keck/LRIS	2014 May 3	2640	12.73
J133541+285324	APO/DIS	2016 May 30	5200	−2.50
J133740+055211	APO/DIS	2017 Feb 22	5100	−11.29
J135051+250506	APO/DIS	2017 Mar 22	2700	160.10
J135521+303320	Keck/LRIS	2014 May 3	3520	78.93
J135733+254205	Keck/LRIS	2014 May 2	2340	−86.09
	APO/DIS	2015 Mar 25	3600	81.90
J142459+382113	APO/DIS	2016 Apr 2	5100	−41.50
J143603+375138	Keck/ESI	2016 Jun 6	2100	67.00
J144727+403217	APO/DIS	2016 May 13	4800	−46.80
J145844+170522	APO/DIS	2016 May 30	4200	8.00
J152027+421519	APO/DIS	2016 Apr 2	4500	−86.50
J153546+391932	Keck/ESI	2016 Jun 6	1000	201.00
J154454+165703	Keck/LRIS	2015 Mar 22	2640	−16.65
J154741+343350	Keck/LRIS	2014 May 3	1760	38.72
J155505+362848	APO/DIS	2016 Jul 4	3200	141.20
J160906+441721	Keck/LRIS	2015 Mar 21–22	5280	44.83
J160951+353838	Keck/LRIS	2014 May 2	1760	24.16
J165930+373527	APO/DIS	2013 Jul 12	4400	10.00

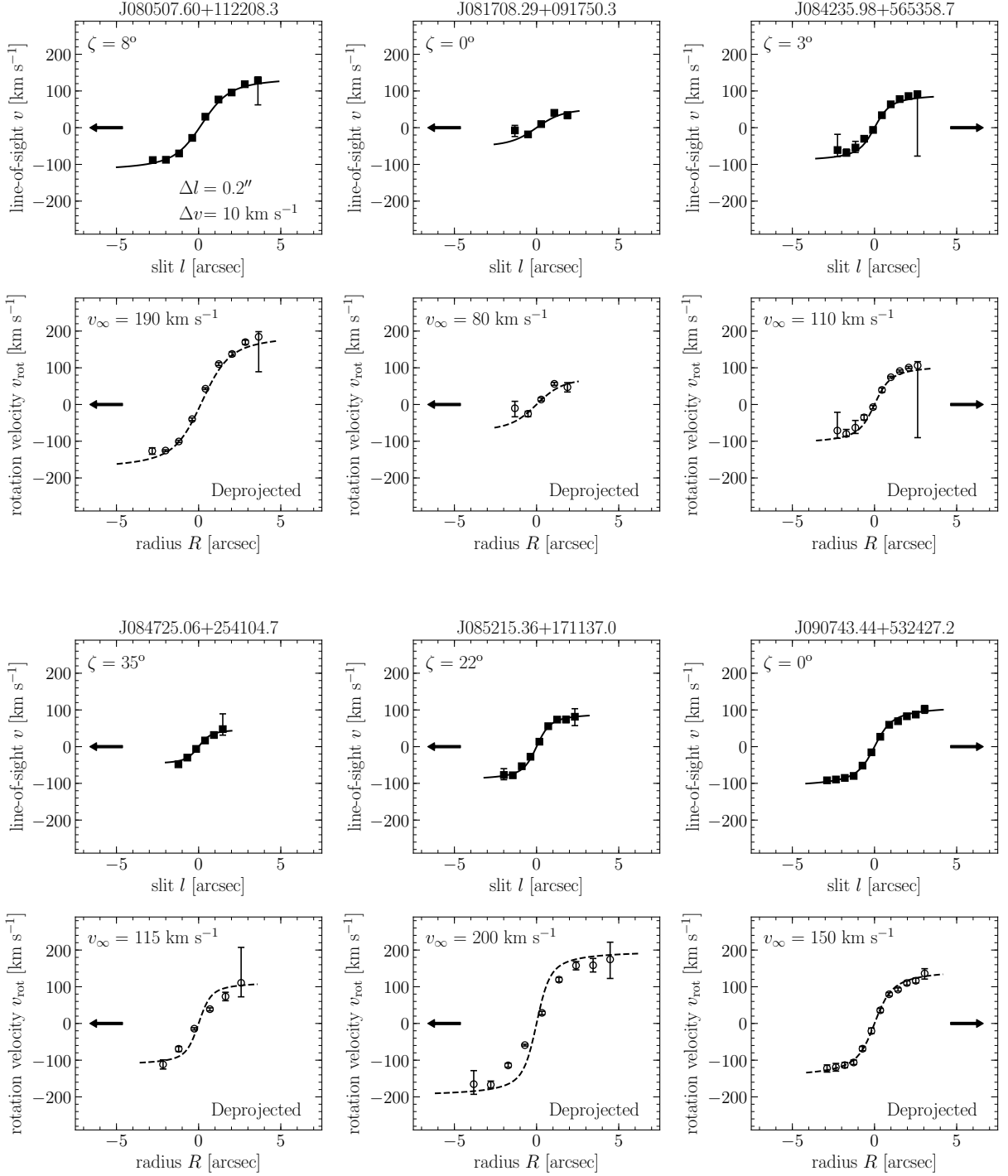


Figure B.1: Position-velocity maps and rotation curves for individual galaxies. See the main text for details.

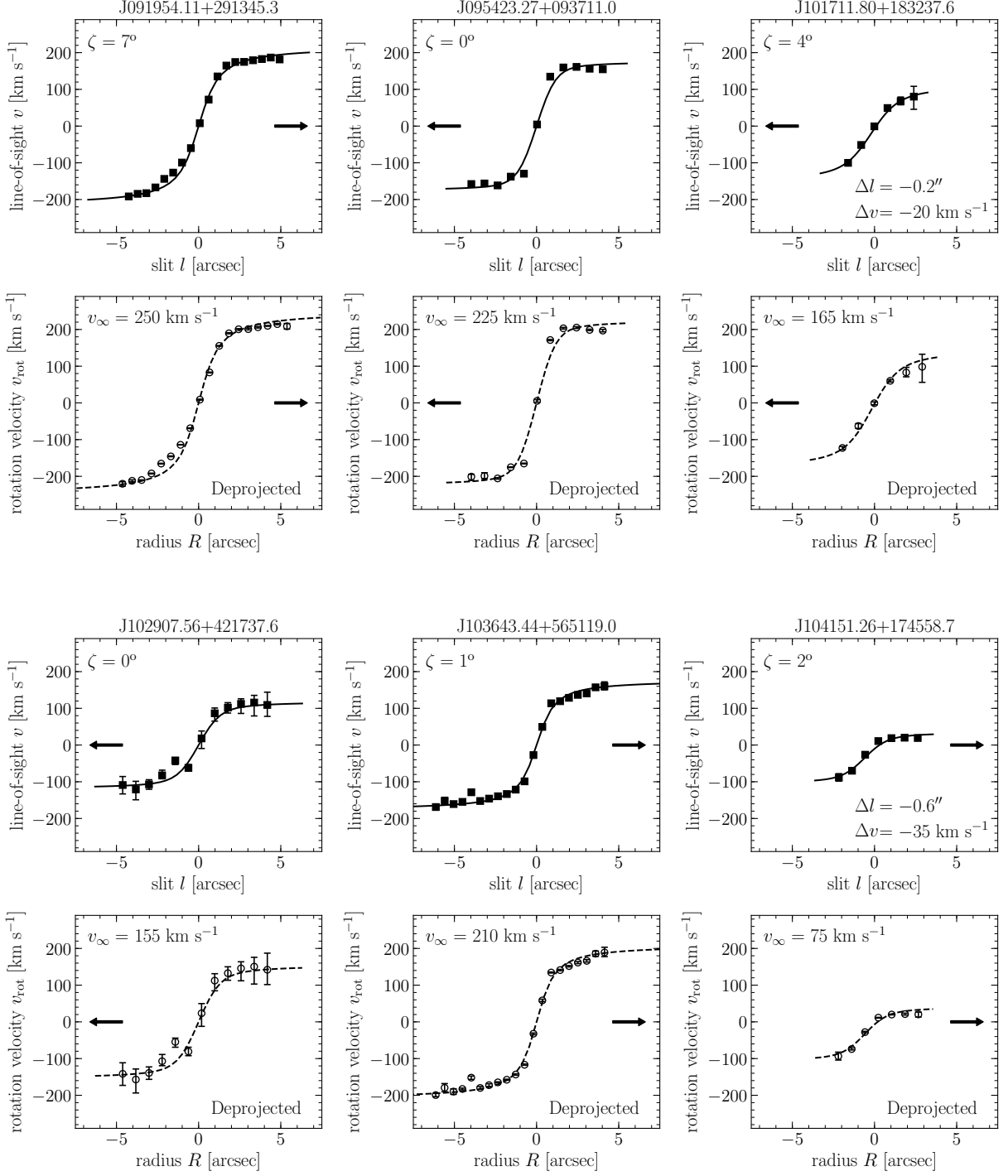


Figure B.2: Position-velocity maps and rotation curves for individual galaxies. (*Continued*)

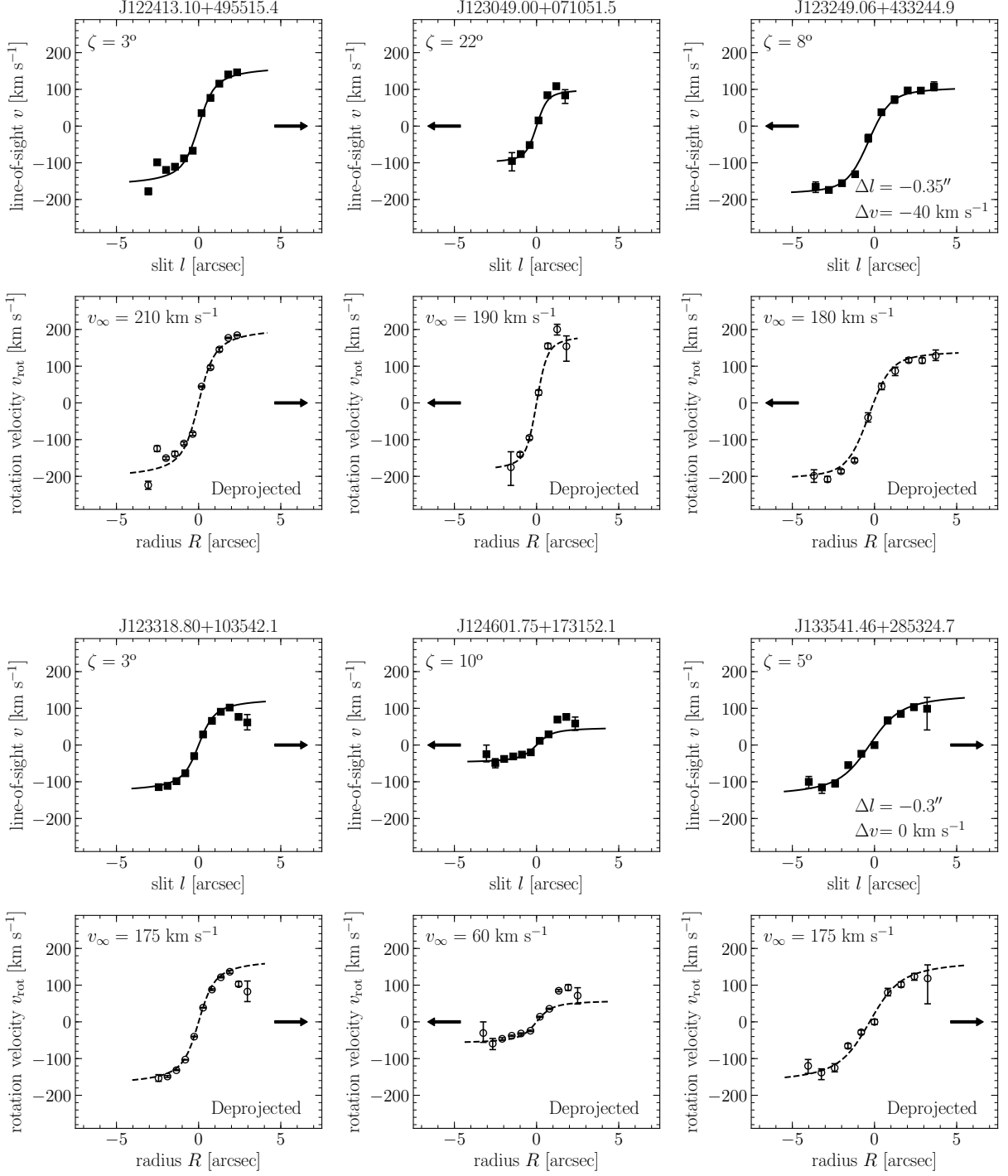


Figure B.3: Position–velocity maps and rotation curves for individual galaxies. (*Continued*)

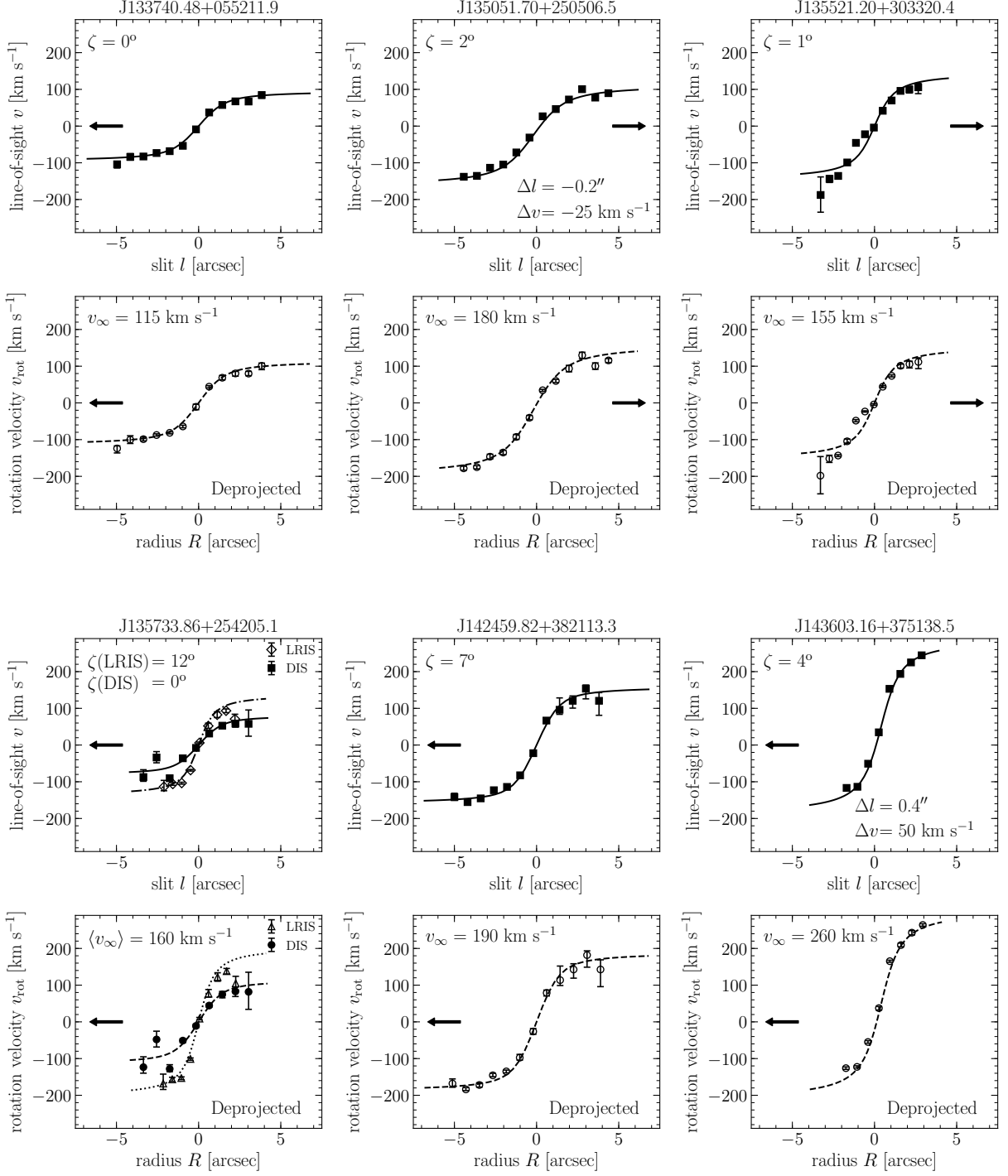


Figure B.4: Position-velocity maps and rotation curves for individual galaxies. (*Continued*)



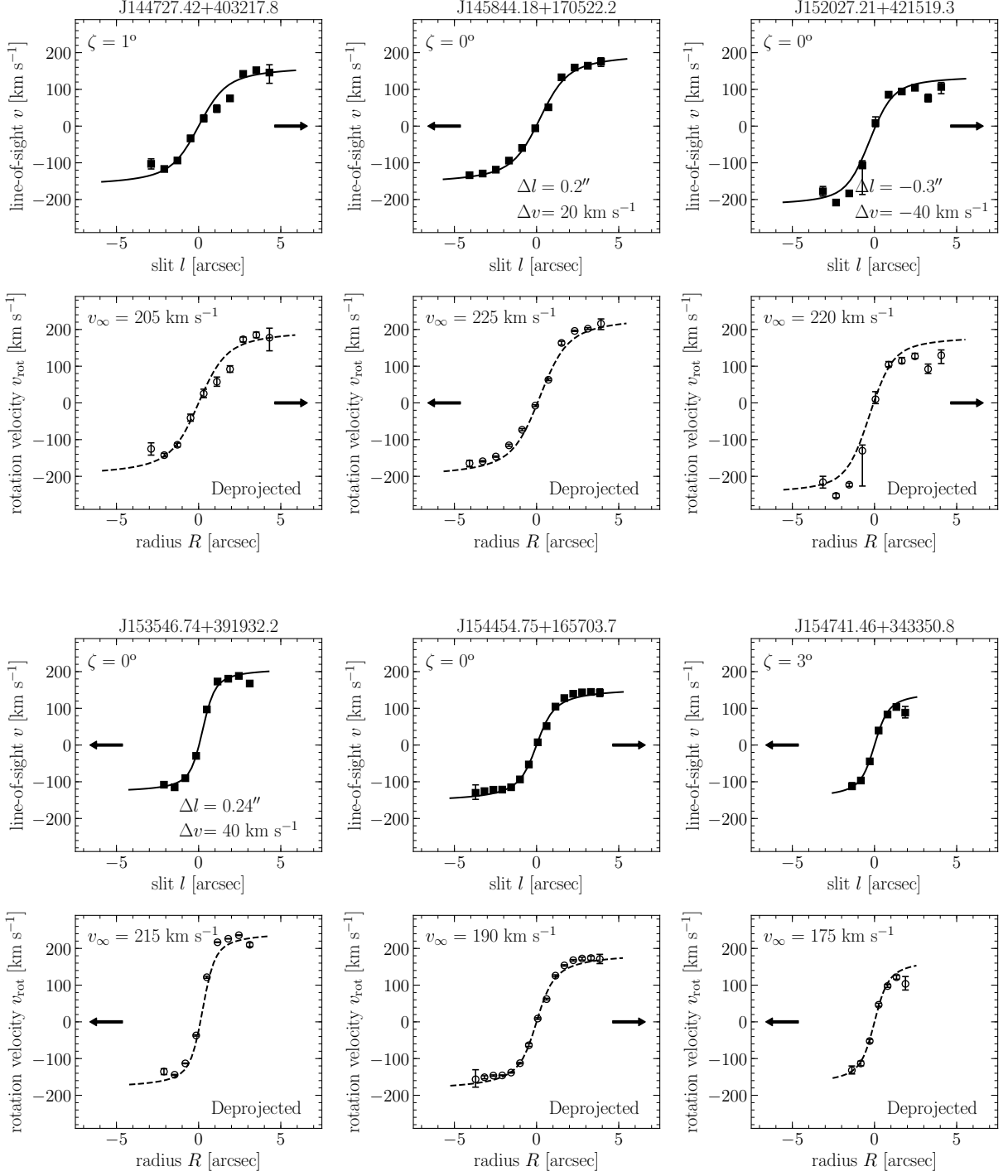


Figure B.5: Position-velocity maps and rotation curves for individual galaxies. (*Continued*)

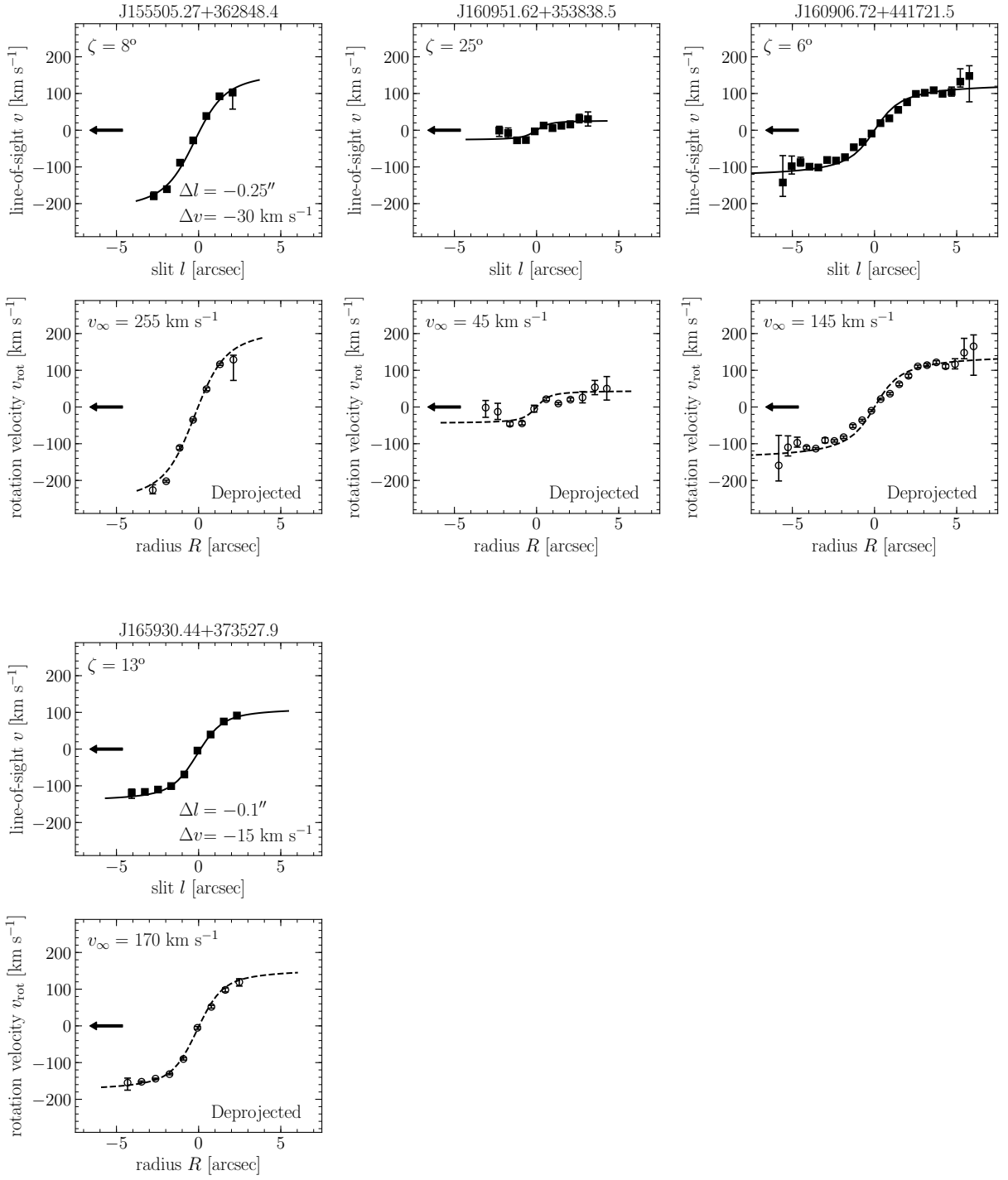


Figure B.6: Position-velocity maps and rotation curves for individual galaxies. (*Continued*)

# Appendix C

## Projected LOS Velocities of Cold Gas Particles in the EAGLE Simulations

The top row of Figure 4.3 shows the projected line-of-sight velocities of the cold gas particles ( $T_{\text{gas}} \leq 2.5 \times 10^5$  K) of one **EAGLE** galaxy (ID: 37448). In this Appendix, Figure C.1 shows the cold gas distribution of the remaining 10 central galaxies. Each particle is color-coded by its projected velocity, and we use the same velocity scale as in the top row of Figure 4.3. Most galaxies have an approaching (blueshifted) side and a receding (redshifted) side, indicating that the cold gas structures show signs of rotation.

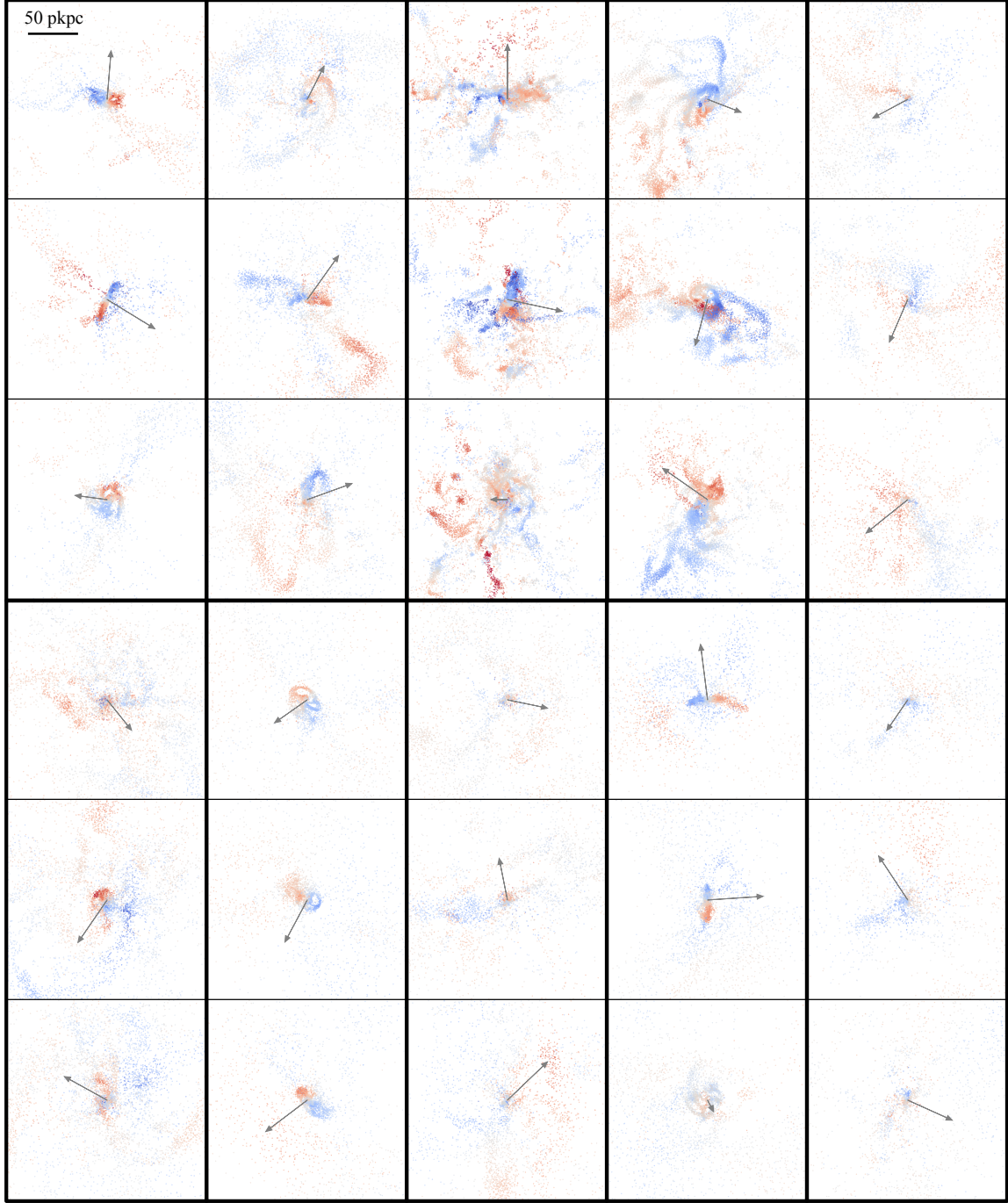


Figure C.1: Particle projection plots showing the projected line-of-sight velocities of cold gas particles ( $T_{\text{gas}} \leq 2.5 \times 10^5$  K). Each particle is color-coded by its projected velocity, and we use the same velocity scale as in the top row of Figure 4.3. This figure follows the same format as in Figure 4.4. Each galaxy occupies 3 rows  $\times$  1 column, enclosed by the thick black lines. For individual galaxies, from top to bottom, each panel represents the cut in the  $x$ ,  $y$ , and  $z$  planes, respectively. The side length of each panel is 200 pkpc. The plotted central galaxies are ordered in decreasing stellar masses, from left to right, and top to bottom.

# Bibliography

- Ahn, C. P., Alexandroff, R., Allende Prieto, C., et al. 2012, *ApJS*, 203, 21
- Anglés-Alcázar, D., Faucher-Giguère, C.-A., Kereš, D., et al. 2017, *MNRAS*, 470, 4698
- Bahé, Y. M., Crain, R. A., Kauffmann, G., et al. 2016, *MNRAS*, 456, 1115
- Barcons, X., Lanzettat, K. M., & Webb, J. K. 1995, *Nature*, 376, 321
- Barker, M. K., Ferguson, A. M. N., Cole, A. A., et al. 2011, *MNRAS*, 410, 504
- Behroozi, P. S., Conroy, C., & Wechsler, R. H. 2010, *ApJ*, 717, 379
- Bell, E. F., & de Jong, R. S. 2000, *MNRAS*, 312, 497
- Benjamin, R. A. 2002, in *Astronomical Society of the Pacific Conference Series*, Vol. 276, *Seeing Through the Dust: The Detection of HI and the Exploration of the ISM in Galaxies*, ed. A. R. Taylor, T. L. Landecker, & A. G. Willis, 201
- Benjamin, R. A. 2012, in *EAS Publications Series*, Vol. 56, *EAS Publications Series*, ed. M. A. de Avillez, 299–304
- Bigiel, F., Leroy, A., Walter, F., et al. 2008, *AJ*, 136, 2846
- Bigiel, F., Leroy, A. K., Walter, F., et al. 2011, *ApJL*, 730, L13
- Blanton, M. R., Hogg, D. W., Bahcall, N. A., et al. 2003, *ApJ*, 592, 819
- Boksenberg, A., & Sargent, W. L. W. 2015, *ApJS*, 218, 7
- Bordoloi, R., Lilly, S. J., Kacprzak, G. G., & Churchill, C. W. 2014, *ApJ*, 784, 108
- Bordoloi, R., Lilly, S. J., Knobel, C., et al. 2011, *ApJ*, 743, 10
- Boselli, A., Gavazzi, G., Donas, J., & Scodeggio, M. 2001, *AJ*, 121, 753
- Bouché, N., Hohensee, W., Vargas, R., et al. 2012, *MNRAS*, 426, 801

- Bouché, N., Murphy, M. T., Kacprzak, G. G., et al. 2013, *Science*, 341, 50
- Bouché, N., Murphy, M. T., Péroux, C., Csabai, I., & Wild, V. 2006, *MNRAS*, 371, 495
- Bouché, N., Dekel, A., Genzel, R., et al. 2010, *ApJ*, 718, 1001
- Bouché, N., Finley, H., Schroetter, I., et al. 2016, *ApJ*, 820, 121
- Bowen, D. V., Chelouche, D., Jenkins, E. B., et al. 2016, *ApJ*, 826, 50
- Bregman, J. N., Anderson, M. E., Miller, M. J., et al. 2018, *ApJ*, 862, 3
- Bresolin, F. 2011, *ApJ*, 730, 129
- Bresolin, F., Kudritzki, R.-P., Urbaneja, M. A., et al. 2016, *ApJ*, 830, 64
- Bresolin, F., Ryan-Weber, E., Kennicutt, R. C., & Goddard, Q. 2009, *ApJ*, 695, 580
- Brinchmann, J., Charlot, S., White, S. D. M., et al. 2004, *MNRAS*, 351, 1151
- Brook, C. B., Stinson, G., Gibson, B. K., Wadsley, J., & Quinn, T. 2012, *MNRAS*, 424, 1275
- Brook, C. B., Governato, F., Roškar, R., et al. 2011, *MNRAS*, 415, 1051
- Bruzual, G., & Charlot, S. 2003, *MNRAS*, 344, 1000
- Bryan, G. L., & Norman, M. L. 1998, *ApJ*, 495, 80
- Calzetti, D., Armus, L., Bohlin, R. C., et al. 2000, *ApJ*, 533, 682
- Carlberg, R. G., & Freedman, W. L. 1985, *ApJ*, 298, 486
- Chabrier, G. 2003, *PASP*, 115, 763
- Charlton, J. C., & Churchill, C. W. 1998, *ApJ*, 499, 181
- Chen, H.-W., Helsby, J. E., Gauthier, J.-R., et al. 2010, *ApJ*, 714, 1521
- Chen, H.-W., Kennicutt, Jr., R. C., & Rauch, M. 2005, *ApJ*, 620, 703
- Chen, H.-W., & Mulchaey, J. S. 2009, *ApJ*, 701, 1219
- Christensen, C. R., Davé, R., Governato, F., et al. 2016, *ApJ*, 824, 57
- Churchill, C. W., Trujillo-Gomez, S., Nielsen, N. M., & Kacprzak, G. G. 2013, *ApJ*, 779, 87
- Coil, A. L., Blanton, M. R., Burles, S. M., et al. 2011, *ApJ*, 741, 8

- Conroy, C., & Wechsler, R. H. 2009, *ApJ*, 696, 620
- Cool, R. J., Moustakas, J., Blanton, M. R., et al. 2013, *ApJ*, 767, 118
- Correa, C. A., Schaye, J., van de Voort, F., Duffy, A. R., & Wyithe, J. S. B. 2018a, *MNRAS*, 478, 255
- Correa, C. A., Schaye, J., Wyithe, J. S. B., et al. 2018b, *MNRAS*, 473, 538
- Crain, R. A., Schaye, J., Bower, R. G., et al. 2015, *MNRAS*, 450, 1937
- Crain, R. A., Bahé, Y. M., Lagos, C. d. P., et al. 2017, *MNRAS*, 464, 4204
- Dalla Vecchia, C., & Schaye, J. 2008, *MNRAS*, 387, 1431
- . 2012, *MNRAS*, 426, 140
- Danovich, M., Dekel, A., Hahn, O., Ceverino, D., & Primack, J. 2015, *MNRAS*, 449, 2087
- Danovich, M., Dekel, A., Hahn, O., & Teyssier, R. 2012, *MNRAS*, 422, 1732
- Davé, R., Finlator, K., & Oppenheimer, B. D. 2012, *MNRAS*, 421, 98
- Davis, M., Efstathiou, G., Frenk, C. S., & White, S. D. M. 1985, *ApJ*, 292, 371
- de Grijs, R. 1998, *MNRAS*, 299, 595
- de Jong, R. S. 1996, *A&A*, 313, 377
- Dekel, A., & Birnboim, Y. 2006, *MNRAS*, 368, 2
- Diamond-Stanic, A. M., Coil, A. L., Moustakas, J., et al. 2016, *ApJ*, 824, 24
- Diemer, B., & Kravtsov, A. V. 2015, *ApJ*, 799, 108
- Dolag, K., Borgani, S., Murante, G., & Springel, V. 2009, *MNRAS*, 399, 497
- Edlén, B. 1966, *Metrologia*, 2, 71
- Eisenstein, D. J., Weinberg, D. H., Agol, E., et al. 2011, *AJ*, 142, 72
- El-Badry, K., Quataert, E., Wetzel, A., et al. 2018, *MNRAS*, 473, 1930
- Erb, D. K., Quider, A. M., Henry, A. L., & Martin, C. L. 2012, *ApJ*, 759, 26
- Fall, S. M., & Efstathiou, G. 1980, *MNRAS*, 193, 189
- Faucher-Giguère, C.-A., & Kereš, D. 2011, *MNRAS*, 412, L118

- Fitzpatrick, E. L. 1999, *PASP*, 111, 63
- Flynn, C., Holmberg, J., Portinari, L., Fuchs, B., & Jahreiß, H. 2006, *MNRAS*, 372, 1149
- Ford, A. B., Davé, R., Oppenheimer, B. D., et al. 2014, *MNRAS*, 444, 1260
- Ford, A. B., Werk, J. K., Davé, R., et al. 2016, *MNRAS*, 459, 1745
- Fox, A. J., Wakker, B. P., Barger, K. A., et al. 2014, *ApJ*, 787, 147
- Fraternali, F., van Moorsel, G., Sancisi, R., & Oosterloo, T. 2002, *AJ*, 123, 3124
- Fruchter, A. S., Hack, W., Dencheva, N., Droettboom, M., & Greenfield, P. 2010, in 2010 Space Telescope Science Institute Calibration Workshop, p. 382-387, 382–387
- Furlong, M., Bower, R. G., Theuns, T., et al. 2015, *MNRAS*, 450, 4486
- Gauthier, J.-R., & Chen, H.-W. 2012, *MNRAS*, 424, 1952
- Gauthier, J.-R., Chen, H.-W., & Tinker, J. L. 2009, *ApJ*, 702, 50
- Gehrels, N. 1986, *ApJ*, 303, 336
- Gentile, G., Józsa, G. I. G., Serra, P., et al. 2013, *A&A*, 554, A125
- Ghez, A. M., Salim, S., Weinberg, N. N., et al. 2008, *ApJ*, 689, 1044
- Goddard, Q. E., Bresolin, F., Kennicutt, R. C., Ryan-Weber, E. V., & Rosales-Ortega, F. F. 2011, *MNRAS*, 412, 1246
- Gogarten, S. M., Dalcanton, J. J., Williams, B. F., et al. 2010, *ApJ*, 712, 858
- Gonzaga, S., & et al. 2012, *The DrizzlePac Handbook*
- Hafen, Z., Faucher-Giguere, C.-A., Angles-Alcazar, D., et al. 2018, *arXiv e-prints*, arXiv:1811.11753
- Hanuschik, R. W. 2003, *A&A*, 407, 1157
- Heald, G., Józsa, G., Serra, P., et al. 2011, *A&A*, 526, A118
- Heckman, T., Borthakur, S., Wild, V., Schiminovich, D., & Bordoloi, R. 2017, *ApJ*, 846, 151
- Heckman, T. M., Alexandroff, R. M., Borthakur, S., Overzier, R., & Leitherer, C. 2015, *ApJ*, 809, 147
- Heckman, T. M., Lehnert, M. D., Strickland, D. K., & Armus, L. 2000, *ApJS*, 129, 493
- Ho, S. H., & Martin, C. L. 2019, *arXiv e-prints*, arXiv:1901.11182



- Ho, S. H., Martin, C. L., Kacprzak, G. G., & Churchill, C. W. 2017, *ApJ*, 835, 267
- Ho, S. H., Martin, C. L., & Turner, M. L. 2019, *ApJ*, 875, 54
- Hubble, E. P. 1926, *ApJ*, 64, 321
- Johnson, S. D., Chen, H.-W., & Mulchaey, J. S. 2013, *MNRAS*, 434, 1765
- . 2015, *MNRAS*, 449, 3263
- Kacprzak, G. G., Churchill, C. W., Barton, E. J., & Cooke, J. 2011, *ApJ*, 733, 105
- Kacprzak, G. G., Churchill, C. W., Ceverino, D., et al. 2010, *ApJ*, 711, 533
- Kacprzak, G. G., Churchill, C. W., & Nielsen, N. M. 2012, *ApJL*, 760, L7
- Kacprzak, G. G., Muzahid, S., Churchill, C. W., Nielsen, N. M., & Charlton, J. C. 2015, *ApJ*, 815, 22
- Kacprzak, G. G., Martin, C. L., Bouché, N., et al. 2014, *ApJL*, 792, L12
- Kacprzak, G. G., Vander Vliet, J. R., Nielsen, N. M., et al. 2019, *ApJ*, 870, 137
- Kamphuis, P., Rand, R. J., Józsa, G. I. G., et al. 2013, *MNRAS*, 434, 2069
- Keeney, B. A., Stocke, J. T., Rosenberg, J. L., et al. 2013, *ApJ*, 765, 27
- Kennicutt, Jr., R. C. 1983, *ApJ*, 272, 54
- . 1998, *ARA&R*, 36, 189
- Kennicutt, Jr., R. C., Tamblyn, P., & Congdon, C. E. 1994, *ApJ*, 435, 22
- Kereš, D., Katz, N., Fardal, M., Davé, R., & Weinberg, D. H. 2009, *MNRAS*, 395, 160
- Kereš, D., Katz, N., Weinberg, D. H., & Davé, R. 2005, *MNRAS*, 363, 2
- Kimm, T., Devriendt, J., Slyz, A., et al. 2011, *ArXiv e-prints*, arXiv:1106.0538
- Kravtsov, A., Vikhlinin, A., & Meshcheryakov, A. 2014, *ArXiv e-prints*, arXiv:1401.7329
- Kregel, M., van der Kruit, P. C., & de Grijs, R. 2002, *MNRAS*, 334, 646
- Kriek, M., van Dokkum, P. G., Labbé, I., et al. 2009, *ApJ*, 700, 221
- Krist, J. E., Hook, R. N., & Stoehr, F. 2011, in *Proc. SPIE*, Vol. 8127, Optical Modeling and Performance Predictions V, 81270J
- Lagos, C. d. P., Schaye, J., Bahé, Y., et al. 2018, *MNRAS*, 476, 4327

- Lagos, C. d. P., Theuns, T., Stevens, A. R. H., et al. 2017, MNRAS, 464, 3850
- Lagos, C. d. P., Crain, R. A., Schaye, J., et al. 2015, MNRAS, 452, 3815
- Lan, T.-W., Ménard, B., & Zhu, G. 2014, ApJ, 795, 31
- Lanzetta, K. M., & Bowen, D. V. 1992, ApJ, 391, 48
- Lehner, N., Howk, J. C., Tripp, T. M., et al. 2013, ApJ, 770, 138
- Leroy, A. K., Walter, F., Brinks, E., et al. 2008, AJ, 136, 2782
- Leroy, A. K., Walter, F., Sandstrom, K., et al. 2013, AJ, 146, 19
- MacArthur, L. A., Courteau, S., Bell, E., & Holtzman, J. A. 2004, ApJS, 152, 175
- Marasco, A., & Fraternali, F. 2011, A&A, 525, A134
- Martin, C. L. 1999, ApJ, 513, 156
- Martin, C. L., Ho, S. H., Kacprzak, G. G., & Churchill, C. W. 2019, ApJ, 878, 84
- Martin, C. L., Kobulnicky, H. A., & Heckman, T. M. 2002, ApJ, 574, 663
- Martin, C. L., Shapley, A. E., Coil, A. L., et al. 2012, ApJ, 760, 127
- Martin, D. C., Fanson, J., Schiminovich, D., et al. 2005, ApJL, 619, L1
- McAlpine, S., Helly, J. C., Schaller, M., et al. 2016, Astronomy and Computing, 15, 72
- McDonald, P., & Miralda-Escudé, J. 1999, ApJ, 519, 486
- McGaugh, S. S., Schombert, J. M., de Blok, W. J. G., & Zagursky, M. J. 2010, ApJL, 708, L14
- McMillan, P. J. 2011, MNRAS, 414, 2446
- Mo, H. J., Mao, S., & White, S. D. M. 1998, MNRAS, 295, 319
- Morrissey, P., Conrow, T., Barlow, T. A., et al. 2007, ApJS, 173, 682
- Morton, D. C. 2003, ApJS, 149, 205
- Moustakas, J., Coil, A. L., Aird, J., et al. 2013, ApJ, 767, 50
- Muñoz-Mateos, J. C., Boissier, S., Gil de Paz, A., et al. 2011, ApJ, 731, 10
- Muratov, A. L., Kereš, D., Faucher-Giguère, C.-A., et al. 2015, MNRAS, 454, 2691
- Murray, N., Martin, C. L., Quataert, E., & Thompson, T. A. 2007, ApJ, 660, 211

- Navarro, J. F., Frenk, C. S., & White, S. D. M. 1996, *ApJ*, 462, 563
- Nelson, D., Genel, S., Vogelsberger, M., et al. 2015, *MNRAS*, 448, 59
- Nelson, D., Vogelsberger, M., Genel, S., et al. 2013, *MNRAS*, 429, 3353
- Nelson, D., Kauffmann, G., Pillepich, A., et al. 2018, *MNRAS*, 477, 450
- Nestor, D. B., Turnshek, D. A., & Rao, S. M. 2005, *ApJ*, 628, 637
- Nielsen, N. M., Churchill, C. W., & Kacprzak, G. G. 2013, *ApJ*, 776, 115
- Nielsen, N. M., Churchill, C. W., Kacprzak, G. G., Murphy, M. T., & Evans, J. L. 2015, *ApJ*, 812, 83
- Nielsen, N. M., Kacprzak, G. G., Pointon, S. K., Churchill, C. W., & Murphy, M. T. 2018, *ArXiv e-prints*, arXiv:1808.09562
- Oke, J. B., Cohen, J. G., Carr, M., et al. 1995, *PASP*, 107, 375
- Oosterloo, T., Fraternali, F., & Sancisi, R. 2007, *AJ*, 134, 1019
- Oppenheimer, B. D. 2018, *MNRAS*, 480, 2963
- Oppenheimer, B. D., Davé, R., Kereš, D., et al. 2010, *MNRAS*, 406, 2325
- Oppenheimer, B. D., & Schaye, J. 2013, *MNRAS*, 434, 1043
- Papovich, C., Labbé, I., Quadri, R., et al. 2015, *ApJ*, 803, 26
- Patterson, M. T., Walterbos, R. A. M., Kennicutt, R. C., Chiappini, C., & Thilker, D. A. 2012, *MNRAS*, 422, 401
- Peeples, M. S., Werk, J. K., Tumlinson, J., et al. 2014, *ApJ*, 786, 54
- Peng, C. Y., Ho, L. C., Impey, C. D., & Rix, H.-W. 2002, *AJ*, 124, 266
- Peng, Y.-j., Lilly, S. J., Kovač, K., et al. 2010, *ApJ*, 721, 193
- Phillips, A. C., Miller, J., Cowley, D., & Wallace, V. 2006, in *Society of Photo-Optical Instrumentation Engineers (SPIE) Conference Series*, Vol. 6269, *Society of Photo-Optical Instrumentation Engineers (SPIE) Conference Series*, 1
- Pichon, C., Pogosyan, D., Kimm, T., et al. 2011, *MNRAS*, 418, 2493
- Planck Collaboration, Ade, P. A. R., Aghanim, N., et al. 2015, *ArXiv e-prints*, arXiv:1502.01589
- Press, W. H., Teukolsky, S. A., Vetterling, W. T., & Flannery, B. P. 1992, *Numerical recipes in FORTRAN. The art of scientific computing*

- Prochaska, J. X., & Wolfe, A. M. 1997, *ApJ*, 487, 73
- Prochaska, J. X., Werk, J. K., Worseck, G., et al. 2017, *ApJ*, 837, 169
- Prochter, G. E., Prochaska, J. X., & Burles, S. M. 2006, *ApJ*, 639, 766
- Putman, M. E., Peek, J. E. G., & Jounge, M. R. 2012, *ARA&R*, 50, 491
- Quiet, S., Péroux, C., Zafar, T., et al. 2016, *MNRAS*, 458, 4074
- Rahman, N., Bolatto, A. D., Xue, R., et al. 2012, *ApJ*, 745, 183
- Roberts, M. S. 1963, *ARA&R*, 1, 149
- Robertson, B. E., & Kravtsov, A. V. 2008, *ApJ*, 680, 1083
- Rockosi, C., Stover, R., Kibrick, R., et al. 2010, in *Society of Photo-Optical Instrumentation Engineers (SPIE) Conference Series*, Vol. 7735, *Society of Photo-Optical Instrumentation Engineers (SPIE) Conference Series*, 0
- Rosolowsky, E., & Simon, J. D. 2008, *ApJ*, 675, 1213
- Roškar, R., Debattista, V. P., Brooks, A. M., et al. 2010, *MNRAS*, 408, 783
- Rubin, K. H. R., Prochaska, J. X., Koo, D. C., & Phillips, A. C. 2012, *ApJL*, 747, L26
- Rubin, K. H. R., Prochaska, J. X., Koo, D. C., et al. 2014, *ApJ*, 794, 156
- Rudie, G. C., Steidel, C. C., Trainor, R. F., et al. 2012, *ApJ*, 750, 67
- Rupke, D. S., Veilleux, S., & Sanders, D. B. 2005, *ApJS*, 160, 115
- Saintonge, A., Kauffmann, G., Kramer, C., et al. 2011, *MNRAS*, 415, 32
- Sancisi, R., & Allen, R. J. 1979, *A&A*, 74, 73
- Schawinski, K., Urry, C. M., Simmons, B. D., et al. 2014, *MNRAS*, 440, 889
- Schaye, J., & Dalla Vecchia, C. 2008, *MNRAS*, 383, 1210
- Schaye, J., Dalla Vecchia, C., Booth, C. M., et al. 2010, *MNRAS*, 402, 1536
- Schaye, J., Crain, R. A., Bower, R. G., et al. 2015, *MNRAS*, 446, 521
- Schiminovich, D., Catinella, B., Kauffmann, G., et al. 2010, *MNRAS*, 408, 919
- Schlafly, E. F., & Finkbeiner, D. P. 2011, *ApJ*, 737, 103
- Schmidt, M. 1963, *ApJ*, 137, 758

- Shen, S., Madau, P., Aguirre, A., et al. 2012, *ApJ*, 760, 50
- Shull, J. M. 2014, *ApJ*, 784, 142
- Sommer-Larsen, J. 1991, *MNRAS*, 249, 368
- Springel, V. 2005, *MNRAS*, 364, 1105
- Springel, V., White, S. D. M., Tormen, G., & Kauffmann, G. 2001, *MNRAS*, 328, 726
- Steidel, C. C., Dickinson, M., & Persson, S. E. 1994, *ApJL*, 437, L75
- Steidel, C. C., Kollmeier, J. A., Shapley, A. E., et al. 2002, *ApJ*, 570, 526
- Steidel, C. C., Rudie, G. C., Strom, A. L., et al. 2014, *ApJ*, 795, 165
- Stern, J., Faucher-Giguère, C.-A., Hennawi, J. F., et al. 2018, *ApJ*, 865, 91
- Stevens, A. R. H., Lagos, C. d. P., Contreras, S., et al. 2017, *MNRAS*, 467, 2066
- Stewart, K. R., Brooks, A. M., Bullock, J. S., et al. 2013, *ApJ*, 769, 74
- Stewart, K. R., Kaufmann, T., Bullock, J. S., et al. 2011, *ApJ*, 738, 39
- Stewart, K. R., Maller, A. H., Oñorbe, J., et al. 2017, *ApJ*, 843, 47
- Stocke, J. T., Keeney, B. A., Danforth, C. W., et al. 2013, *ApJ*, 763, 148
- Strateva, I., Ivezić, Ž., Knapp, G. R., et al. 2001, *AJ*, 122, 1861
- Teklu, A. F., Remus, R.-S., Dolag, K., et al. 2015, *ApJ*, 812, 29
- Tinker, J. L., & Chen, H.-W. 2010, *ApJ*, 709, 1
- Trayford, J. W., Theuns, T., Bower, R. G., et al. 2016, *MNRAS*, 460, 3925
- . 2015, *MNRAS*, 452, 2879
- Tumlinson, J., Peebles, M. S., & Werk, J. K. 2017, *ARA&R*, 55, 389
- Tumlinson, J., Thom, C., Werk, J. K., et al. 2011, *Science*, 334, 948
- . 2013, *ApJ*, 777, 59
- Turk, M. J., Smith, B. D., Oishi, J. S., et al. 2011, *The Astrophysical Journal Supplement Series*, 192, 9
- Turner, M. L., Schaye, J., Crain, R. A., et al. 2017, *MNRAS*, 471, 690
- Turner, M. L., Schaye, J., Steidel, C. C., Rudie, G. C., & Strom, A. L. 2014, *MNRAS*, 445, 794

- van Dam, M. A., Bouchez, A. H., Le Mignant, D., et al. 2006, *PASP*, 118, 310
- van de Voort, F., & Schaye, J. 2012, *MNRAS*, 423, 2991
- van de Voort, F., Schaye, J., Booth, C. M., Haas, M. R., & Dalla Vecchia, C. 2011, *MNRAS*, 414, 2458
- van den Bergh, S. 1962, *AJ*, 67, 486
- van Dokkum, P. G. 2001, *PASP*, 113, 1420
- van Dokkum, P. G., Leja, J., Nelson, E. J., et al. 2013, *ApJL*, 771, L35
- Veilleux, S., Cecil, G., & Bland-Hawthorn, J. 2005, *ARA&R*, 43, 769
- Wakker, B. P., & van Woerden, H. 1997, *ARA&R*, 35, 217
- Wakker, B. P., Howk, J. C., Savage, B. D., et al. 1999, *Nature*, 402, 388
- Weiner, B. J., Coil, A. L., Prochaska, J. X., et al. 2009, *ApJ*, 692, 187
- Werk, J. K., Prochaska, J. X., Thom, C., et al. 2013, *ApJS*, 204, 17
- Werk, J. K., Prochaska, J. X., Tumlinson, J., et al. 2014, *ApJ*, 792, 8
- Werk, J. K., Prochaska, J. X., Cantalupo, S., et al. 2016, *ApJ*, 833, 54
- Wetzel, A. R., Deason, A. J., & Garrison-Kimmel, S. 2015, *ApJ*, 807, 49
- Wizinowich, P. L., Le Mignant, D., Bouchez, A. H., et al. 2006, *PASP*, 118, 297
- Woolf, V. M., & West, A. A. 2012, *MNRAS*, 422, 1489
- Worthey, G., Dorman, B., & Jones, L. A. 1996, *AJ*, 112, 948
- Yang, X., Mo, H. J., van den Bosch, F. C., Zhang, Y., & Han, J. 2012, *ApJ*, 752, 41
- York, D. G., Adelman, J., Anderson, Jr., J. E., et al. 2000, *AJ*, 120, 1579
- Zabl, J., Bouché, N. F., Schroetter, I., et al. 2019, *MNRAS*, 485, 1961
- Zheng, Y., Peek, J. E. G., Werk, J. K., & Putman, M. E. 2017, *ApJ*, 834, 179
- Zheng, Y., Putman, M. E., Peek, J. E. G., & Joung, M. R. 2015, *ApJ*, 807, 103
- Zschaechner, L. K., & Rand, R. J. 2015, *ApJ*, 808, 153
- Zschaechner, L. K., Rand, R. J., Heald, G. H., Gentile, G., & Józsa, G. 2012, *ApJ*, 760, 37
- Zschaechner, L. K., Rand, R. J., Heald, G. H., Gentile, G., & Kamphuis, P. 2011, *ApJ*, 740, 35